Real-time image-based feedback for microfluidic applications

Dean Frazer Crawford

Degree of Doctor of Philosophy

School of Engineering and Physical Sciences

Heriot Watt University

August 2019

Abstract

The field of microfluidics has been solving problems on the micro-scale for decades, but many in-flow analysis techniques only take single dimensional measurements. In this thesis, multi-dimensional, real-time image analysis has been used to improve and expand upon current microfluidic techniques in several microfluidic areas. Microdroplets within microfluidics are a promising technique for creating microscopic vessels for chemical and biochemical experiments, however accurately controlling such tiny objects can be difficult. The use of real-time image feedback has dramatically improved the monodispersity (coefficient of variation of 0.32%) and accurate loading of the contents of droplets. Beyond this, using these techniques, real-time analysis on the morphology of living cells can be carried out and used to isolate cells of interest. Machine learning algorithms have provided a rapid method to identify the cell populations based on quantitative parameters extracted from transmission or fluorescent images of the cells. By integrating fast piezo-based fluid manipulation, highly selective and accurate cell sorting can be performed within a lab-on-a-chip device for the isolation of subpopulations of cells based on their morphological features. Using this method, K562 cells have been sorted from a mixed population with an efficiency of 91.3% and a purity of 99.4%.

Acknowledgements

Over the past three years, I have been lucky enough to have the love and support of many people; family, friends and colleagues.

Firstly, I would like to thank my parents. Not only are you the reason I am here, but you are the reason I have got this far. You never pushed me, but encouraged me to reach my full potential and hopefully I've made you proud.

Stephanie, thanks for being such a great sister and friend. Our shared sense of humour has kept me smiling and I'm looking forward to finding out who will be a doctor first, depending on the graduation dates! Either way I'm so very proud of who you've become and everything you've achieved.

I am lucky enough to have such a big supportive family, who have been there for me over the years. I couldn't have asked for better grandparents, (George and Joan, Jock and Betty) you have given me great memories over the years and all the lessons you have taught me (from Pythagoras to playing draughts) will stay with me forever. To my aunties, uncles and cousins (Diane, Sandra, Liz, Billy, Jimmy, Steven, Christopher, Sean, Stephen and Tyler) you have provided me with lots of fun moments over the past three years, many of which provided a welcome break from the thesis writing. Your company during holidays to Orkney, Kenmore and Arbroath, and family parties helped kept me sane! Thanks also to David, Sharon and Ross, I've felt like part of the family since day one and I'm lucky to have such a warm second home.

Graeme, a huge thanks to you. You had so much patience and time for me over the last 5 years and I appreciate how lucky I was. Your door was always open and I thoroughly enjoyed all of our chats, both science and non-science related. It will be weird not seeing you every day, but we will definitely keep in touch! You are a great supervisor, mentor and friend.

A PhD isn't the easiest of jobs and I was lucky enough to have a great support network at Heriot Watt. Thanks to everyone that's been in my group over the years; Kai, Muhsincan, Ewa and Selene, your company was a joy! In addition, thank you to everyone in PoBBBS. From lunches, football and of course coffee breaks, I was so lucky to have such a great group of friends in one place, all the time.

Thanks to all my friends who have been there for me during the PhD. I've known some of you for as long as I can remember, some of you for only a few months and many more in between. My ECMS (Ami, Anna, Antz, Brian, Chapy, Emily, Lynne, Ross, Shannon, Stuart and Terri) thanks for always being there for me and for being a nice solid

base for the past what feels like a hundred years, you are my second family. Here's to many more years of fun and less of the retelling of my most embarrassing stories. Thanks to Jonny, Mark, Paul and Robyn for being part of my undergraduate journey. Here's to more often catch ups and less flying attempts. And to my new PGDE buddies, thanks for being part of my new journey. Here's to a long and successful teaching career and less time searching for my laptop (back your thesis up)!

And last but certainly not least, a huge thanks to my Gemma. You were my rock and I couldn't have done this PhD without you. Thanks for always being there for me and for keeping me smiling, even during the stressful times! I will make sure to return the favour when it's your turn! I met you at the start of this journey and you've been the best part of it. I am lucky to have you and I love you so very much.

Research Thesis Submission

Name*:*	Dean Frazer Crawford		
School:	EPS		
Version: *(i.e. First, Resubmission, Final)*	First	Degree Sought:	PhD

Declaration

In accordance with the appropriate regulations I hereby submit my thesis and I declare that:

1. The thesis embodies the results of my own work and has been composed by myself
2. Where appropriate, I have made acknowledgement of the work of others
3. Where the thesis contains published outputs under Regulation 6 (9.1.2) these are accompanied by a critical review which accurately describes my contribution to the research and, for multi-author outputs, a signed declaration indicating the contribution of each author (complete Inclusion of Published Works Form – see below)
4. The thesis is the correct version for submission and is the same version as any electronic versions submitted*.
5. My thesis for the award referred to, deposited in the Heriot-Watt University Library, should be made available for loan or photocopying and be available via the Institutional Repository, subject to such conditions as the Librarian may require
6. I understand that as a student of the University I am required to abide by the Regulations of the University and to conform to its discipline.
7. Inclusion of published outputs under Regulation 6 (9.1.2) shall not constitute plagiarism.
8. I confirm that the thesis has been verified against plagiarism via an approved plagiarism detection application e.g. Turnitin.

* *Please note that it is the responsibility of the candidate to ensure that the correct version of the thesis is submitted.*

Signature of Candidate*:*		Date:	

Submission

Submitted By *(name in capitals):*	
Signature of Individual Submitting:	
Date Submitted:	

For Completion in the Student Service Centre (SSC)

Received in the SSC by *(name in capitals):*	

Method of Submission *(Handed in to SSC; posted through internal/external mail):*			
E-thesis Submitted ***(mandatory for final theses)***			
Signature:		Date:	

Inclusion of Published Works

Declaration

This thesis contains one or more multi-author published works. In accordance with Regulation 6 (9.1.2) I hereby declare that the contributions of each author to these publications is as follows:

Citation details	Crawford, D. F., Smith, C. A. & Whyte, G. Image-based closed-loop feedback for highly mono-dispersed microdroplet production. Sci. Rep. 7, 10545 (2017).
Author 1	Carried out experiments and helped to write manuscript
Author 2	Helped designed experiments, write manuscript and provided device master
Author 3	Helped design experiments and write manuscript
Signature:	
Date:	

Contents

Introduction

Microfluidics, as the name suggests, involves the manipulation of microscopic volumes of fluid within micron channel walls. The dimensions of such channels can be manufactured to match that of small particles, providing a platform that is perfect for the analysis of cells. The micron sized channels allow for a fast sample throughput, providing the ability to perform a high number of measurements in a small amount of time[1]. These channels can also be manufactured to be similar to that of the cell diameter, providing a platform to accurately control and manoeuvre cells[2]. Although one thing that is lacking in many current microfluidic techniques is the ability to accurately observe and control the manipulation of the confined solutions and/or cells. Most analysis performed in flow measures one parameter at a time (this will be referred to as one-dimensional measurements), such as fluorescence[3], scatter[4] and electrical impedance[5]; but there is much more that can be learned from higher dimensional measurements. In this work higher dimensional measurements will be taken in flow and analysed to provide real-time feedback and control within the microfluidic devices to tackle current problems. **Chapter 1** in this thesis provides a background to the work described in the later results chapters, while **Chapter 2** describes the methods used to carry out the experiments.

The first problem to be addressed in this work involves the implementation of an image-based feedback system to accurately control the volume and frequency of microdroplets. Microdroplets act as discrete vesicles and allow samples, such as reactants, drugs or cells, to be encased in a second immiscible phase (they will be introduced and discussed in more detail in **Section 1.3**). To ensure samples are of the correct volume or concentration, it is important to have accurate control over microdroplet volume. **Chapter 3** discusses a technique which uses real-time imaging to collect two dimensional data (droplet length as a function of time). This along with image-based feedback is used to accurately control, not only the droplet volume, but also the droplet generation frequency or droplet cell concentration simultaneously. To measure the number of cells in each droplet, two dimensional images and time resolution information is required.

The image analysis techniques used in **Chapter 3** are taken and expanded upon in **Chapter 4** and **Chapter 5** to perform image-based cell sorting. All living things are made up of cells; from amoebas to algae, from bananas to baboons, from cacti to cows and of course us, humans. These microscopic structures are the smallest unit of life that

can function as a complete organism, but the real marvel occurs when trillions of cells form single, complex, organisms such as ourselves. Various cell types, each with their own structure and functions, work together to perform a number of processes to keep us alive. There are around 200 different cell types within the human body and each one performs specific functions; osteocyte bone cells provide the body with structure, hepatocyte liver cells are involved in metabolising carbohydrates and detoxification, and neuronal brain cells transfer electrical signals to communicate with each other. Even though these cells look and function differently they all contain the same set of instructions, encoded within their DNA. Human DNA is split into roughly 20,000 sub units called genes[6]. These genes code for specific proteins, which have an important role in cell function. However, only a fraction of the genes within a cell are turned on and it is these differences that provide heterogeneity between cells. These can be significant, for example the difference between a red blood cell and a white blood cell; or more subtle, like two different sub-types of white blood cells (neutrophils and monocytes). Understanding the heterogeneity and the differences in gene expression is of great interest to cell biologists and can provide a new insight into challenging medical areas such as cancer development, genetic diseases and tissue regeneration. To characterise these differences, cells of interest must be isolated from and compared to other cells within the population. It is then possible to understand which genes are important in specific medical conditions, potentially leading to better diagnostic and therapeutic tools. Microfluidic devices are ideal for this cell sorting task.

Traditionally some cell sorting techniques have involved large pieces of equipment, with high running costs that move the cells within potentially damaging and hazardous aerosols, such as fluorescence activated cell sorting (discussed in **Section 1.6**). Microfluidic devices can address these problems, as they are small and easy to produce and can move the cells within a cell appropriate solution or encased within a microdroplet. There are a number of microfluidic techniques which have been used to sort cells. Passive methods are able to sort based on cell size, but require specific designs and running conditions which can be difficult to adjust for new samples. **Chapter 4** uses an imaging and real time decision making technique to actively sort large K562 cells from red blood cells (RBCs) in flow.

More complex cell sorting methods commonly use fluorescent labels to target specific structures within the cells, allowing them to be characterised based on one dimensional, total fluorescent intensity measurements. This has allowed a wide range of different cell subpopulations to be isolated and investigated, but there is however, a

limitation to this technology. For example if two cells contain the same concentration of the fluorescent label, but it is distributed differently in each cell, they will be undistinguishable. The main goal of **Chapter 5** is to tackle this problem. By employing in-flow, real-time, image-based analysis, cells can be imaged and characterised based on their sub-cellular morphologies. This extends the real-time feedback to allow the use of three dimensional data (2D morphological information over time), which opens up a wide range of new potential cell types which can be sorted and cell functions that can be understood.

This work is split into five main chapters; a background chapter (**Chapter 1)**, which introduces both microdroplet production and cell sorting, providing an overview of key knowledge areas needed for the remaining chapters; a methods chapter (**Chapter 2**), which describes the methods used to carry out the experiments in this work; and three results chapters. The first results chapter **(Chapter 3)**, describes the use of image-based feedback to accurately control the volume, frequency and cell concentration of microdroplet production. A new device and setup was then designed for the imaging and sorting of a model cell solution (RBCs and K562s) and this work is discussed in **Chapter 4**. Cells were imaged in flow and their external morphology was analysed in real time. This information was used to determine if a cell should be sorted into a specific outlet. The final chapter (**Chapter 5)** extends this technique to include fluorescent-based imaging and machine-learning-based classification, allowing cell types with different sub-cellular structures to be imaged identified and sorted.

Image-based sorting is the next frontier in cell sorting with many image-based techniques described in publications within the last couple of years. This work provides an easy to use, microfluidic chip based solution to both classify and sort different cells based on their nuclear morphology, allowing new and potentially exciting cell functions to be investigated.

Chapter 1. Background

This section will provide a background on the topics discussed in the later chapters within this thesis. A brief overview of microfluidics and the microscopy needed to image within the devices is given, followed by two larger sections. The first discusses microdroplet generation and the ability to measure and control parameters of the droplet generation; this is paramount for **Chapter 3**, in which the volume and frequency of microdroplet production is controlled with record monodispersity. The second section discusses microfluidic based cell sorting which will be important for **Chapters 4 and 5**, which discuss image-based cell sorting both in bright field and fluorescent modes.

1.1 Microfluidics

Microfluidics is a relatively new field, with the first microfluidic device created in 1979 at Stanford University, a portable gas detector[7]. Since then the field has rapidly expanded, especially in the past two decades[8] and the estimated worth of the microfluidic industry is in the order of billions of dollars[9]. Experiments are mainly performed in microscopic channels with dimensions from tens to hundreds of micrometres and the ability to accurately control solutions on such a small scale has a number of advantages. Small bodies such as individual cells can be moved and manipulated; with the size of the microfluidic channels similar to that of the cell diameter[10]. This can be done both in flow within a cell friendly solution or within microdroplets.

From microfluidics, a number of new 'subfields' have branched out. These include organ-on-a-chip[11], microfluidics for point-of-care (POC) diagnostics[12], paper-based microfluidics[13], single cell microfluidics[14] and droplet microfluidics[15] (the latter two will be discussed further on in this chapter). The first of these fields, organ-on-a-chip, allows for the replication of three-dimensional tissue. Initial experiments demonstrated the synthesis of a single tissue type using one type of cell, this allowed the functions of the tissue to be replicated and observed within the microfluidic device[16]. Recent advancements in 3D bioprinting technology has resulted in the increased precision of the positioning of individual cells into a 3D tissue[17], allowing for more complex heterogeneous structures to be generated[18]. Recent studies have focussed on using this technology to recreate blood vessels[19], hearts[20], kidneys[21], livers[22] and lungs[23]. Drugs and/or toxins can then be added into the artificial tissue, to simulate how they would react with real life samples[24,25]. This is seen as one of the 'greatest values' of organ-on-a-chip

devices; the ability to test and prioritise drug candidates may provide an intermediate stage between single cell testing and animal testing[16]. Some predictions suggest that this technology will allow for the reduction and maybe even the replacement (in some cases) of animal testing[11].

Another medical application for microfluidic devices is point-of-care diagnosis. The inability to diagnose diseases in a quick and efficient manner in the developing world, results in a disproportionate amount of deaths when compared to the developed world[26]. POC microfluidic-based tests provide a rapid and affordable solution to this problem. Recent designs have allowed for the detection of multiple virus pathogens in under 15 minutes, with initial trials showing tests for denuge, MERS, ebola and zika all carried out at once, within a multichannel microfluidic device[27]. The bodily fluid (usually blood or saliva) travels along a number of channels, where it then meets a number of virus specific reactants. If the virus is present, a reaction then occurs and there will be a visible change in the solution, such as a colour change or fluorescent signal. This positive signal alerts the user that a virus is present. Other designs have been used to test for diseases like cancer[28], HIV[29] and cardiac diseases[26].

In the past decade paper-based microfluidic systems have been demonstrated as a cheap and easily disposable alternative to standard POC microfluidic devices[30]. A hydrophobic paraffin pattern is injected into the paper, which creates discrete hydrophilic channels. Due to the capillary action of the paper, fluids can travel along the channels (without a pump) into regions where they meet reactants, which will provide either a positive or negative signal[31]. This method has been used to create cheap tests for diseases such as malaria[32] and tuberculosis[33] and has the potential to revolutionise POC testing in the developed world[34].

The remaining two fields, droplet microfluidics and single cell microfluidics are discussed in more detail in **Sections 1.3** and **1.4** respectively.

1.2 Microscopy

It is important to have the ability to observe and take measurements within the microfluidic device and so many experiments are performed within a microscope setup[35,36]. The components such as the objectives, illumination sources, detectors and cameras must be carefully chosen for each specific experiment so that the imaging of the cells, particles or droplets within the device is optimised. The magnification used within the system must provide a resolution which allows the target features or the region of

interest to be observed and the illumination within the microfluidic setup must provide sufficient light so that the experiment can be imaged by the cameras. It is important for the camera imaging the device to have a high frame rate to image flowing cells, particles or droplets, so there are no streaking artefacts which would compromise the measurements. In the case of multiple cameras, the light must be split so that the correct wavelengths are incident on the correct cameras; to achieve this, specific beam-splitters and filters can be optimised to block and direct the light down the correct beam paths, allowing for multiple wavelengths or regions of interest to be observed at once[37]. A microfluidic-microscope-camera setup can be used to take measurements of cell morphology to cell mechanics[38] and from cell phenotype to cell function[39]. This has made microfluidics a widely used tool in both cell biology[40–42] and medicine[43,44].

1.3 Droplet microfluidics

The miniaturisation of experimental techniques and the growth of lab-on-a-chip systems have stimulated interest in microfluidics where networks of micron scale channels move and manipulate liquids. However, in general, the high surface to volume ratio of such channels leads to strong interactions with the walls, which can result in unintended dispersion and mixing. By encapsulating the sample in a second immiscible phase, microdroplets can be produced within microfluidic networks. These two phases are known as the dispersed phase (which contains the sample) and the continuous phase. The immiscible continuous phase isolates each discrete droplet from those around it and eliminates direct contact with the walls. This provides a powerful platform capable of producing discrete reaction vessels for a wide variety of applications, including chemical[1,45] and biochemical reactions[46,47], library generation and screening[48,49], and nanoparticle fabrication[50,51].

Additionally, individual particles, cells or molecules, which can be manipulated freely in solution within the microfluidic walls, can also be encapsulated and isolated in microdroplets for studying them at the single level. Cells can be encapsulated individually or in small populations within the droplets, which act as small incubation vessels for the cells to grow and interact with each other[52]. This technique has been used to grow small microtumours from the aggregation of individual cells[53]. The cell-encapsulating microdroplet can be merged with secondary microdroplets containing reactants[54] such as nanotoxic particles[55], pharmaceutical drugs[56] or even coded assays for single cell analysis[54]. The effect of the reactants upon the cells can then be observed.

The small droplet volumes reduce sample waste[57] and the potential for high throughput allows multiple concentrations of reactants to be tested at once[58]. This allows for a wider range of tests per experiment compared to performing them in a well plate, which is limited by the number of wells in the plate, while also resulting in a more efficient use of reactants. The ability to encapsulate reactants and isolate them from external factors has acted as a beneficial extension to traditional techniques such as; polymerase chain reaction (PCR)[59], fluorescent cell sorting (FACS)[60] and single cell sequencing[61]. To generate these droplets in a controlled manner it is important to understand the factors that affect droplet formation.

1.3.1 Reynolds number

For a device to generate microdroplets there must first be at least two continuous, stable streams of immiscible solutions; for example hydrophobic oil and hydrophilic water. Microfluidic channels allow for interesting flow patterns due to the laminar flow profile in the channels. This means the injected solutions will flow in parallel and will be co-flowing, with little mixing[62]. This is due to the laminar flow profiles within the microfluidic device. The motion of the liquid can be described by the incompressible Navier-Stokes equation (**Equation 1.1**)[63]. In this equation ρ is the density of the fluid, υ is the fluid velocity field, p is the pressure field, η is the kinematic viscosity and f represents any external forces present. The equation describes how the velocity field of a fluid changes with respect to space and time, by balancing the forces present in the system. The left term is the force due to the velocity field (both time dependent and spatial), -∇p is the pressure-gradient force, $\eta\nabla^2 v$ is the viscous force and f represents the external forces such as gravitation and electrical forces. This equation can be simplified by substituting for the non-dimensional parameters. This leads to the non-dimensional Reynolds number (**Equation 1.2**) which provides the ratio of inertial and viscous forces.

$$\rho(\partial_t \boldsymbol{v} + (\boldsymbol{v} \cdot \boldsymbol{\nabla})\boldsymbol{v}) = -\boldsymbol{\nabla} p + \eta\nabla^2 \boldsymbol{v} + f \qquad \textbf{(1.1)}$$

$$Re = \frac{\rho U H}{\mu} \qquad \textbf{(1.2)}$$

In this equation Re is the dimensionless Reynold's number, ρ is the density of the liquid flowing in the channel, U is the mean flow velocity, H is the channel dimeter (likely to be in microns)[64] and μ is the dynamic viscocity. Microfluidic channels with a Reynolds number <2300 will host a laminar flow while channels with a number ~ >2600 will contain turbulent flow, with fluid mixing as it propagates[65]. In microfluidics the viscous

forces dominate, giving a small Reynold's number and laminar flow. This allows microdroplets to travel in the direction of solution propagation, which provides a stable environment for microdroplet production. The droplets can remain in the centre of the channel, free from the shear forces and wetting effects of the channel walls[1].

1.3.2 Capillary number

The capillary number is important in understanding the behaviour of the two immiscible fluids within microfluidic devices and microdroplet production[66]. As the droplets are being generated on the microscopic scale, they have a large surface to volume ratio. In this situation two forces dominate; the interfacial tension between the dispersed phase and continuous phase, and the viscous stresses of the solutions. These two factors are in competition with each other during droplet production and the relative effect of the two are described by the dimensionless Capillary number seen in **Equation 1.3**[67].

$$Ca = \frac{\mu_v V}{\sigma} \quad \textbf{(1.3)}$$

The top terms describe the viscous stresses, where μ_v and V are the dynamic viscosity and characteristic velocity respectively; while the bottom term, σ, describes the interfacial tension between the two phases. When the top term dominates, due to large viscous effects, the dispersed phase is extended and dragged down the channel. The dispersed phase is more stable and is less likely to form a droplet and droplets which are formed are likely to be deformed[68]. On the contrary, when the bottom term dominates, the interfacial tension is large and so the dispersed phase wants to reduce its interfacial area, resulting in the creation of droplets with spherical ends[69].

The capillary number is useful in microfluidics as it can be calculated independently of the channel dimensions. Although, channel dimensions can play a part in the velocity of the liquid[70], which in turn effects the capillary number.

1.3.3 Surfactant for droplet production

As described above, to generate spherical droplets the interfacial tension must be the dominant force. But when the interfacial tension is too large, droplets may merge together on contact to reduce their surface area[71,72]. To prevent this and to produce stable droplets, surfactants are used. These molecules contain affinities for both of the phases being used in the droplet production, for example water/fluorous oil droplets[73]. In this case, the surfactant molecule will contain a fluorophobic part and a fluorophilic part. The

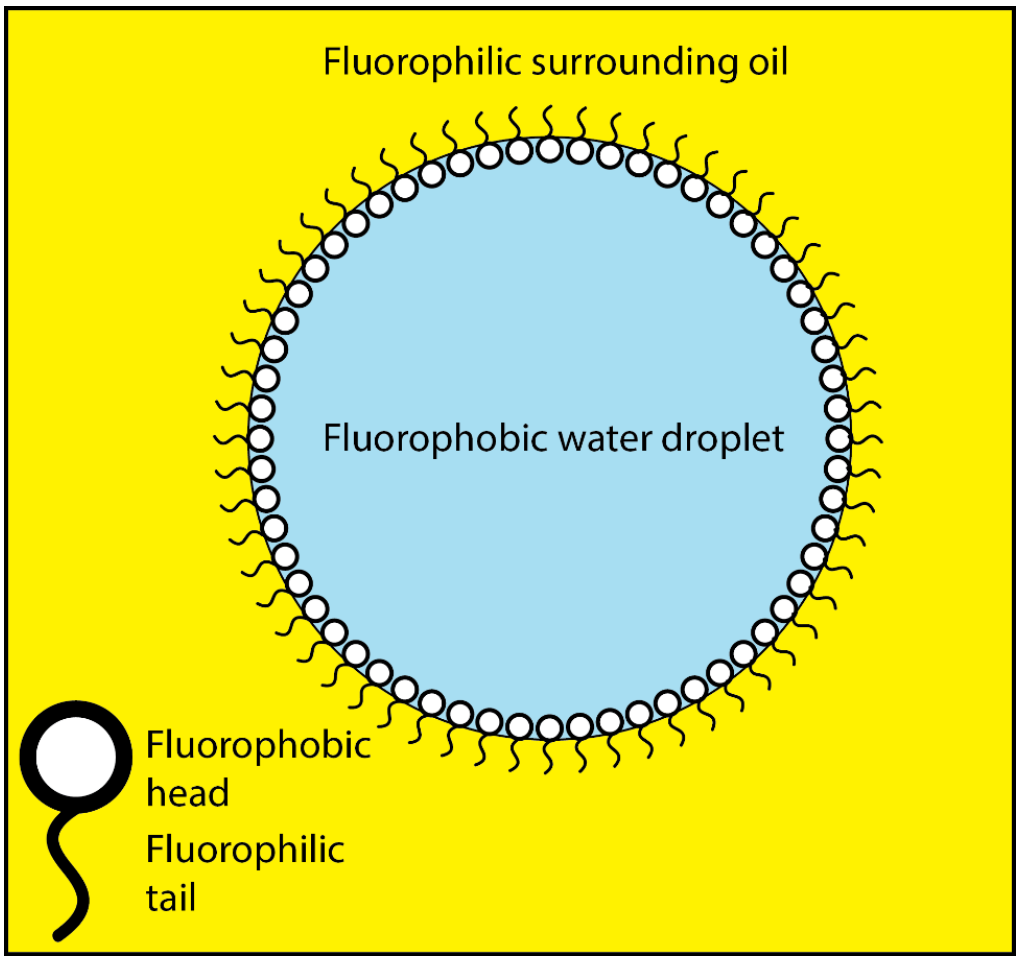

Figure 1.1 *Diagram showing the interaction of surfactant molecules on a water-oil interface. The fluorophobic heads face the water droplet while the fluorophilic tails face the surrounding oil, reducing the interfacial tension at the interface, allowing for more stable droplets.*

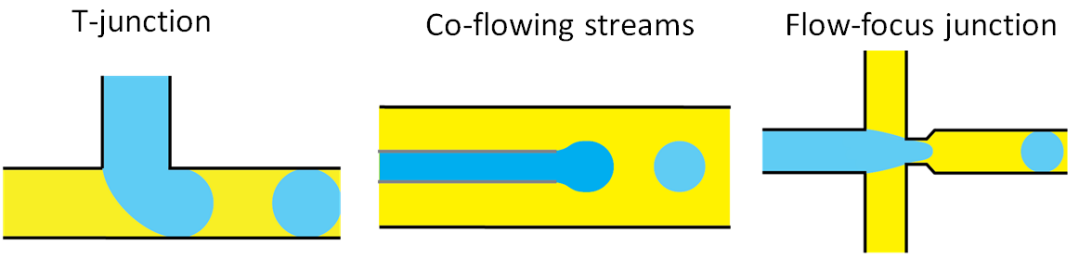

Figure 1.2 *The three device designs for microdroplet production; the T-junction, co-flowing streams and the flow-focus junction. Blue represents the dispersed water phase while yellow represents the continuous oil phase.*

term surfactant comes from the words 'surface active agent' and as the name suggests the molecules will be repelled to the edge of the droplets and will line up with the fluorophobic heads facing the water and the fluorophilic tails facing the oil, see **Figure 1.1**[74,75]. The concentration of surfactant within the solution determines the effect

on the surface tensions of the droplets; the greater the concentration, the lesser the interfacial tension and the more stable the droplets[76]. The aforementioned fluorous oils are popular within microdroplet production, as most organic compounds are insoluble within the oil[73]. The oils are also biocompatible which is vital for many common droplet uses[77].

1.3.4 Microdroplet generation designs

Microdroplet generation can either be continuous or on demand. In **Chapter 3** a method for continuous droplet production will be presented. There are three common continuous techniques: a T-junction, co-flowing streams or a flow-focus region. Images of the designs can be seen in **Figure 1.2**.

1.3.5 T-junction design

The first droplet production method, the T-junction design can be seen in **Figure 1.3**. The first solution is injected into a channel where it meets an orthogonal channel carrying a second immiscible solution at 90° in a 'T' shape. As the solutions cannot mix, microdroplets are formed due to shear stress and interfacial tension. There are two regimes in which the microdroplets are formed and they both are determined by the ratio of the two orthogonal channels[69], $x = w_{in}/w_{out}$. Where w_{out} is the width of the long channel in which the continuous phase and droplets propagate and w_{in} is width of the channel in which the dispersed phase is injected, the orthogonal channel. When w_{out} dominates and $x << 1$, the viscous shear forces cause the dispersed phase to elongate with microdroplets eventually breaking off before they can extend to the diameter of the full channel width, this is known as the 'dripping regime'. These spherical droplets are formed when the interfacial tension between the two phases is overcome by the shear stress, this happens at high capillary numbers. The droplet radius, and therefore volume is dependent on the interfacial tension between the two immiscible solutions, σ_{it}, the viscosity of the continuous phase, η, and the shear rate, $\dot{\varepsilon}$; it can be described as [78]: $r \sim \frac{\sigma_{it}}{\eta \dot{\varepsilon}}$. The shear rate is $\dot{\varepsilon} = \frac{2v}{w_{out}}$ where v is the velocity of the solution. Therefore, droplet size can be altered by changing the solution velocity.

The second 'squeezing' regime starts to occur when $x \sim 1$. As the droplet phase grows within the outlet channel it obstructs the channels walls, restricting the continuous phase from flowing down the outlet channel. The reduction in size of continuous phase carrying channel causes an increase in the pressure upstream of the droplet. This causes

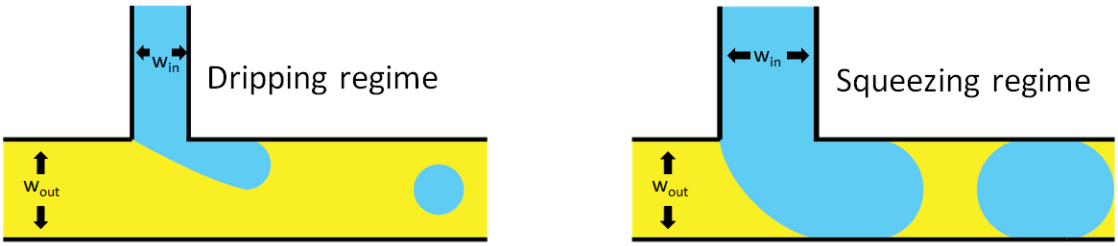

Figure 1.3 *Two regimes found in microdroplet generation within a T-junction design. If the ratio of the inlet width to outlet width w_{in}/w_{out} is <<1, smaller droplets will be produced in the dripping regime. As the ratio approaches 1 then droplet production enters the squeezing regime where larger plugs are generated. Blue represents the dispersed water phase while yellow represents the continuous oil phase.*

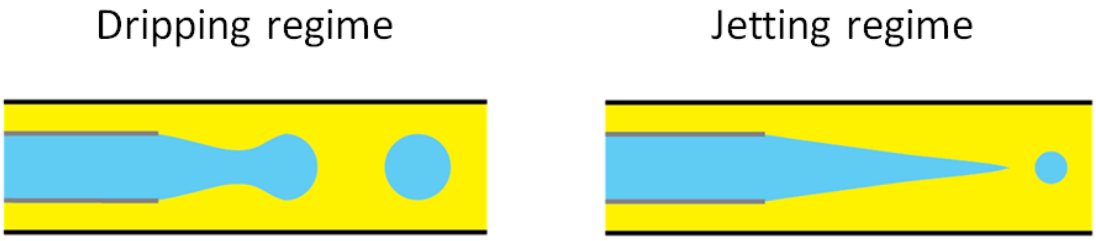

Figure 1.4 *The co-flow stream design involves a capillary (grey lines) being inserted into a microfluidic channel (black lines) and the dispersed and continuous phases are injected into the two spaces respectively. Droplet formation is dependent on the flow rates of the phases; if the continuous phase flow rate is low then droplets are formed at the tip of the capillary in the dripping regime, as the flow rate is increased droplets are formed further away from the capillary in the jetting regime. Blue represents the dispersed water phase while yellow represents the continuous oil phase.*

the droplet phase to neck and then break off from the orthogonal channel, creating a plug, a nonspherical droplet[79]. The length of the plugs produced is independent of viscosity, but is proportionally dependent on the ratio of the flow rates of the continuous and dispersed phases[79]. There is an intermediate stage where x<1 and the shape of the droplets produced is dependent on the both the shear stress and viscosity of the solutions (as seen previously in the dripping regime) and the confinement of the channel walls[80,81].

1.3.6 Co-flowing stream design

The T-junction and flow-focus junction, described in **Section 1.3.7,** droplet generation designs both involve multiple channels within a microfluidic device. The co-flowing stream technique is less complex and involves inserting a glass capillary into a single microfluidic channel. The continuous phase is injected into the microfluidic channel, while the dispersed phase is injected into the capillary. Towards the tip of the capillary, both the glass and channel walls are parallel creating two co-flowing

solutions[82]. As long as the interfacial tension is overcome by the shear stress, the solution from the capillary breaks into individual droplets in one of two regimes, dripping and jetting (**Figure 1.4)**[83]. Dripping occurs when droplets are formed close to the capillary, while jetting occurs when the droplets are formed further away from a thinning stream of dispersed phase. Assuming the viscosity and interfacial tensions of the two phases remain constant; the droplet production changes from the dripping phase to the jetting phase once the velocity of the continuous phase is increased beyond a certain threshold, this is the Rayleigh–Taylor instability, which occurs when a lighter fluid (oil) is pushing a heavier fluid (water)[84]. If the aforementioned velocity is increased further, droplets are generated further and further from the capillary and eventually there will be no droplet production, only co-flowing streams of the dispersed phase surrounded by a continuous phase[85]. When the flow rate of the continuous phase is <10 times larger than that of the continuous phase it is possible to alter droplet volume by adjusting the input flow rates[86]. However, this changes the frequency of droplet production. Currently, it seems both droplet volume and frequency cannot be adjusted in unison using this method. Recently work has been done to model the variables present in droplet formation to accurately predict droplet volume[84].

1.3.7 Flow focus design

The remaining widely used droplet production method is the flow focus design. Two opposing, perpendicular continuous phase channels meet a dispersed phase channel. The solutions flow into a narrower chamber which expands into an output channel. Microdroplets are produced in one of five regimes; squeezing, dripping, jetting, tip-streaming and tip-multi breaking, all of which are illustrated in **Figure 1.5**[15].

Squeezing regime

The squeezing regime occurs at low capillary numbers (Ca < 0.01) where the interfacial tension term dominates and unlike the latter four regimes, it does not rely on the Rayleigh instability to generate microdroplets[87]. The dispersed phase protrudes into the flow-focus junction and grows; meanwhile, pressure from the two intermediate flows builds on either side of the dispersed phase. This gradually reduces the distance between the two opposing continuous phases. Once the pressure from the continuous phases overcomes the pressure inside the droplet, the interface is squeezed and necks into a fully formed droplet. In this regime the droplet will generally be a plug, with dimensions

controlled by the channel geometry[88]. This method is known to produce droplets with a high degree of monodispersity[89].

Dripping regime

At higher capillary numbers (Ca > 0.01), the viscosity term starts to play a roll over the interfacial tension forces, which previously prevented the emerging droplets from breaking up, and droplet production moves into the dripping regime[87]. The two phases are forced through the narrow chamber which results in the two outer, continuous solutions applying pressure to the inner dispersed phase. This results in the dispersed phase elongating into a thin cylindrical shape[90]. Due to the perturbations in the stream, the dispersed phase becomes unstable due to increasing surface tensions and, as the Rayleigh instability predicts, the fluid breaks into individual droplets. These droplets will either be created within or after the narrow chamber, the position of generation is determined by the capillary number[1].

Jetting regime

Once the capillary number is above a certain threshold the dripping regime changes into the jetting regime (**Figure 1.5j)**. As the name suggests a long jet is produced, extending from the narrow chamber and this happens at high flow rates of the dispersed and continuous phases, Q_d and Q_c. Similarly to the dripping regime, the Rayleigh instability causes the tip of the jet to break off into individual droplets[91]. The droplets produced have low levels of monodispersity with coefficient of variation, CV, (explained in **Section 1.3.14**) values of ~ 6% being recorded. This is due to perturbations in capillary number as the liquid moves through the system[92]. This system is therefore not the best for producing consistent monodispersed droplets.

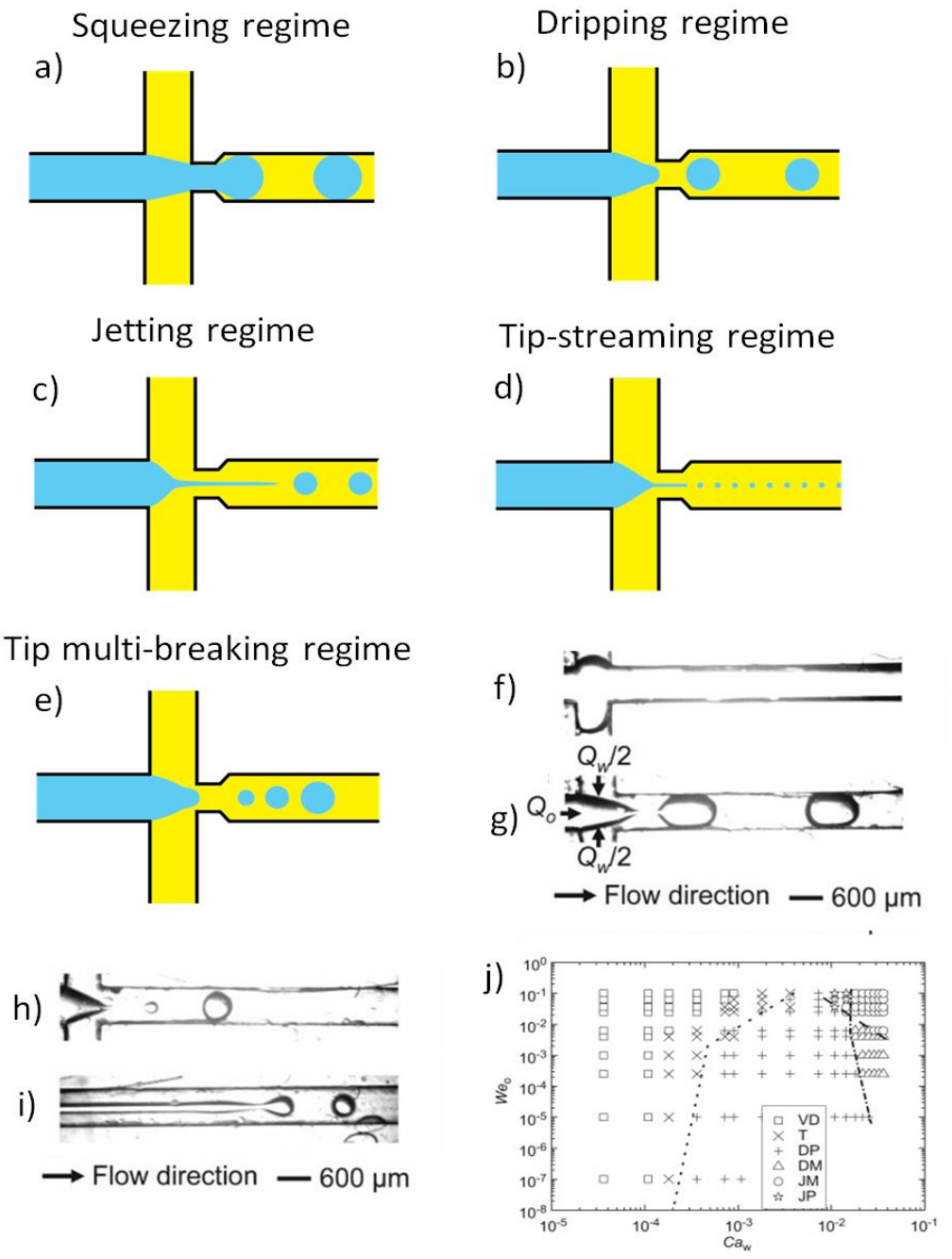

Figure 1.5 (a-e) *Show the five regimes that can be achieved in the flow-focus junction design; the squeezing, dripping, jetting, tip-steaming regimes and tip multi-breaking. Blue represents the dispersed water phase while yellow represents the continuous oil phase. (**f-i**) show images of droplet production:* **(f)** *Tubing regime where no droplets are produced [T],* **(g)** *Dripping plug [DP],* **(h)** *Dripping monodispersed droplet [DM],* **(i)** *jetting monodispersed droplet [JM].* **(j)** *Flow pattern map where We and Ca are the webber and capilary number respectively. The dopped line represents the transition between the tubing and dripping regimes; the dashed line represents the transition between dripping and jetting regimes; the dashed and dotted line represents the transition between the plug and monodispersed droplets. At high capilary numbers droplets and plugs are generated, jetting is observed at lower Ca values and no droplet production is seen at very low Ca values. (**f-j**) are reprinted from, Chemical Engineering Science 84, Fu, et al, "Droplet formation and breakup dynamics in microfluidic flow-focusing devices: From dripping to jetting",* ***207****, Copyright (2012), with permission from Elsevier*[93].

Tip streaming and tip-multi-breaking regimes

The final two methods tip-streaming and tip-multi-breaking are less commonly seen in microdroplet production. The former of the two occurs at specific channel geometries[94] when sufficient surfactant is present[95]. The dispersed phase is elongated into a conical shape with a thin stream emanating from the tip. Microdroplets break off from this stream[96]. Microdroplets on the femtolitre scale have been recorded with a relatively high degree of monodispersity, CV ~1.8[97].

The final regime, tip-multi breaking, is similar to tip-streaming in that a conical shape is formed from the dispersed phase. However, the cone is unstable and oscillates with multiple droplets breaking off the cone with each oscillation[98]. The droplets produced are polydispersed and are not continuous like the previous methods. However, the number and size of the droplets produced are repeated with each oscillation and can be predicted[99].

1.3.8 Choosing a design

Both the T-junction and flow-focus devices can be produced using simple PDMS moulds (described in **Section 2.1.3**), unlike the co-flowing junction which also requires a capillary to be carefully inserted into each device. For multiple experiments using multiple devices, the co-flowing design is therefore less favourable. Due to the nature of the T-junction, the dispersed phase is stretched along the outlet channel wall during droplet formation which can cause issues such as wetting. This is when the water maintains contact with the channel wall and therefore droplets cannot be formed. Flow-focus designs by contrast generate droplets in the middle of the channel and therefore avoid wetting problems, allowing smaller droplets to be produced. Other multi-layer droplet generation designs are available, but require complex multi-stage master creation (single stage master creation described in **Section 2.1.2**). Due to the combination of the ease of device manufacturing and the range of producible droplet volumes, the flow-focus junction was chosen for droplet generation in **Chapter 3**.

1.3.9 Droplet volume calculation

Predicting and measuring droplet volume within the flow focus devices is important in many experiments, such as cell encapsulation, where the wrong droplet size may result in an incorrect number of cells per droplet[100]; and reagent mixing, where incorrect volumes will invalidate the results of any measurements[101]. To confirm the droplet volume is as expected it can be imaged and one can measure parameters such as

the droplet radius, length and width[102]. In a large enough channel where the channel depth and width are greater than the droplet length, D, the droplet will be spherical and so the droplet volume, V, can be calculated using the sphere volume calculation, **Equation 1.4**.

$$V = \frac{\pi D^3}{6} \quad \textbf{(1.4)}$$

In some cases the droplet produced may have dimensions larger than the channel width and/or height which causes the length of the droplet to be longer than its width, this is called a plug[103]. When this happens the below approximation **(Equation 1.5)** is used to calculate the droplet volume. This can be calculated by finding the volume of both the plug and the two caps (ends of the plug). Each cap is estimated to have the volume of a hemisphere. The volume of the main body is calculated using the cross sectional area of the plug; this changes depending on if the plug is flattened by either the side or bottom walls (or both). By adding these three volumes together, the below equation is achieved.

$$V = \left(HW - \frac{H^2W^2(4-\pi)}{4(H+W)^2}\right)\left(L - \frac{W}{3}\right) \quad \textbf{(1.5)}$$

The volume of the droplet, V, is calculated using the channel height, H, channel width, W, and the length of the droplet, L. This equation has been calculated theoretically and confirmed experimentally[104,105].

1.3.10 Controlling droplet volume

As described previously, microdroplets have a number of applications and in many of these applications, having an accurate and controllable droplet volume is important. It is therefore important to be able to adjust droplet volume in flow and to maintain a high level of monodispersity. Droplet volume is dependent on a number of factors: the viscosities and interfacial tension between the two phases, the device geometry, the temperature of the solutions and the flow rates of the solutions. Models have been developed to predict droplet volume, using the above parameters, and recent studies have been able to predict droplet volume[15,106,107].

$$\frac{V}{(hw_c^2)} = a_{lag} + a_{fill} + \zeta_{neck}\varphi \quad \textbf{(1.6)}$$

An example of such a model can be found in **Equation 1.6**, which describes a method used for calculating the volume of microdroplets in a T-junction device[107]. V is droplet volume, h is channel height, w_c is channel width; α_{lag}, α_{fill} and $\zeta_{neck}\varphi$ are normalised volumes added during the lag and filling stages of droplet production and the dimensionless necking time. Even though this equation takes multiple parameters into account, it can only generate droplets within 10% of the predicted volume. This

highlights the difficulty and impracticality of predicting droplet volume when there are so many variables, some of which are not trivial to measure within the microfluidic device, such as temperature.

1.3.11 Active droplet generation

Microdroplet size control can be either passive or active. Active microdroplet production involves using external appliances to impart additional energy into the system, which in turn creates droplets. The droplets can be created using piezoelectrics[108], pneumatic valves[109], optical heating elements[110] and generated electric fields[111]. Droplets can be produced on demand and the frequency and magnitude of the external energy imparted into the microfluidic system dictates the frequency and volume of the droplets.

1.3.12 Passive droplet generation

Passive droplet generation, as the name suggests, does not make use of external energy sources and uses continuously flowing liquids and produces droplets in one of the five regimes described in **Section 1.3.7**. Changing channel geometries or liquid properties are two ways of passively controlling droplet production[106], but the easiest way to do so is by changing the flow rates of the liquids[112]. Unlike the other methods, this can be done in flow. It has been shown that both the volume and frequency of microdroplet production are dependent on the flow rates of both the dispersed phase, Q_d and the continuous phase, Q_c[112]. Using one of the two main configurations of fluid input, syringe pumps and pressure-based pump systems, these flow rates can be controlled[113,114]. By controllably changing the flow rates both the droplet volume and frequency can be controlled[115], but a recent review paper by Zhu, et al (2017) suggests that "it is almost impossible" to control both droplet volume and frequency using a passive method and that changing droplet volume can take "several seconds or even minutes"[15].

1.3.13 Pressure-based pumps and syringe pumps

To generate droplets, the two immiscible solutions must first be injected into the microfluidic device. Two commonly used methods, which are compared in **Chapter 3**, are syringe pumps and pressure regulator based systems. The former of the two involves a syringe which is connected, usually via tubing, to the microfluidic inlet. The syringe is secured onto the syringe pump and a moving pusher block pushes the plunger into the syringe at a constant speed, providing a constant flow rate for the solution. A motor

within the syringe pump drives the pusher block and moves in individual steps, increasing the pressure within the syringe, which in turn causes the solution to flow out of the syringe and into the inlet[116]. The stability of this flow is related to the magnitude of each step; if the steps are small there will be many steps and the flow rate will be smooth, if the steps are large then for the same flow rate there will be less steps in total and there may be pulses or oscillations in the flow rates[117]. As microfluidic experiments use small volumes of liquid and therefore low flow rates, this pulsing can cause issues such as oscillations in the microdroplet volume. To combat this, "pulseless" syringe pumps which have hundreds of thousands of steps per motor revolution can be used; and although there will still be discrete steps, the limit of the flow rates for which the syringe remains pulseless is reduced.

Another method commonly used to regulate flow rates within microfluidic devices is to impart pressures on to a vessel containing the solution, usually connected by tubing to the microfluidic device, using pressure regulators; this results in the solution travelling up the tubing and into the device. The pressure in the vessels can be maintained and altered by the regulator; internal valves in the regulator are adjusted into a pre-calibrated configuration that converts a high external input pressure into the required lower outlet pressure. Although there are still moving parts within the regulator itself, shorter response times are observed when compared to syringe pumps, the latter of which can take seconds or minutes to respond to changes in infusion rate[118]. This results in a higher droplet monodispersity on small time scales[119]. However, over long times the backpressures within the pressure pump system can change, resulting in a change of liquid flow rates which in turn dictates droplet volume[119]. Due to the aforementioned oscillations present in syringe pump based systems, pressure-based pumps have been more effective in producing monodispersed droplets[120].

1.3.14 Coefficient of variation

The accepted method of measuring droplet monodispersity is the coefficient of variation,

$$C_V = \frac{\sigma}{\mu} \tag{1.7}$$

where σ is the standard deviation and μ is the mean droplet volume. This can also be described as the relative standard deviation. Previous studies have described the standard coefficient of variation for a pressure-based system to be just under 3%[121] and studies in recent years have struggled to achieve a $C_V \sim 1\%$ [122–125].

1.4 Cell Sorting

Cells are inherently heterogeneous, both at a cellular and nucleosomal level and the ability to separate large heterogeneous populations into smaller more homogeneous subpopulations is an important tool for many disciplines such as medical diagnosis[126], therapeutics[127] and single cell genomics[128]. The ability to identify and isolate different cell types is called cell sorting.

In 1965 the first cell sorter was built by Fulwyler, using inkjet printing technology which was new at the time, and involved isolating cells of different volumes within charged droplets and using electrostatic fields to direct the cells into the relevant subpopulation vessels[129]. The first commercial cell sorter was invented in 1969 by Herzenberg and was an advancement of Fulwyler's technology[130]. A large number of cells flow through a single/multiple laser beams and the scatter of the light is detected and used to determine the cell type present. The cell is then directed into the relevant sub population using the same method used by Fulwyler. The cells are labelled with fluorescent markers and hence the technique is called Fluorescent Activated Cell Sorting, FACS. This technique has evolved over the decades and has become a cornerstone in cell sorting technology with throughputs of over 100,000 cells per second[131], but it does have some drawbacks.

FACS sorters are usually large and expensive pieces of equipment which require significant effort to prevent contamination[132], they require technical expertise to run and maintain[133] and most importantly there are worries that there could be biohazard risks due to the cells being encased in aerosols[42]. An emerging cell sorting technique which aims to address these issues, while maintaining the high flowrates and efficiencies of current FACS sorters, is microfluidic cell sorting[134]. Microfluidic devices are already a proven platform for cell manipulation[135] and cells can both be detected and maneuvered in the devices, either within microdroplets[47] or free in cell media or PBS[136]. Different designs of microfluidic devices and techniques of cell sorting have been invented to optimise sorting for different cell types, including a FACS microfluidic technique[3].

1.4.1 Methods of microfluidic cell sorting actuation

There are a number of available methods for microfluidic cell sorting but they can all be defined into two broad categories, passive and active. Passive cell sorting makes use of specifically designed channel dimensions and designs to create hydrodynamic forces, which allow the separation of cells depending on morphological differences such

as size and density. Active sorting involves external mechanisms to impart forces to separate the cells. Examples include acoustic waves, magnetic fields and electric fields.

1.4.2 Passive cell sorting

The simplest form of cell sorting is passive cell sorting. These methods can be high throughput, with 100,000s of cells being sorted per second[137]. One of the benefits of this method is also one of its main disadvantages; cells can be sorted without fluorescent labels, but only inherent cell properties such and size and density can be analysed. Cells are sorted using inertial flow focusing, filtration and hydrodynamic forces. These methods are discussed in **Section 1.4.3** and **Section 1.4.4.**

1.4.3 Inertial flow focusing

Inertial flow focusing within microfluidic devices makes use of the laminar flow of the cell solution, where due to the low flow velocities, the movement of the fluid is smooth and orderly. The velocity of the fluid is greatest at the centre of the channel and effectively zero at the channel walls[138]. In laminar flow systems curved channel walls can be used to employ inertial forces onto the cells in solution. These forces act on the cell in the direction of the inner channel wall. These curved channels can be designed into a spiral or serpentine pattern. A spiral design imparts a larger force on larger cells and smaller forces on smaller cells (**Figure 1.6a)**[139]. By imparting these forces over a longer distance the cells will separate, with larger cells gravitating towards the inner channel wall[140]. The larger the cell the closer it will be to the channel wall. At the end of the spiral, the channel widens into multiple parallel outlets. The cells will then flow into different outlets depending on their size (**Figure 1.6b)**. Multiple cell types can be separated at once using this method[141]. This technique has been widely used, one example being the separation of tumour cells from blood samples[142]. Recently modified spiral channels have used micro-obstacles and extra corners to increase the efficiency and throughput of cell sorting. The micro-obstacle method has achieved a yield of >90% and a throughput of 2.5 mL/min[143], while the spiral channels with added corners achieved a yield of 99.8%, a purity of >85% and a throughput of 3mL/min[144].

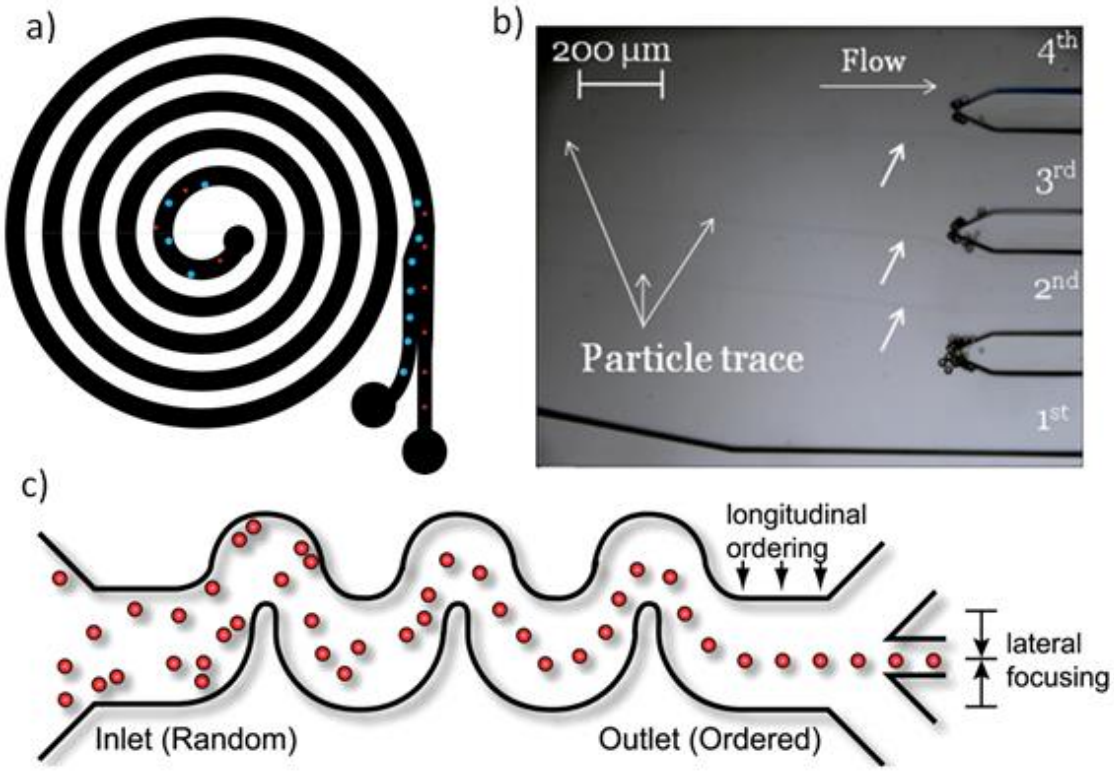

Figure 1.6 **(a)** *A spiral inertial flow focusing channel which is sorting large (blue) and small (orange) cells. The larger cells experience a larger force compared to the small cells and move towards the inner channel to be sorted into the leftmost outlet, while the small cells continue into the rightmost outlet.* **(b)** *Particles of differing sizes being sorted into four outlets using a spiral inertial focusing device.* **(c)** *Serpentine inertial flow focusing channel diagram with cells arriving scattered across the width of the channel being focused into the middle of the channel by the time they reach the outlets. Figure (**b**) Reprinted by permission from Springer Nature: Journal of Mechanical Science and Technology, "Focusing and sorting of multiple-sized beads and cells using low-aspect-ratio spiral microchannels", Thanormsridetchai, et al, (2017) Figure (**c**) Reprinted from, PNAS 104, Di Carlo, et al, "Continuous inertial focusing, ordering, and separation of particles in microchannels", 18892, Copyright (2017) National Academy of Sciences, with permission from PNAS*[145]

Making use of similar forces, a serpentine channel has been used to separate cells of varying sizes (**Figure 1.6c**). The sudden changes in direction within the channels cause the flowing solution to lose momentum at the turns, imparting an inertial lift force which in turn creates an opposing accelerating force on the liquid[146]. This secondary drag force leads to vortices, or Dean flows, in the serpentine channel[147]. The cells are acted upon by these two forces and experience varying resultant forces depending on cell size, which separates the cells within the channel perpendicular to the direction of propagation[145]. The serpentine design has been used to sort cells at a rate of 1mL/min but there is less recent work using the technique when compared to the aforementioned spiral design[148]. The design is also useful for focusing cells into the middle of the channel for flow cytometry[149].

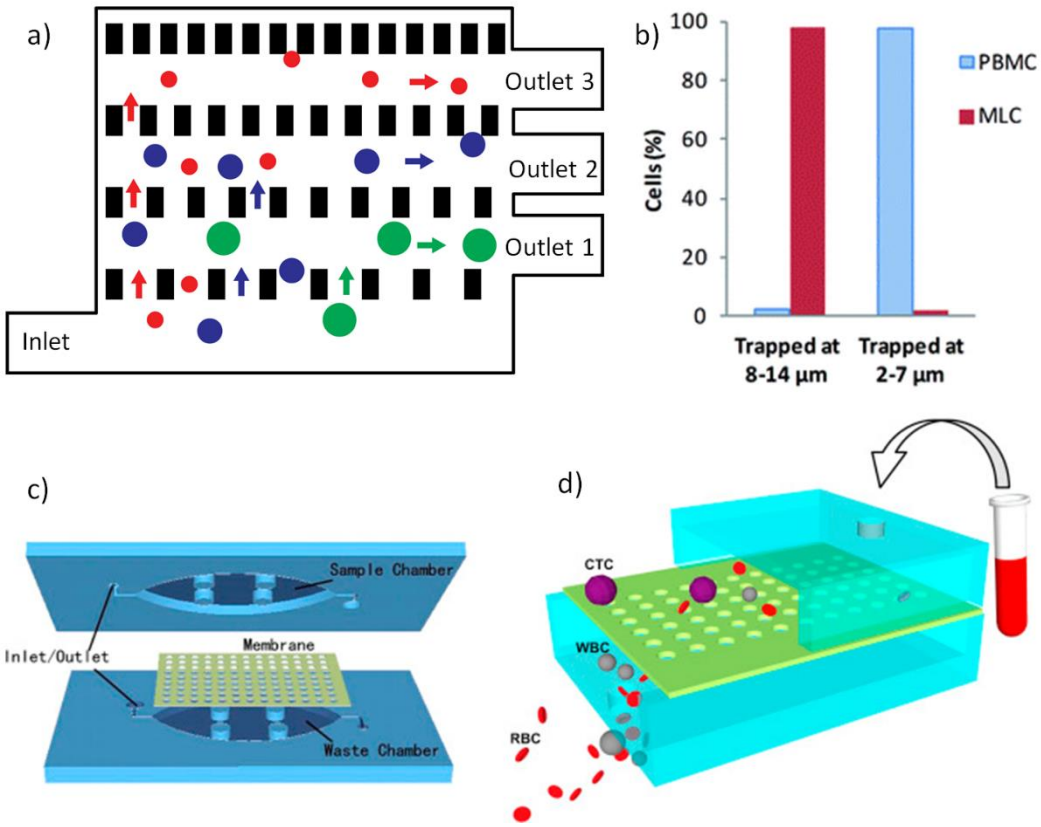

Figure 1.7 (a) *Schematic of a pillar based filtration cell sorting device where the distance between pillars decreases with each iteration, trapping larger cells earlier and letting smaller cells pass. The cells can then be sorted into multiple outlets depending on their size and elasticity.* **(b)** *Results of filtration sort of small peripheral blood mononuclear cells (PBMC) and larger mouse lymphoma cells (MLC) with purities of 95% and 99% respectively.* **(c)** *Top down lateral sorting device with membrane for trapping large cells and allowing small cells to pass.* **(d)** *Diagram of top down device in action, detecting cancer, where CTC cells are trapped and RBCs and WBCs pass through. Figure (**b**) reprinted from, Lab on a Chip 13, McFaul, et al, "Cell separation based on size and deformability using microfluidic funnel ratchets", 2369, Copyright (2012) Royal Society of Chemistry, with permission from the Royal Society of Chemistry* [150]. *(**c-d**) Reprinted from, Biosensors and Bioelectronics 71, Fan, et al, "A microfluidic chip integrated with a high-density PDMS-based microfiltration membrane for rapid isolation and detection of circulating tumour cells", 380, Copyright (2015), with permission from Elsevier*[151].

1.4.4 Filtration

Not unlike other methods of filtering, cells can be separated due to their size by implementing channel features into the device design. The simplest technique is to use arrays of pillars with varying separations as seen in **Figure 1.7a**[152]. The cells enter the sorting region at the bottom and are enacted upon by two flows. One flow pushes the cells into the pillar arrays, while the other flow moves the cells perpendicular to the pillar arrays, along to the numerous outlets between each array. This is known as a cross flow junction. Each iteration of pillars are closer together. Smaller or more elastic cells will

pass through more arrays while larger or less elastic cells will not be able to pass. Once a cell cannot progress any further through the pillars it will be moved along into one of the outlets. The cells can therefore be sorted into numerous subpopulations in one experiment (**Figure 1.7b)**[150,153]. A common issue with filtration is that the pores are prone to clogging, with cells getting stuck, preventing more cells from being sorted[154]. To prevent this from happening recent designs have implemented multiple microfluidic device layers for top down, lateral sorting (**Figures 1.7c and 1.7d)**[151]. The cells are injected above the top layer. Smaller cells can pass down into the bottom channel, while larger cells cannot pass. There are outlets for the top and bottom channels at the sides of the channels. If large cells start to clog the pores a positive pressure is applied from the top outlet to detach the cells. A negative pressure is then used to remove the cells from the channel without disrupting the smaller cells which have already passed the membrane[155]. Due to the high throughput of this method it is useful for isolating white blood cells[156], circulating tumour cells (CTCs)[151], and bacteria[157] from blood.

1.4.5 Magnetic activated cell sorting (MACS)

The previously described methods of passive cell sorting only allow cells to be separated into populations determinant on cell size and deformability. This limits the number of potential applications. A method that allows more specific cell sorting, by identifying the antigens on the cell surface, is magnetic activated cell sorting (MACS). Antigens are proteins found on the surface of cells, which only bond to specific antibodies (another protein), like a lock and key. MACS uses magnetic beads, usually iron, which are coated with a specific antibody which will bind to antigens on the target cells[158]. After these particles have been incubated with the cells, magnets can be used to attract the beads and recover the required cell type while the unbound cells can be washed away[159,160]. It could be argued either way that MACS is an active or passive method of cell sorting. The magnetic particles are actively bound to the cells but after this binding step, the cells are passively flown through the magnetic field.

Initial applications of MACS were performed without microfluidic chips and have been used in a wide variety of cell isolation and purification techniques including locating rare CTC cells[161] and removing damaged sperm cells to improve fertilisation[162]. In the past 15 years this technique has been adapted into microfluidic chips to further increase its potential.

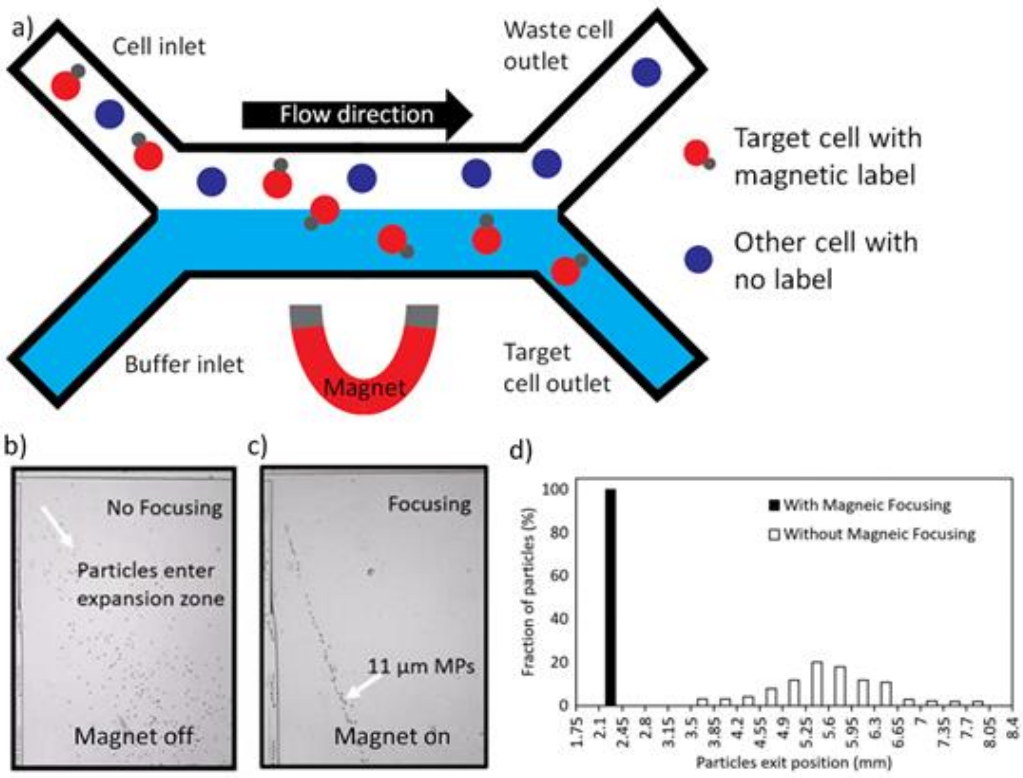

Figure 1.8 (a) *Diagram of MACS device. The cell inlet and buffer inlet causes all cells to move towards the waste outlet unless the magnet is on, in that case the cells with magnetic labels are drawn towards the magnetic field and will flow into the target cell outlet.* **(b)** *Image of magnetically labelled particles flowing into a microfluidic channel with the magnet off. The particles flow from the top left to the bottom right of the channel.* **(c)** *Particles flowing in the same channel as* **(c)** *but with the magnet on, in this case the cells line up and reach the bottom of the channel at roughly the same lateral position.* **(d)** *Lateral exit position of cells both with (black) and without (white) the magnetic focusing. With the focusing almost 100% of the cells are in the same 350µm position and without the magnetic focusing, the cells are randomly distributed.* ***(b-d)*** *are reprinted by permission from Springer Nature: Biomedical Microdevices, "Magneto-Hydrodynamic Fractionation (MHF) for continuous and sheathless sorting of high-concentration paramagnetic microparticles" Kumar, et al, (2017)* [163]

Magnetic cell sorting was first introduced into microfluidic devices in 2004 where cells passed through a channel with a perpendicular magnetic field. Cells with attached iron microspheres are deflected while those without continue in the direction of laminar flow (**Figure 1.8)**[164]. This method only works for two cell types, those with the microsphere attached and those without. To combat this, different sizes of microspheres can be attached to different target cells, which leads to different trajectories when passing the magnetic field; by taking advantage of these trajectories the cells can be removed at up to 25 different outlets[165,166]. The throughput of microfluidic MACS is relatively high when compared to other methods with rates in the tens of thousands of cells per second[163,167]. This has allowed bacteria to be removed from whole blood at rates of 60

mL/hr[168]. A downside of this method is that it requires an external label being attached to each cell which may alter the viability of the cell. It is also is difficult to remove the magnetic beads from the cells post-sort and this may or may not remove the antibody, both of which may alter the measurement of cell properties[168]. As each cell needs an antibody-coated magnetic bead this technique may become expensive when sorting a large number of cells.

1.4.6 Active cell sorting

Active cell sorting relies on external forces to alter the trajectories of cells. The throughputs can be high, with 100,000s of cells sorted per second; and unlike passive methods, active sorting can make use of fluorescent labels to target a wider range of cell subpopulations. Active sorting involves two steps: the detection of a cell or fluorophore and the actuation of the sort. The same cell detection method can be used with various sorting actuation methods. The fluorophores used will be discussed in **Section 1.5** and below the various methods of physically sorting the cells will be discussed. These methods include: acoustophoresis, dielectrophoresis, optical methods and micro-electro-mechanical sorting (MEMS).

1.4.7 Acoustophoresis

Acoustic cell sorting, or acoustophoresis, involves the manipulation of cells using acoustic radiation. Piezoelectric transducers are used to create standing waves which alter the pressure within microfluidic channels. The nodes of the wave create regions of constant pressure while the antinodes create regions which alternate between a maximum and minimum pressure. These alternating waves are created when waves of a specific frequency travel in opposite directions. Different varieties of these waves can be created, namely bulk acoustic waves (BAWs) and surface acoustic waves (SAWs).

BAWs occur when standing waves are produced and line up with the walls of the microfluidic channel, creating a node or antinode in the centre of the channel[169]. Cells entering this region experience a force. The magnitude of the force is dependent on the size and shape of the cell and the direction is determined by the size, density and compressibility of cell[170]. The movement of the cell is described by the acoustic contrast factor, φ, (seen in **Equation 2.1)** a value which is also dependent on the properties of the surrounding medium[171]. β and ρ represent the compressibility and density of the particle (c) and medium (w) respectively.

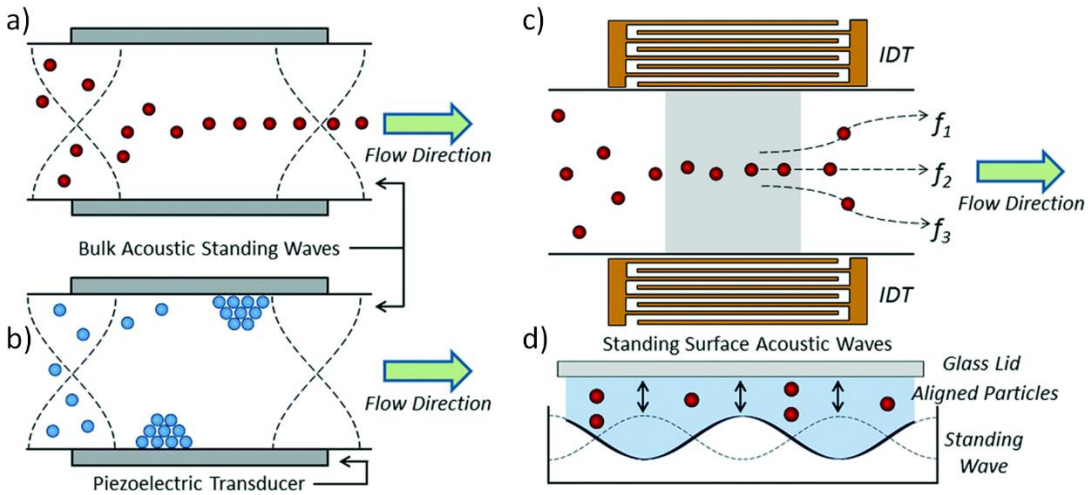

Figure 1.9 (a) *Particles being focused in the middle of the microfluidic channel using Bulk Acoustic Waves (BAWs). The particles have a positive φ value and so migrate to the pressure nodes.* **(b)** *Conversely to* **(a)** *the particles have a negative φ value and therefore migrate to the antinodes at the channel walls.* **(c)** *Surface Acoustic Wave (SAW) sorting where interdigitcal transducers (IDT) use multiple driving frequencies to focus cells into specific flow paths and into various outlets.* **(d)** *Cross section of SAW device showing the pressure waves within the microfluidic device. This figure is reprinted from, Lab on a Chip* ***15****, Wyatt Shields, et al, "Microfluidic Cell Sorting: A Review of the Advances in the Separation of Cells from Debulking to Rare Cell Isolation", 1230, Copyright (2015) Royal Society of Chemistry, with permission from the Royal Society of Chemistry* [42].

$$\varphi(\beta,\rho) = \frac{5\rho_c - 2\rho_w}{2\rho_c + \rho_w} - \frac{\beta_c}{\beta_w} \qquad \textbf{(2.1)}$$

A positive value of φ results in the cell moving towards the node (**Figure 1.9a)** and a negative value of φ results in the cell moving towards the antinode (**Figure 1.9b**). By positioning the antinodes at the channel walls, a node at the centre of the channel cells will be directed to the middle or edge of the channel. If the two cell types have positive and negative φ values they can be passively sorted, with the waves being produced constantly[172]. But to sort more similar cell types, the acoustic wave can be turned on when a target cell is present and the cell will be directed to the middle or edge of the channel and into the sorting outlet[173,174].

Fluorescent activated cell sorting has been performed using BAWs with throughputs of 150 cells per second[175]. The formation of these waves relies on high acoustic reflection from the microfluidic device. Unfortunately, low-cost polymer materials such as PDMS have poor acoustic reflection properties. As PDMS is widely used for rapid prototyping this makes it difficult to easily and quickly test new BAW-device designs[176]. An alternative acoustic focusing technique is surface acoustic waves or SAWs.

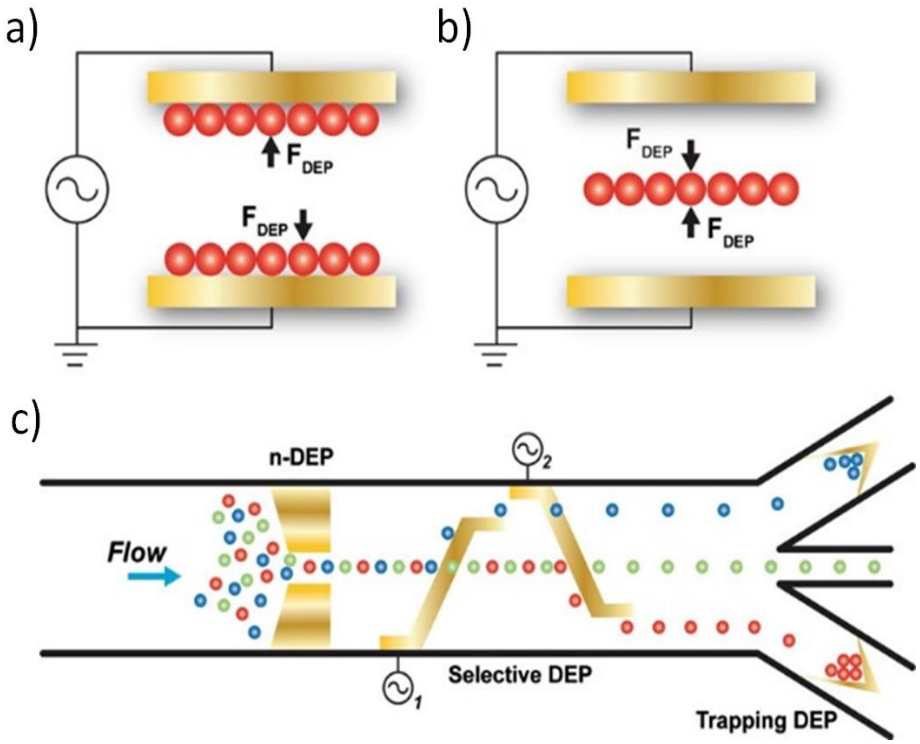

Figure 1.10 (a) *Diagram of positive Dielectrophoretic (pDEP) where an AC current is used to pull cells towards the electrodes.* **(b)** *Alternatively negative DEP (nDEP) can repel cells into the centre of the microfluidic channel.* **(c)** *Diagram highlighting the use of such techniques. Initially the cells are focused into the centre of the channel using pDEP and are then actively pulled towards the channel walls using two nDEP electrodes, allowing 3 cell types to be sorted. This figure has been reprinted from, Analytical and Bioanalytical Chemistry* ***397****, Gossett, et al, "Label-free cell separation and sorting in microfluidic systems", 3249, Copyright (2010) Springer-Nature, with permission from Springer Nature*[177].

These waves are produced along the floor of the microfluidic channel using transducers. They mechanically produce sound waves which allow for cells to be aligned into specific flow streams[178]. SAWs were first employed to help focus microparticles and cells into the middle of microfluidic devices in both 2D[179,180] and 3D[181]. This has been useful in cytometry where cells can be focused into centre of the laser beam, allowing for a more tightly focused beam which improves the resolution[182,183]. The SAW waves are either standing or travelling waves, SSAW or TSAW waves. With TSAWs the frequency of the wave can be altered to fine tune the sorting rate[184]. With SSAW only a fixed wavelength can be used[185]. These methods have been able to achieve cell sorting in the kilohertz regime[186,187].

1.4.8 Dielectrophoresis

Similarly to how MACS uses magnetic fields to manipulate the trajectory of cells, dielectophoresis, DEP, employs non-uniform AC electric fields. The field that the cells flow through is produced by integrated electrodes within the microfluidic channel which generate an alternating current, inducing dipole moments across the cells[188]. The cells will then move towards the region of strongest or weakest field intensity within the microfluidic channel depending on the electrical permittivity of the cell and the surrounding solution; if the cell has a greater permittivity than the fluid it will move towards the weakest region of the field and vice versa (**Figure 1.10a** and **Figure 1.10b**)[189]. The magnitude of this force depends on the size and dielectric properties of the cell or droplet[189]. By altering the voltage and frequency of the input signal, the force experienced by the cells can be changed, causing them to be positioned at different distances from the channel walls, which allows multiple cell subpopulations to be sorted into multiple (at least 5) outlets as seen in **Figure 1.10c**[190]. To reduce the damage to the cells imparted by the electric fields, the cells can be encased in microdroplets[191]. A similar method is used in the FACS (fluorescent activated cell sorting)[192]. DEP droplet sorting methods have achieved throughputs up to 30,000 cells/s[193].

1.4.9 Optical methods

Light in the form of lasers and the radiation forces produced by them can be used to manipulate cells. Optical cell manipulation has been studied since the 1970s[194] with cell trapping[195], optical tweezing[196], optoporation[197], optogenetics[198] and optical stretching[199] highlighting that focused laser beams can enact forces upon the cells. There are two main forces at play, the lateral force and the axial force. The former occurs when light enters the cell and is refracted, like in a lens, due to the refractive index difference between the cell and the surrounding liquid [200]; resulting in the light to exit in a different direction than before, causing a change in the momentum of the light particle. As the total momentum of the system is conserved, there will be an equal and opposite momentum change, and therefore force, applied to the cell. If the cell is not in the centre of the beam there will be a larger momentum change towards the beam focus, this is the axial force[201]. These forces are illustrated in **Figure 1.11a** and can be used to move cells into specific outlets within a microfluidic device [202]. Optical tweezers can be used to move individual cells but this method has a restricted throughput, even with multiple tweezers employed at once, rates of only 5 cells/s were recorded[203]. An example of a

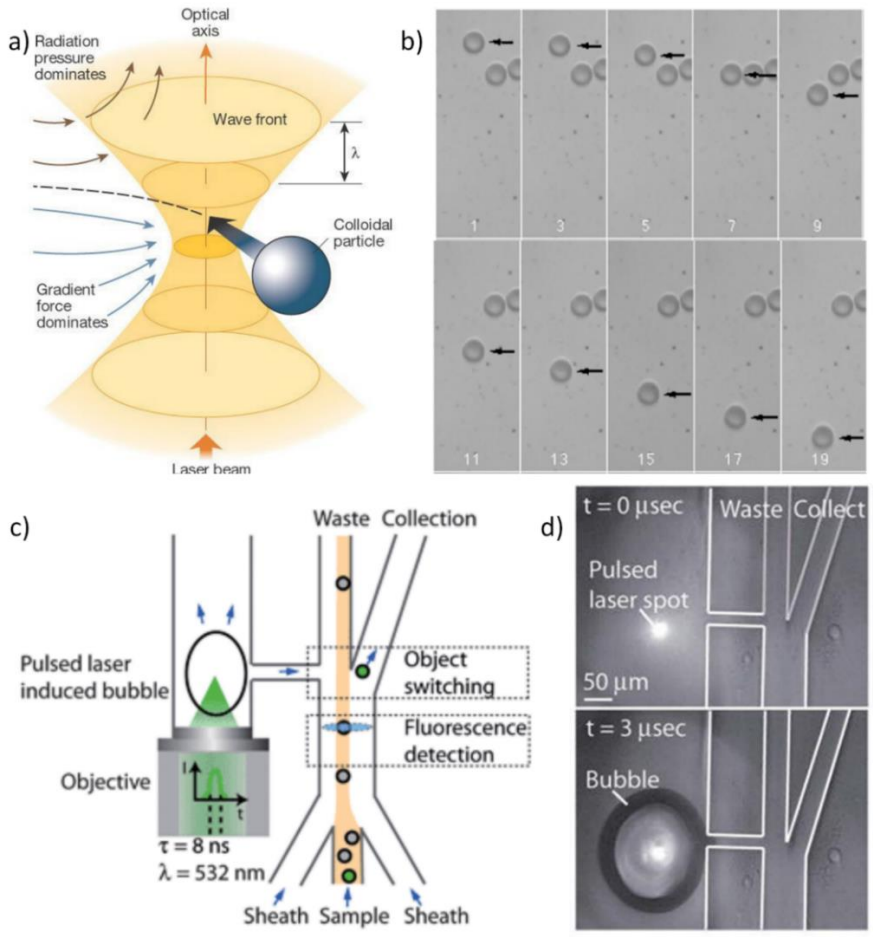

Figure 1.11 (a) *Converging laser beam profile illustrating that particles are drawn to the focus due to the axial gradient force. This allows cells and other small particles to be trapped and maneuvered.* **(b)** *A series of images showing the manipulation of a single 10 µm particle using an optical trap.* **(c)** *Schematic of a pulsed laser activated cell sorter. The sample flow is focused into the centre of the channel and into the waste outlet. If a target cell is detected a laser pulse induces cavitation, resulting in a bubble being produced in the adjacent channel. This displaces liquid and alters the cell path into the collection outlet.* **(d)** *Images of cavitation bubble generation due to a focused laser beam pulse. Figure (**a**) is reprinted from, Nature 424, Grier, et al, "A revolution in optical manipulation", 810, Copyright (2003) Springer-Nature, with permission from Springer Nature*[204]*. Figure (**b**) is Reprinted from Optics Express, 12, Applegate, et al, "Optical trapping, manipulation, and sorting of cells and colloids in microfluidic systems with diode laser bars", 2004 © The Optical Society*[205]*. (**c-d**) are reprinted from, Lab on a Chip 12,Wu, et al, "Pulsed laser triggered high speed microfluidic fluorescence activated cell sorter.", 1378, Copyright (2012) Royal Society of Chemistry, with permission from the Royal Society of Chemistry*[206]*.*

cell being moved in a device is shown in **Figure 1.11b**. Lasers can also act as optical switches which can be switched on and off very quickly, and because the forces from the light can be transmitted at the speed of light, they have been investigated widely as a switching mechanism for high-throughput cell manipulation.

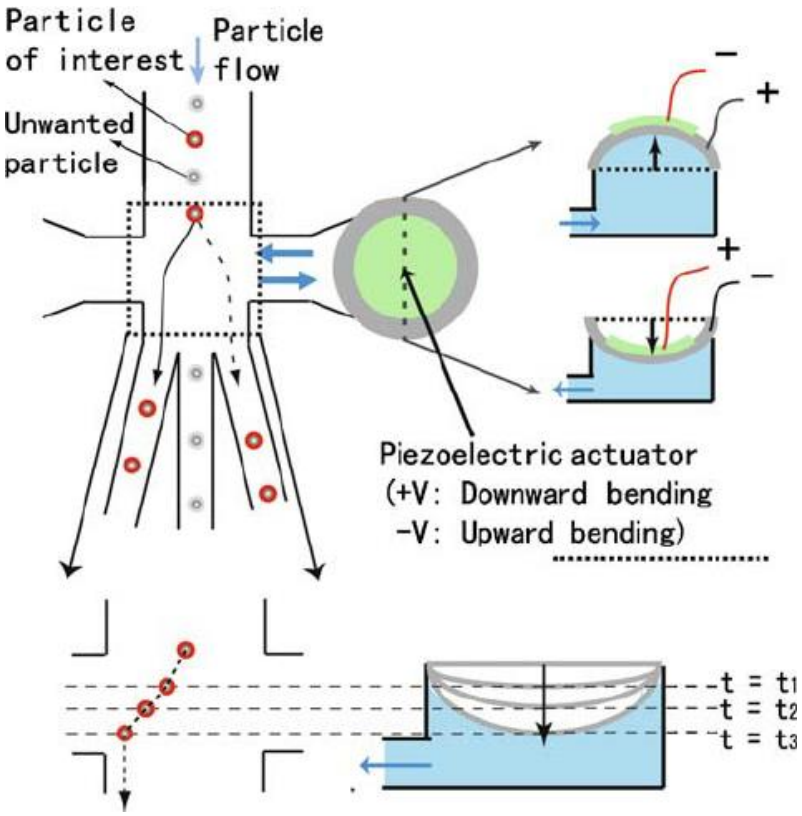

Figure 1.12 *Schematic of piezo sorting mechanism. In this design particles are focused into the centre of the microfludic device and flow into the middle waste channel. By actuating the piezo with either a postive or negative voltage, it will either bend downward or upwards respectively. This causes the liquid within the resevior to displace, causing the particles to be moved to the left or right of the channel and into one of the two sorting outlet channels. This figure is reprinted by permission from Springer Nature: Biomedical Microdevices, "Microfluidic cell sorter with integrated piezoelectric actuator", Chen, et al, (2009)* [36].

If the laser is turned on as a target cells flows by in a microfluidic channel, the cell will experience an additional optical force which can deflect it within the flow of the device and result in it moving into the required outlet channel[205]. This method does not require the cell to be fully trapped and it only needs a small additional force to change the cell direction. Using this method, throughput rates of 100 cells/s have been recorded[207].

Another technique which uses optical switching, focuses intense laser beams into the channel, which can produce temporary vapour bubbles within the liquid (**Figure 1.11c** and **Figure 1.11d**). This technique, called pulsed laser activated cell sorting (PLACS), can be used to generate a low pressure bubble, cavitation, within a microfluidic which eventually collapses due to the higher pressure of the surrounding liquid[208]. The generation of the bubbles displaces liquid in the channel, creating a jet of solution to move flowing cells from one side of the microfluidic channel to the other and into the sorting

channel [206]. This method has been improved with multilayer 3D sheath focusing[209] and has achieved flow rates of up to 45,000 cells/s[210].

1.4.10 Microelectromechanical sorting (MEMS)

Another method in cell sorting uses micro-electro-mechanical sorting (MEMS) devices to manipulate the paths taken by cells within microfluidic devices. Initial devices used switches and valves which opened and closed multiple outlet channels[134]. Depending on the position of the switch the flow focused cells move into the energetically favourable outlet[211]. Valve switching throughputs are limited by the response time of the valves and initially achieved throughputs of hundreds of cells/min[134]. Other methods can be used to bias cell flow into outlets, such as controlling the outlet pressures. If one outlet is at atmospheric pressure while the other is acted upon by a lesser, negative pressure; the cell flow will be directed to the former outlet. These pressures are switched using a hydrodynamic valve, allowing for sorting at throughputs limited to the switching time[212].

Newer MEMS designs employ piezoelectric actuators such as the one seen in **Figure 1.12**. Flow focused cells flow down a main channel and into one of multiple outlets[36]. Perpendicular to the main channel is a channel which leads to a reservoir of liquid with a PZT (lead zirconate titanate) piezo buzzer bonded to the top. This piezo is comprised of a metal plate in contact with a PZT piezoelectric crystal. When an electric current is applied to the buzzer, the PZT expands and contracts causing the metal plates to vibrate. When the piezo is actuated the moving plates displace liquid in the reservoir which flows into the main channel, disrupting the flow of cells. The cells are then pushed into the previously energetically unfavourable outlet[213]. The magnitude and polarity of the voltage affects the magnitude and direction of the piezo bend and so extra channels can be added to sort multiple cell types[214]. A benefit of these devices when compared to the valve based sorting methods is the short reaction time of the piezo. Piezos can actuate in a tenth of a millisecond, leading to high sorting speeds of tens of thousands of events per second[213]. Fluorescence based FACS sorting has been carried out on piezo based devices, with cell sorting being performed in the kilohertz regime[215]. The 2D design employed thus far contains a large cell flow area, with cells having the potential to flow anywhere in the z axis. By focusing cell flow in the z axis, the sorting area is reduced allowing for improved flow control and higher throughputs of up to 10kHz[216].

1.5 Fluorescent labelling

As is evident from the previously described techniques, the cell sized channels within microfluidic devices are an ideal environment to manipulate single cells. These attributes make it possible to isolate and sort individual cells based on their individual properties. The passive methods highlight the ability to sort cells based on attributes such as size, density and elasticity but even cells of the same size and cell type can be heterogeneous. Cells can contain different internal characteristics such as; different volumes of DNA, have different proteins present and express varying numbers and types of surface markers. By targeting these characteristics with a label these differences can be observed and quantified, allowing cells to be further sorted into new subpopulations. This can be done using fluorescent labels: labels which fluoresce under specific conditions. The fluorescent labels which bind to the target protein or surface marker are excited using a light source, such as a light emitting diode (LED) or laser. They then emit light of a higher wavelength; which can be detected, confirming the presence and quantity of the target substance within the cell. More cell characteristics can therefore be detected, allowing for more cell types to be sorted and analysed. Multiple fluorescent markers can also be used at once to further increase the potential number of subpopulations. There are different families of fluorescent surface markers which are discussed below.

1.5.1 Fluorescent proteins

Fluorophores are fluorescent markers which absorb a specific wavelength of light and re-emit light at a different wavelength. Energy is lost in this process and so the emission wavelength is always longer than the absorption wavelength. The fluorescent nature of fluorophores has been known for over a century[217], with JFW Herschel observing molecules in tonic water fluorescing under UV light, but it took another 100 years for these molecules to be used within cells. The family of fluorescent proteins, such as the green fluorescent protein (GFP) found in jellyfish[218], have been critical in the development of fluorescent labelling. GFP has been extracted, synthesized and has been used to tag target proteins within cells since 1992[219]. The genetic code of the cell is altered by fusing new DNA, with encodes of GFP, to the protein of interest. This is incorporated within the genome and results in some of the protein within the cell being fluorescently labelled, causing it to fluoresce when illuminated allowing it to be observed and tracked within living cells[220,221]. To allow for multiple target proteins to be observed

at once, various fluorescent proteins have been developed which absorb and emit varying wavelengths[218].

1.5.2 Fluorophores

More complicated fluorophores have been synthesized to target the cell membrane, cytoskeleton and surface markers[222]. Lipophilic dyes[223] and fluorescently labelled lectins[224] (carbohydrate binding proteins), are used to target the cell membrane and cytoskeleton respectively. To target surface markers, fluorescent molecules are tagged to specific antibodies which bind to particular antigens within the cell[225]. All of these options allow for a wider range of immunophenotyping, improving the study of cell protein expression within cells. If these phenotypes can be observed, the cells can be targeted and sorted using fluorescent activated cell sorting (FACS).

1.5.3 Fluorescent nucleic acid dyes

Another group of fluorescent markers are fluorescent nucleic acid dyes[226]. These dyes do not require gene editing and some are cell permeable so can be easily added to living or dead cells. The dyes bind to grooves found in DNA between the strands[227]. Examples of these dyes are Hoechst and 4′,6-diamidino-2-phenylindole (DAPI) stains. These dyes are excited by ultraviolet light and emit blue light. As DNA is mostly found in the cell nucleus, the dye allows cell nuclei to be stained and observed. Hoechst dye is used in **Chapter 5** and is important in observing cell nuclear morphologies.

1.6 Fluorescent activated cell sorting (FACS)

To sort cells based on the fluorescent signal present, due to their fluorescent label, cells can be sorted using FACS. The cells flow in the FACS sorter and are illuminated with a number lasers, of varying wavelengths, which excites the fluorophores within the cells and the light emitted from them is picked up by a detector[228]. The wavelengths present and the magnitudes of these wavelengths adduce the fluorophores present and their concentration within the cell. The incident light is also scattered by the cell. Forward scatter, which propagates in the direction of the light path; and side scatter, which is deflected perpendicular to the light path can be measured. Forward scatter can be used to determine the cell size with larger cells producing a larger forward scatter signal[229]. Side scatter provides information about the internal structure of the cell[230].

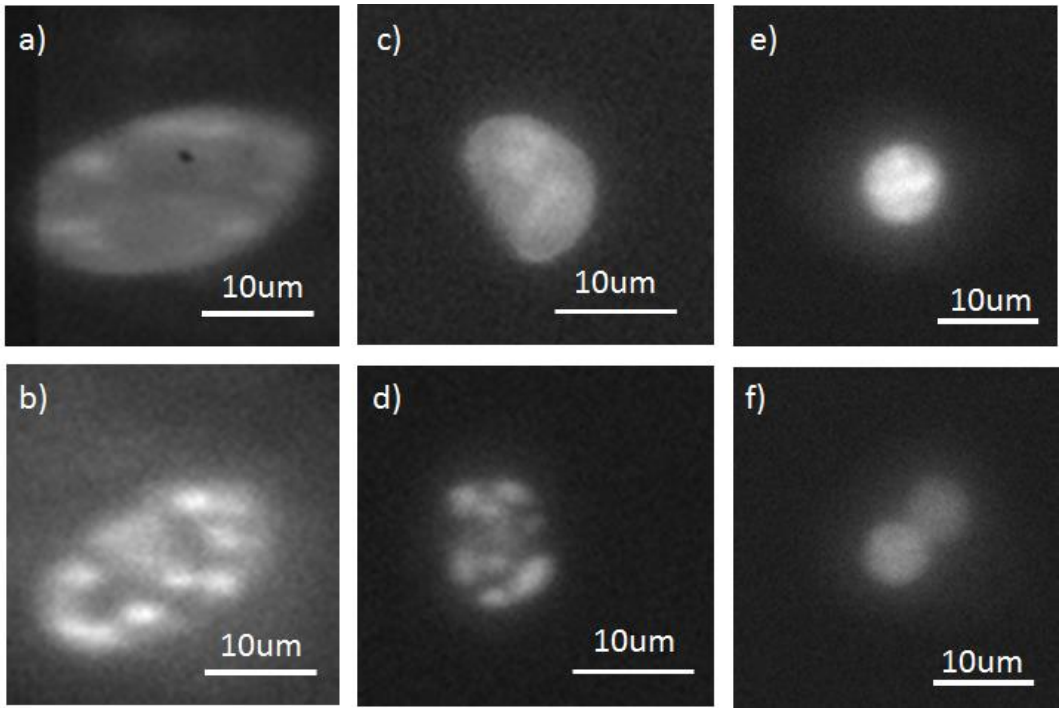

Figure 1.13 *Images taken of cells with stained nuclei within a microfluidic device.* **(a-b)** *Images of SAHF negative and SAHF positive nuclei. The SAHF+ cell contains spotty nuclei while the SAHF negative cell has a more evenly distrubuted nucleus.* **(c-d)** *images of a healthy K562 cell nucleus and an apoptotic K562 cell. The healthy cell nucleus is in tact while the dying apoptotic cell has packaged its nucleus into smaller discrete regions.* ***(e-f)*** *Mononucleated and binucleated hepatocyte cells. The number of nuclei within the cells can be observeed.*

Cells with a more complex internal structure produce a larger side scatter signal[231,232]. Using these three parameters, heterogeneous cell samples can be categorised into more homogeneous subpopulations[233]. After a decision on cell type has been made, charges are added into the fluid surrounding the cell. This fluid pinches off generating a droplet which is then sorted via two charged plates. The cells are sorted into populations depending on the charge applied, which in turn depends on the signals measured by the detectors[130]. This method is able to sort 100,000s of cells a second but due to the expense of the machines and running costs this sorting method is one of the most expensive[234,235].

1.7 Cell models used

As previously described, there are a number of morphological differences that cannot be picked up by standard FACS techniques. Below several cell types with nuclear morphological differences are discussed. The total DNA remains constant but the structure and location of the DNA varies. This means sorting using fluorescent imaging

is vital in separating the cells into groups of similar subpopulations. The following section discusses the cell models used in **Chapter 5**.

1.7.1 Senescence associated heterochromatic foci (SAHF) cells

Although aging is a mostly universal occurrence in both organisms and their individual cells, its exact causes are unclear[236,237]. Most cells can only divide a finite number of times, after which they become senescent[238]. The activation of certain oncogenes can also cause senescence, this is called oncogene induced senescence or OIS. In some of the senescent cells, their nuclei contain senescence associated heterochromatic foci (SAHF)[239,240].

This effect causes the normally smooth cell nucleus, as shown in **Figure 1.13a,** to appear 'spotty', as shown in **Figure 1.13b**. By staining the nucleus and sorting the cells into 'spotty' and 'smooth' nuclei populations, the effects on the cell caused by senescence can be investigated. Once the cells have been separated the active genes within the cells on both populations can be analysed to further investigate the causes and effects of aging. FACS would be unable to sort these cells due to the cells containing the same concentration of DNA and hence providing the same signal.

1.7.2 Apoptosis

At the end of a cell's life cycle it will undergo programmed cell death, or apoptosis[241]. The cell loses is functionality and will start to disassemble. The cell membrane starts to bleb and the cell will eventually break into multiple vesicles which will be engulfed by other cells by phagocytosis. Before the destruction of the cell, the chromatin will condense and the nucleus fragments into smaller discrete units (as seen in **Figure 1.13d**). The total DNA within the cell remains the same, but instead of one large nucleus the cell contains multiple smaller nucleosomal units[242]; which again makes it difficult for a FACS machine to detect and sort, as the intensity of the fluorescing DNA signal would be the same. Apoptosis is an important function in the immune system and the cell life cycle; and can show increased or reduced performance during diseases such as cancer[243]. By isolating apoptotic cells, the genes expressed during these diseases could be further understood.

1.7.3 4n Liver hepatocytes

Polyploidisation is common in hepatocyte liver cells; this involves a numerical change in the number of chromosomes present within a cell. Human cells usually contain 23 pairs of chromosomes, giving a total of 46. The number of chromosomes can be described by the haploid number, n, which, under normal conditions, is half the number of chromosomes found in a non-reproductive cell (23). It has been shown that an important step in liver polyploidisation is the creation of cells containing multiple nuclei and increased haploid numbers, for example 4n, 8n and 16n. The generation of these binucleated cells is due to errors in cell division, or specifically cytokinesis[244]. High polyploidy has been linked with senescence and a decrease in the ability of cell replication[245,246]. With liver disease being higher in Scotland than other European countries, research into liver regeneration is important[247]. If the simplest case of polyploidisation is considered, the cells may contain a single 4n nuclei (**Figure 1.13e**) or two 2n nuclei (**Figure 1.13f**). In both cases the cells contain the same total amount of DNA, it is only packaged differently. In FACS detection, the stained nuclei would give the same fluorescent signal in both cases. By imaging the cells and isolating mononucleated and binucleated cells it is hoped that the reasons behind the induced polyploidy and the link to cell replication can be understood.

1.8 State of the art: Image-based cell sorting

Fluorophores allow a wide range of heterogeneous cell properties to be investigated, but there are still a number of morphological cell differences that cannot be expressed by these parameters such as the distribution of proteins, organelles and other target features. The concentrations of these features may be similar and so when stained the total fluorescent signal would be comparable, but the compounds may be distributed throughout the cell differently[248]. Examples of this can be found in the section above, where various cell types with the same total DNA, package it in different ways, leading to distinct cell functions. The ability to separate these cell types would allow the investigation of the genes used in the varying cell functions. The differences can be seen visually but are not picked up by the quantitative measuring FACS system and so to categorise the cells into homogeneous subpopulations they must first be imaged and classified. Imaging flow cytometry has been carried out at high throughputs, tens of thousands of cells/s[249], but until recently the cells were imaged without being sorted. Multiple sources have suggested that the next stage in cell sorting is the ability to

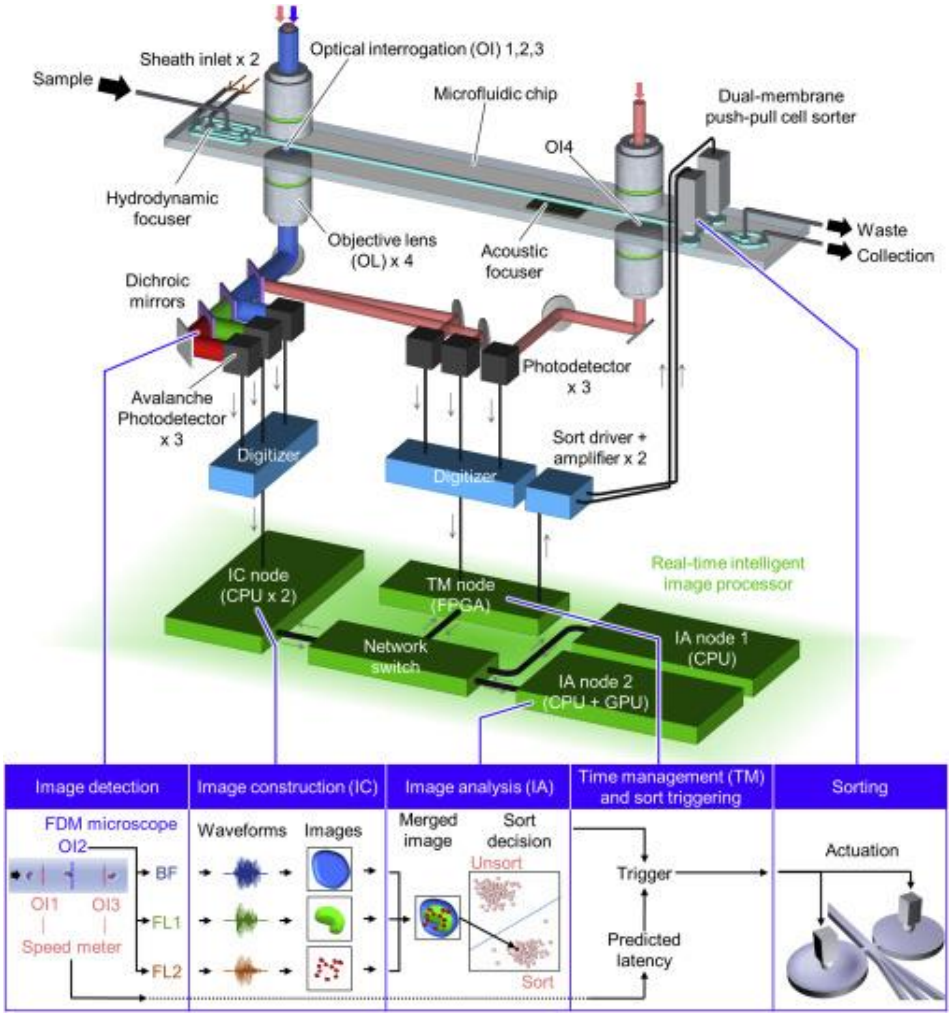

Figure 1.14 *Schematic of Intelligent Image-Activated Cell Sorter (IACS). Cells are focused into the centre of the channel using conventional hydrodynamic methods and are imaged in multiple wavelengths. The data obtained is in waveform format and is then converted into an image of the cell. Deep learning image analysis is then performed on the image to determine if the cell is of interest. If a target cell is present a trigger signal actuates the two piezos to push or pull the cell into the correct outlet. This image reprinted from, Cell 175, Nitta, et al, "Intelligent Image-Activated Cell Sorting", 266., Copyright (2018), with permission from Elsevier*[35].

image, characterise and sort cells in flow; but due to slow image processing and decision making it has been difficult to create a system which can image, categorise and sort cells in real time[250,251]. However, in 2017 the first microfluidic image based cell sorter was developed. The system sorted two types of single cell plankton, a circular and an elongated species. To differentiate between the two cell types an algorithm was used to locate the cells within microdroplets and to determine the shape of the cell. It used electrodes to sort droplets containing the imaged cells at 10 Hz[252].

Improvements were made to the image based sorting technique in 2018 with the intelligent image-activated cell sorting (IACS) technique, shown in **Figure 1.14**[35]. It used piezoelectric actuators to sort the cells and deep machine learning to analyse and

characterise cell images into the relevant subpopulations. A frequency-division multiplexing (FDM) microscope is used to image the cells in both bright field and two fluorescent frequencies. The FDM data obtained by the photodetectors is acquired as waveforms and must be constructed into an image of the cell or regions of the cell[253]. The deep learning algorithm is used to analyse these signals and to categorise each event into one of multiple cell types, by comparing each waveform to pre-trained data sets providing a probability of the present cell being in each class. Thresholds are then used to determine if the cell will be sorted into a particular class or sent to waste. Deep learning allows the data for each new cell to be incorporated into the decision making step of the next cell, and so on, allowing the system to learn and improve with each new image[254]. Throughputs of 100 events per second were recorded with multiple cell types being analysed and sorted[35]. The IACS technique has inspired similar techniques with improvements: Image based cell sorting throughputs have been recorded at 10,000 cells per second[255], the machine learning technique has been used to classify real images rather than the waveform "ghost images"[256] and cells have been imaged in 3D and sorted at throughputs of 500 cells per second. This technique will no doubt evolve over the coming years to become the gold standard in cell sorting.

Chapter 2. Materials and methods

2.1 Microfluidic devices

This section will describe the methods followed to create the microfluidic devices used in **Chapters 3-5**, from the initial design stage to readying the devices for experimental use.

2.1.1 Device design

Adobe Illustrator was used to design the numerous device designs seen throughout the thesis. The designs were then printed onto a high resolution, dark field lithography mask which is used for creating masters.

2.1.2 Master generation

Designs are printed on a high-resolution photomask with negative features (the channels are transparent with the remainder of the mask remaining black and opaque). This is printed by an external company, Micro Lithography Services. Using photolithography these designs can be transferred onto an SU-8 coating on a substrate of silicon wafer, creating a master mould for the devices to be manufactured from.

SU-8 2025 photoresist is poured onto a 3 inch diameter silicon wafer and spread using a pipette tip to cover the whole wafer. The wafer is then placed onto a spin coater. An initial rotation of 500 rpm is used for 10 seconds. The spin coater then accelerates to the desired speed at 300 rpm s^{-1}. Once the desired speed has been reached, the coater will spin for a further 30 seconds. The rotation spreads the SU-8 2025 to the desired thickness and the speeds used can be found in **Table 2.1**, which is based on the manufacturers specifications. The wafer is removed from the spin coater and the SU8 is soft baked to remove any solvent from the material and to create a solid coating of photoresist. To achieve this the wafer is placed on a hot plate at 65°C, followed by a hot plate at 95°C and finally back to the hot plate at 65°C for the times listed in **Table 2.1**. While on the hot plate, a tin foil covered petri dish lid is placed over the wafer to prevent stray, ambient UV light from cross linking the SU-8 on the wafer. Once the soft bake is complete, the wafer must be exposed to a controlled intensity of UV light to cross link the photoresist and create the required features for the mould. The desired designs are cut from the photomask and placed onto silicon wafer. The remainder of the wafer is covered by plain black photomask to shield it from UV exposure. This allows the same design to be

exposed multiple times on the same wafer so long as the exposures do not overlap. A glass disk is placed over the photomask covered wafer to prevent bends in the mask, which may allow the UV light to crosslink the wrong areas of the wafer. A Thorlabs, 190 mW, 365nm LED (M365L2) is placed over the glass disk, covering the whole wafer and is turned on at full power for 42 seconds, this was found to be the optimum exposure time after a trial and error experiment. The wafer is moved back onto the two hot plates for a post-exposure bake, again the times can be found in **Table 2.1**.

Once this step is complete the designs should be visible on the wafer. The uncross-linked SU-8 must now be removed using a developer (propylene glycol monomethyl ether acetate). A small sonicator is filled with water and a pipette tip box is placed inside. This allows a small glass beaker to be placed on top without being fully immersed. The developer is poured into the beaker until it is about 2cm from the bottom. The wafer is then placed inside the beaker. The sonicator is turned on initially for 15 seconds. The wafer is then removed and isopropanol is sprayed onto the silicon wafer, removing the excess SU-8. An air gun is then used to dry the wafer. This step is repeated for a sonication time of 10 seconds, followed by one of 5 seconds. Further sonications can be performed in 5 second steps to remove any uncross-linked SU-8. The process is

Wanted height (µm)	Spin speed (rpm)	Soft bake time at 65°C and 95°C (mins)	Exposure time at 190 mW (s)	Post exposure bake time at 65°C and 95°C (mins)
20	4000	3, 6	42	1, 5
30	3000	3, 6	42	1, 5
40	2500	3, 6	42	1, 5
50	1750	3, 9	42	2, 7
60	1500	3, 9	42	2, 7

Table 2.1 *Settings and timings for device master creation*

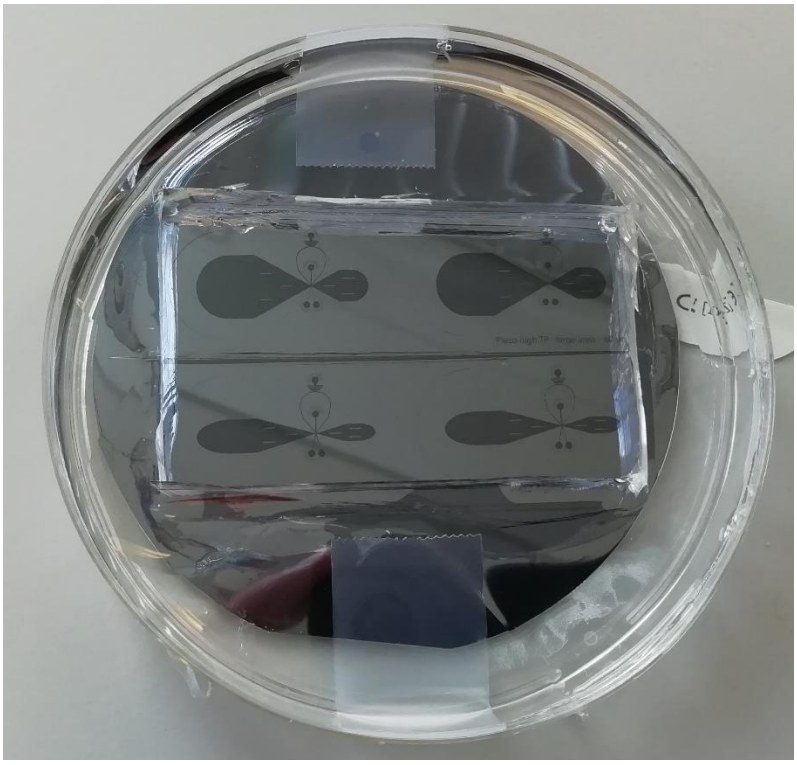

Figure 2.1 *Image of master used to create cell sorting devices.*

complete once the wafer is clean and contains no "sandy" looking regions outwith the cross-linked designs. The master is then placed into a petri dish. The master must now be hydrophobically coated to allow for easier removal of the eventual PDMS layer. Two 1 μL droplets of silane (Trichloro 1H,1H,2H,2H petrafluoro octyl) are placed into the petri dish on the plastic surrounding the master and the dish is covered and left in a fume hood for an hour. This allows the silane to evaporate and coat the master. The remaining silane can be removed using a tissue. The master is now ready to make devices and an example can be found in **Figure 2.1**. The masters used to create the devices in **Chapter 4** and **Chapter 5** were generated using this method. However, the droplet devices used in **Chapter 3** were created using masters provided by Clive Smith of Sphere Fluidics Limited.

2.1.3 PDMS device creation

Polydimethylsiloxane (PDMS) devices are widely used in the field of microfluidics. The material is itself inert, transparent, cheap and compatible with biological samples. It can therefore be used as a microscopic reaction chamber for both chemicals and cells. The PDMS used was SYLGARD 184. This comes in two parts; the PDMS elastomer and the curing agent. The two liquids are mixed into a plastic cup at a ratio of 10:1 (elastomer : curing agent), but this mixing creates air bubbles in the system, which need to be removed. The mixture is placed into a vacuum chamber, causing the air to rise to the top of the cup and escape the mixture. Once the mixture is bubble free it is poured into the petri dish containing the master. Again, this will create unwanted bubbles which need to be removed. The dish is placed into the vacuum chamber until the air has dissipated out of the PDMS. The dish is then placed into an oven for at least two hours at 70 °C, after which the PDMS will have hardened.

Using a scalpel blade the devices are cut out of the master and are placed on a cutting mat, where inlet and outlet holes and piezo reservoirs are punched using a 1 mm biopsy punch respectively.

The devices must then be adhered onto a base (either a glass slide or cover slip) to seal them, creating a semi-enclosed environment, only open through the inlets and outlets. For the microdroplet devices, a glass slide is used. When fluorescent cells are involved (in **Chapters 4 and 5**) a glass cover slip is used to allow the microscope objective to be closer to the cells.

The PDMS devices and base are placed into a plasma treatment system (Diener Zepto). This system removes the hydrocarbon groups on the surfaces of the materials allowing covalent bonds between the device and base. The power and time of the system is set to 100 W and 54 s respectively and a vacuum pump reduces the pressure to below 0.4 mBar. The pressure is then adjusted to 0.6 mBar and the plasma is turned on. Once 54 s have passed the plasma turns off and the pressure is allowed to return to atmospheric pressure. The devices are then pressed firmly face down onto the bases, allowing the strong covalent bonds to occur. The devices are placed back in the 70°C oven for an hour; this was found to reduce detachment. After this step they are ready to use.

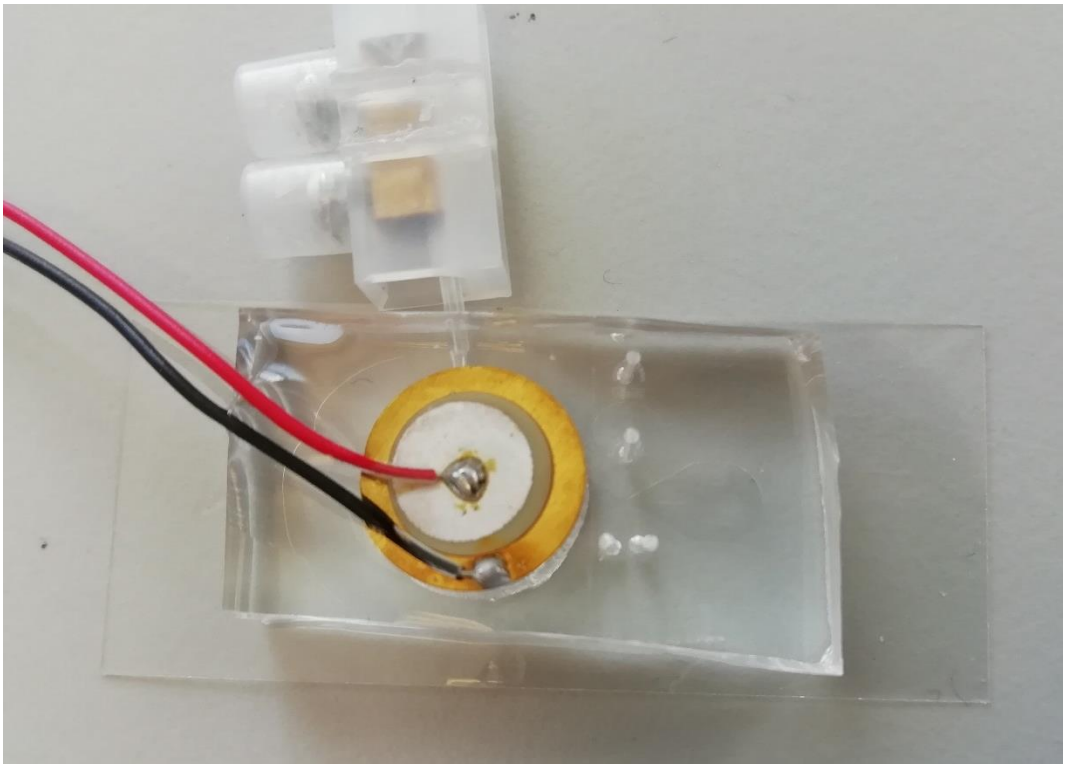

Figure 2.2 *Image of cell sorting device. The piezo, along with the two inlets, two outlets and the tubing closed off with the screw terminal can be seen.*

2.1.4 Piezo sorting devices

The piezo sorting devices have additional fabrication steps to incorporate the piezo element. A 6 mm hole is created using a 6 mm biopsy punch and a 6 mm piezo is placed into this hole as seen in **Figure 2.2**. A 1 mm hole is then inserted into the side of this 6 mm reservoir, again using a biopsy punch. The hole must be below the piezo. Tape is used to temporarily cover the inlets and outlets of the device. PDMS is then poured into the exposed, 6 mm hole, reservoir and onto the piezo to seal the final hole. The devices are placed into the oven, as before, for at least two hours. The tape can then be removed from the top of the device revealing free inlets and outlets. The PDMS device can then be bonded to a glass cover slip as described in the previous section.

2.1.5 Device coating

In **Chapter 3** water droplets are surrounded by fluorous Novek 7500 oil, which is in contact with the device walls and the glass that the device is bonded to. PDMS and glass are naturally hydrophobic materials but surface wetting can still occur, rendering an experiment compromised. To allow for a successful experiment, devices must be fluorophilic, like the oil. To achieve this the devices are coated with a fluorous oil with 1% silane. The solution is injected into the device inlet using a 1 mL syringe until there is no air left in the device. Tape is then placed over the inlets and outlets to prevent evaporation. The device is left for 10 minutes, in which time the silane coats the channels. The tape is then detached and the solution is then removed from the channels by injecting air into the device via a syringe. The device is then cleaned using syringes of air and oil by first injecting oil into the device and then removing it with air. This step is repeated twice. The device is then ready to use.

2.2 Microdroplet techniques

This section describes the techniques employed to use the droplet devices (described in **Section 2.1**) to generate, measure and control microdroplet generation and their contents.

2.2.1 Device preparation and setup

Solutions of fluorous oil (2% PicoSurf, Sphere Fluidics in Novec 7500) and deionised water are delivered to the devices using silicon tubing (with an outer diameter of 1 mm). This tubing is connected to either the syringes with 22 gauge needles, or pressurised reservoirs (Elveflow). If the syringes are used, they are mounted on the corresponding stepper-based syringe pump (KD Scientific) or a pulseless syringe pump (Cetoni neMESYS). In the case of the reservoirs being used, they are attached to a pressure pump (OB1 Elveflow). The outlet of the device is connected by tubing to a vial (2 mL Eppendorf) for collection. An infrared laser used for droplet detection (discussed more in **Section 3.2**) is aligned to the middle of the channel, several hundred microns from the flow-focusing junction and the camera's region of interest is adjusted to the same position, to ensure only fully formed droplets are imaged. The threshold for triggering the camera is adjusted to ensure a single trigger pulse is sent for each droplet. Initial flow rates or pressures are chosen based on previous experiences and are allowed to equilibrate before measurements are taken. Images are acquired using the Vision Acquisition Software module of LabView (National Instruments) and processed in real time using the

Vision Development Module of LabView. Control of the OB1 pressure pumps is achieved using the drivers supplied by the manufacturer, which allows direct control of the desired pressure within LabView. Once the oil and water is injected into the device, droplets form after the flow focusing region.

2.2.2 Droplet volume estimation

The length of the droplet, parallel to the channel, across its centre is measured using a line intensity profile. The NI-IMAQ peak detection tool is implemented to locate the edges of each droplet allowing length, L, to be calculated. This length is used to estimate the droplet volume, $\boldsymbol{V_{measured}}$, using the approximation found in **Section 1.3.9**.

2.2.3 Droplet feedback system

The droplet volume measured, as described above, is averaged over the last 50 droplets to give $\overline{\boldsymbol{V_{measured}}}$ and compared to the wanted value, $\boldsymbol{V_{wanted}}$. The error, $\boldsymbol{\sigma_V = \overline{V_{measured}} - V_{wanted}}$, *i*s used to modulate the pressure pumps.

Droplet volume measurements are integrated over a timescale of 0.1 s to reduce the effects of outliers. The change in pressure, Δ, is governed by the feedback equation[257]:

$$\Delta = \boldsymbol{K_p^V \sigma_V + K_i^V \int \sigma_V \, dt + K_d^V \frac{d}{dt} \sigma_V} \qquad \textbf{(2.1)}$$

Where $\boldsymbol{K_p^V}$, $\boldsymbol{K_i^V}$ and $\boldsymbol{K_d^V}$ are the proportional, integral and derivative constants respectively, which describe the behaviour of the feedback. The value of $\boldsymbol{K_p^V}$ reacts proportionally to any change in the error, reducing the rise time of any steady state errors. $\boldsymbol{K_i^V}$ reacts to and reduces long term, steady state errors, while $\boldsymbol{K_d^V}$ is based on the rate of change of the error and reduces overshoots in the response of the feedback[258]. In this work $\boldsymbol{K_p^V}$ was found to be the dominant term and optimised as described in the main text. Therefore an error, $\boldsymbol{\sigma}$, would result in a pressure change of $\boldsymbol{\Delta = K_p^V \sigma_V}$ and so $\boldsymbol{P_{n+1} = P_n + \Delta}$ where $\boldsymbol{P_n}$ is the initial pressure provided by the pressure pump and $\boldsymbol{P_{n+1}}$ is the new updated pressure.

2.2.4 Cell encapsulation

Red blood cell samples are prepared by diluting 10 μL of whole blood (obtained by finger prick from healthy volunteers in accordance with Heriot-Watt University ethical guidelines with informed consent) into 1 mL of buffer solution consisting of either 28% OptiPrep solution in PBS ("Density Matched" buffer) or 10% OptiPrep in PBS ("Non Density Matched" buffer). The 28% OptiPrep solution is produced to have a density of 1.09 g/mL to match that of RBCs, 1.09–1.10 g/mL. Samples are then loaded into either a syringe or vial, to be injected into the device.

2.2.5 Droplet cell concentration feedback system

The cell concentration feedback loop uses two parameters, $\boldsymbol{P_n^T}$, representing the total aqueous pressure, and $\boldsymbol{\alpha_n}$, the ratio of the cells to buffer pressure, where n is the iteration number. Cell concentrations, $\boldsymbol{Conc_{measured}}$ are determined in real-time from image analysis of camera images by background subtraction, thresholding and binary particle analysis using the Vision Development Module (National Instruments). The feedback loop calculates the new errors and new values as:

$$\boldsymbol{\sigma_V = \overline{V_{measured}} - V_{wanted}} \quad \textbf{(2.2)}$$

$$\boldsymbol{\sigma_C = \overline{Conc_{measured}} - Conc_{wanted}} \quad \textbf{(2.3)}$$

$$\boldsymbol{P_{n+1}^T = P_n^T + K_P^V \sigma_V} \quad \textbf{(2.4)}$$

$$\boldsymbol{\alpha_{n+1} = \alpha_n + K_P^\alpha \sigma_C} \quad \textbf{(2.5)}$$

$$\boldsymbol{P_{cells} = P_{n+1}^T \cdot \alpha_{n+1}} \quad \textbf{(2.6)}$$

$$\boldsymbol{P_{buffer} = P_{n+1}^T \cdot (1 - \alpha_{n+1})} \quad \textbf{(2.7)}$$

where $\boldsymbol{\sigma_V, \sigma_C}$ are the errors in the volume and concentration, $\boldsymbol{K_P^V, K_P^C}$ are the proportional feedback constants for the volume and concentration respectively and $\boldsymbol{P_{cells}, P_{buffer}}$ are the pressures applied to the cells inlet and buffer inlet respectively.

2.3 Cell sorting techniques

This section discusses the preparation of both K562 cells and Jurkat cells. Live senescent fibroblasts (described in **Section 1.7.1**) and binucleated hepatocytes (described in **Section 1.7.3**) were provided by Nattaphong Rattanavirotkul (University of Edinburgh) and Jordan Portman (University of Edinburgh) respectively. They were used within the devices without further preparation. The use of the piezo device and the generation of receiver operating characteristic curves is also discussed.

2.3.1 Cell culture for K562 cells

Media used for culturing K562 cells:

- 500 mL RPMI 1640
- 50 mL Foetal Bovine Serum (FBS)
- 5 mL Pen/Strep
- 5 mL Glutamax

The K562 cells are passaged three times a week. The cells are in suspension and so the concentration is calculated as described in **Section 2.3.3**. The cell solution is pipetted into a falcon tube and spun down for 5 mins at 1800 rpm. The excess solution is removed, leaving a pellet of cells containing roughly 10 million cells. 5 mL of media is added to the falcon tube and the solution mixed to distribute the cells evenly. This is then added to a 75 cm^3 flask, containing 15 mL of media, bringing the total volume to 20 mL and the cell concentration to 0.5 million cells per mL. This value is calculated using the initial counted concentration. For example, for a count of 1 million cells per mL, 10 mL of solution would be spun down and the pellet added to 20 mL of media to give a concentration of 0.5 million cells per mL. The flask is stored in an incubator at 37°C and 5% CO_2.

2.3.2 Cell culture for Jurkat cells

Media used for culturing Jurkat cells:

- 500 mL RPMI 1640
- 50 mL Foetal Bovine Serum (FBS)
- 5 mL Pen/Strep
- 5 mL Glutamax

The Jurkat cells are passaged roughly three times a week. These cells are adherent and so the confluence of the cells (how much of the bottom of the flask is covered by the cells) is judged by eye and the cells are split once they reached 90% confluence. To detach the cells from the bottom of the flask, the flask is gently tapped with one hand, as the other hand holds the flask. 10 mL of the cell solution is pipetted into a falcon tube and spun down for 5 mins at 1800 rpm. The excess solution is removed, leaving a pellet of cells containing roughly 8 million cells. 5 mL of media is added to the falcon tube and the solution mixed to distribute the cells evenly. This is then added to a 75 cm^3 flask, containing 15 mL of media, bringing the total volume to 20 mL and the cell concentration to 0.4 million cells per mL. The flask is stored in an incubator at 37°C and 5% CO_2.

2.3.3 Cell counting

It is important to know the concentration of cells within media before passaging them. To count the number of cells per millilitre a Neubauer haemocytometer is used. Firstly, the cells in media solution is mixed using a pipette to allow the cells to distribute more evenly throughout the solution. A pipette is then used to collect 20 μL of solution and 10 μL is placed into each side of the haemocytometer. A glass cover slip is placed onto the counting chamber to spread the solution evenly. The counting chamber contains a 1 mm x 1mm grid where the cells are counted. The volume of liquid within this region is $1x10^{-4}$ mL and so the concentration of cells within the solution is 1 million cells for every 100 counted within the chamber.

2.3.4 Defrosting cells

When a new batch of cells are required, a vial is retrieved from the liquid nitrogen storage container. The vial is defrosted quickly within a 37°C bead bath. The contents are placed into a 15 mL falcon tube and topped up with media. The cells are then spun down and resuspended in media to remove unwanted dead cells, the dimethylsulfoxide (DMSO) which will be contained within the solution. If left unremoved the DMSO can have a negative effect on cell viability[259]. The new cell solution is transferred to a 25 cm^2 flask and placed into the incubator. After a week of changing the media, the cell population should be healthy enough to split.

2.3.5 Cryopreservation of cells

The concentration of cell solution is counted using the method described in **Section 2.3.3**. The cells are spun down, for 5 mins at 1800 rpm, into a pellet and resuspended to 5 million cells / mL with FBS and 10% DMSO. 1 mL of solution is aliquotted into 1.8 mL cryo-vials. These vials have to be screw top vials to prevent the tops bursting off at the cold storage temperatures. The vials are placed in a Mr Frosty freezing container and left in a -80 °C freezer for at least 2 hours. The jar cools the solution at a rate of -1 °C per minute. This allows the temperature of the frozen solution to reach -80 °C. The vials can then be removed from the container and transferred into the liquid nitrogen freezer. This is kept at -180 °C.

2.3.6 Staining cell nuclei

The cells are stored in a media solution. To stain the cells, 10 µL of Hoechst 33342 stain, per 1 mL of cell solution, is added. The cells are then incubated for 10 minutes. The solution is spun down for 1 minute at 1800 rpm to create a cell pellet. The remaining solution is then removed and 1 mL of PBS is added to the cell pellet. The solution is then pipetted up and down to dislodge pellet. The solution is spun down once more for 1 minute at 1800 rpm. Finally, the remaining PBS solution is removed, leaving only the pellet. The cell solution of PBS +1% pluronic and Optiprep can then be added to the pellet.

2.3.7 Cell transfection to induce apoptosis

To induce apoptosis in the K562 cells daunorubicin (DNR) is used. DNR is dissolved in water and stored at −20 °C as a 0.95 mM stock. The cells are treated with 1 µM of DNR and incubated at 37°C with 5% CO_2 for 24 hours. The solution is then spun down for 5 minutes at 1800 rpm, creating a cell pellet. This solution is removed and PBS is then added to wash the cells. The solution is spun down once more and the required solution can then be added to the cell pellet to resuspend the cells.

2.3.8 Setting up piezo device

To obtain a stable flow system within the microfluidic device, the channels must be free of air. The large reservoir, where the piezo sits, makes this harder to achieve. A needle is attached to a 1 mL syringe containing PBS, and polytetrafluoroethylene (PTFE) tubing is fed onto this needle. PBS is then slowly injected into the inlet hole in the side

of the reservoir, allowing the liquid to slowly fill the area while letting the air escape through the inlets and outlets at the other side of the device. When the reservoir is nearly full a small air bubble will be present at the top of the device. By rotating the device, the air bubble can be moved to be in contact with the channel. A final release of PBS from the syringe should allow this air bubble to evacuate the reservoir leaving an air free chamber. At this point a screw terminal is used to seal the tubing, preventing PBS from leaking. To remove the remaining air present in the channels, the needleless syringe, filled with PBS, is placed over an outlet and injected into the device. The tubing from the flow focus PBS syringe is then fed into the flow focus inlet. A droplet of PBS must be present at the edge of the tubing to prevent air bubbles entering the device. The tubing from the cell syringe is then fed into the cell inlet of the device. The final two outlets are connected to pressure sealed 1.5 mL vials (Eppendorf) containing 0.5 mL of PBS, via PTFE tubing. A pressure pump is used briefly to allow the PBS to flow out the tubing. The tubing can then be fed into the outlets as no air bubbles will be present. The microfluidic system is now closed from the atmosphere and ready to sort. The running of the device is described in **Section 4.2.2**.

2.3.9 ROC curves – determining characterisation success

Receiver operating characteristic (ROC) curves are used to illustrate the deterministic ability of a two outcome classification system, by showing the change in true and false positives as the classification threshold is altered. To plot the ROC curve the number of true and false positives must be calculated.

An example graph can be seen in **Figure 2.3a**, with the orange and blue curves representing the two classes. The black lines represent the threshold which will sweep across the x-axis; and for each threshold value investigated, the number of images at either side of the line (and the class they belong in) is noted. Images to one side of the line are accepted (as a positive classification) while images to the other side are rejected (as a negative classification) and this is used to calculate the number of true and false positives.

This technique is used in **Chapter 4** to test the classification success of the area threshold. This simple metric used for classification allows a ROC curve to be generated. Manually classified images of RBCs and K562s are classified using a sweeping area threshold, with everything above the threshold being classified as a K562 cell and everything below the threshold being classified as an RBC. The outcome of the classification is analysed to calculate the true and false positive values for each threshold and this is used to plot the ROC curve seen in **Figure 4.9a**.

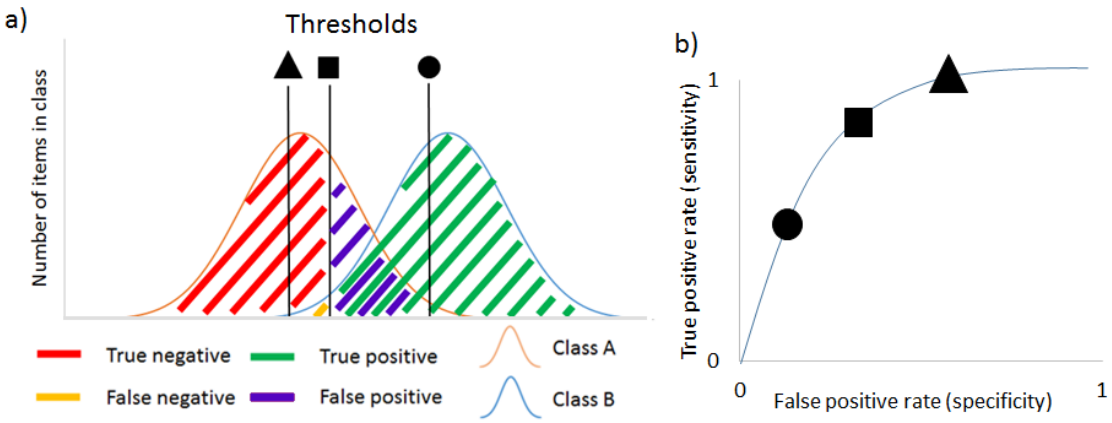

Figure 2.3 (**a**) *Diagram displaying the Gaussian distributions of two classes for a specific measurement value. To generate a ROC curve, a threshold (the black line) is swept across this graph, with the number of true positive values and false positive values to the right of the threshold used to calculate the true and false positive rates. The shapes (rectangle, square and circle) above the threshold lines represent the thresholds used to calculate the representative false positive and true positive points on the adjacent ROC curve graph (**b**).*

The ROC curves generated in **Chapter 5** use 25 measurements of each cell image to create a 'confidence value', which is used as the sweeping threshold. These measurements can be found in **Table 2.2** and the method used to generate the confidence value is discussed more in **Section 5.5**. As he confidence value threshold is not a single measurement, it is more complex; and therefore a value of 0 does not result in all images being classified as class B (as it would be in **Figure 2.3**). We therefore do not get points at the top right of the graph and this again is discussed in **Section 5.5**.

Measurement number	Measurement
1	Area: Area of the particle in pixels
2	Bounding Rectangle width: The width of the bounding rectangle (the smallest rectangle that can contain all pixels of the particle).
3	Bounding Rectangle height: The height of the bounding rectangle.
4	Bounding Rectangle Diagonal: The diagonal length of the bounding rectangle.
5	Perimeter: The perimeter of the particle.
6	Convex hull perimeter: The perimeter smallest convex polygon that can surround all particles (the convex hull).
7	Hole's perimeter: Sum of the perimeters of all holes in the particle.
8	Maximum Feret diameter: Maximum distance between points.
9	Equivalent ellipse major axis: The major axis of the ellipse with the same area as that of the particle.
10	Equivalent ellipse minor axis: The same as above, but the minor axis.
11	Equivalent rectangle long side: The length of the large side of the equivalent rectangle. This is the rectangle with the same area as that of the particle.
12	Equivalent rectangle short side: The same as above but the length of the short side of the rectangle.
13	Average horizontal segment length: A segment is a row of continuous particles. This is the average length of horizontal segments.
14	Average vertical segment length: The same as above but vertical segments.
15	Hydraulic radius: Particle area divided by particle perimeter.
16	Waddel disk diameter: Diameter of the disk with the same area as the particle.
17	Hole's area: Sum of the areas of each hole in the particle.
18	Particles and hole's area: The area of the particle added to the area of all holes in the particle.
19	Convex hull area: The area of the convex hull.
20	Number of holes: Number of holes in the particle.
21	Number of horizontal segments: Continuous rows of pixel are segments. This is the number of horizontal segments.
22	Number of vertical segments: Same as above but vertical.

23	Orientation: The angle of the line that passes through the particle centre of mass about which the particle has the lowest moment of inertia.
24	Compactness factor: Particle area divided by both the bounding rectangle width and height.
25	Heywood circularity factor: Particle perimeter divided by the circumference of a circle with the same area.

Table 2.2 *The 25 measurements calculated for each cell image in* ***Chapter 5***.

Chapter 3. Image-based closed-loop feedback for highly mono-dispersed microdroplet production

This chapter focuses on applying real-time image analysis to address the problem of microdroplet monodispersity described in **Section 1.3.13**. Droplets were imaged in flow and image analysis was performed to calculate the volume of each droplet. If there was a deviation from the target droplet volume, a feedback system was employed to alter the input pressures, which control the droplet volume. Further feedback systems were then added to monitor and control the frequency of droplet production and the number of injected cells per droplet. The latter of the two methods performed real-time image analysis on cells, which is built upon in **Chapter 4**. The work contained within this chapter was published in Scientific Reports and presented at the SelectBio Lab-On-A-Chip and Microfluidics 9th annual conference in Munich. The figures in this chapter and some text is taken from this paper and due to the open access nature of the publication, permission has been granted. The masters used for device generation were provided by Clive Smith (Sphere Fluidics Limited).

Outputs:

- Crawford, D. F., Smith, C. A. & Whyte, G. Image-based closed-loop feedback for highly mono-dispersed microdroplet production. Sci. Rep. 7, 10545 (2017).
- Crawford, D.F., Whyte, G. Highly mono-dispersed microdroplet production using imaged-based closed-loop feedback, Poster session presented at: SelectBio Lab-On-A-Chip and Microfluidics 9th annual conference; 10-11 May 2017; Munich, Germany.
- Heriot Watt IB3 1st year research prize.

3.1 Overview:

The broad range of applications for microdroplets has been described in detail in **Section 1.2**. The ability to successfully perform these experiments is often dependent on the control of both the size and the resulting monodispersity of the microdroplets. The precise size of a microdroplet depends on a wide variety of parameters, including flow rates, device geometry, viscosities and interfacial tensions; so reliably creating droplets of a known size is often an iterative, trial-and-error process. Even when droplets are produced with a known volume, the monodispersity of production can vary depending on the production method used, as described in **Section 1.3.13**.

In this work, the combination of image-based feedback and pressure driven pumping is used to accurately control the size of microdroplets produced in a microfluidic device with high levels of monodispersity. The use of fast-response, pressure-driving pumps allows the microfluidic flow to be quickly and accurately changed. While directly measuring the droplet size allows the user to define the more meaningful parameters of droplet size and generation frequency, rather than flow rates or pressures. The feedback loop enables the drift correction of pressure-based pumps, and leads to an increase in the monodispersity of the droplets produced over long time periods (minutes to hours). By implementing two pressure pumps, changes in pressure, and therefore changes in flow rates, will have a faster response, allowing a closed loop feedback to perform at higher throughputs.

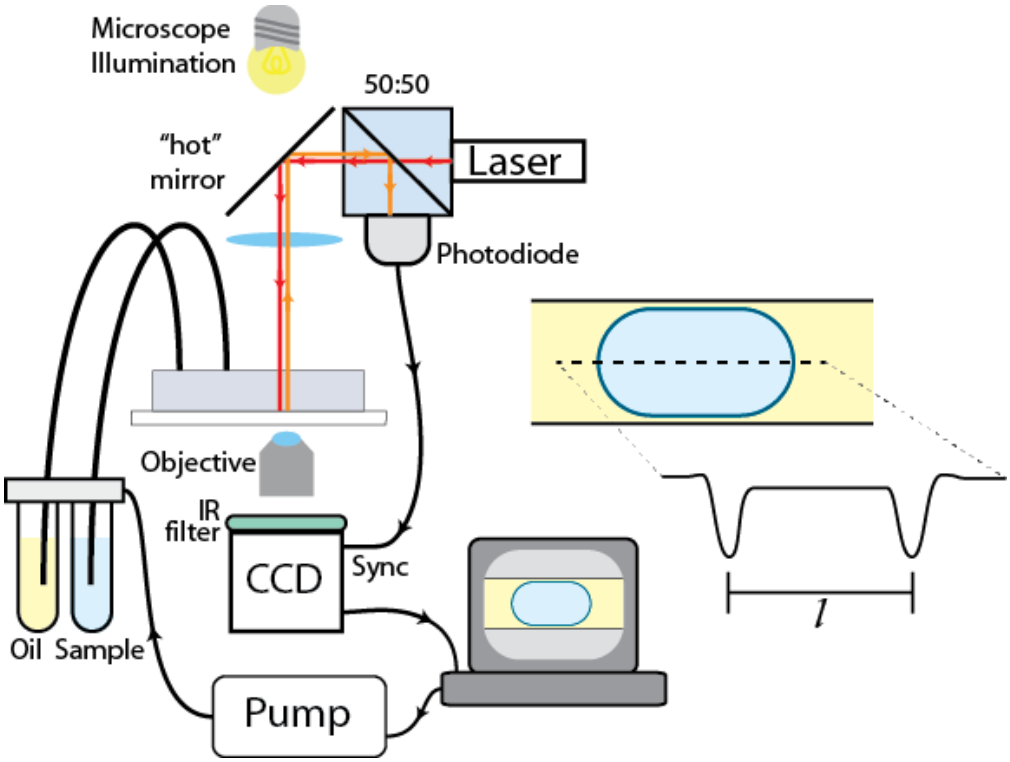

Figure 3.1 *Schematic diagram showing the setup used for image-based feedback. Two immiscible phases (fluorous oil and water) are pumped into a microdevice featuring a flow-focusing section, by pressurised air controlled by bespoke feedback software. Both solutions are contained in separate vials and the pressures within are controlled independently. Image acquisition is synchronised to the presence of a droplet using the backscatter signal from an IR laser. The droplet length can be measured using simple image processing, the volume can be calculated and this information fed back to the control of the pump.*

3.2 Experimental setup

A pair of continuously flowing solutions are used to generate the microdroplets. If the pressure imparted on the vials or the syringe pump flow rates remain constant then it could be argued that the generation method is passive. This approach is preferable, to that of an active one, as it negates the need for complex equipment and the microdroplet size and frequency are dependent on the flow rates of the two immiscible solutions (oil and an aqueous solution), providing the liquid properties and channel geometries remain constant. The PDMS microfluidic device with a flow-focusing junction (**Figure 3.2a** and **Figure 3.2b**) is mounted on a microscope equipped with a high-speed camera, synchronised to droplet formation using an infra-red laser and back-scatter detector, seen in **Figure 3.1**. The device channel height is 55 µm and this was confirmed by cutting a cross section of the channel, as seen in **Figure 3.2c**. This image was compared to an image of a cell-counting chamber, of known dimensions, so an accurate scale could be used. These dimensions are important for droplet volume calculations later on.

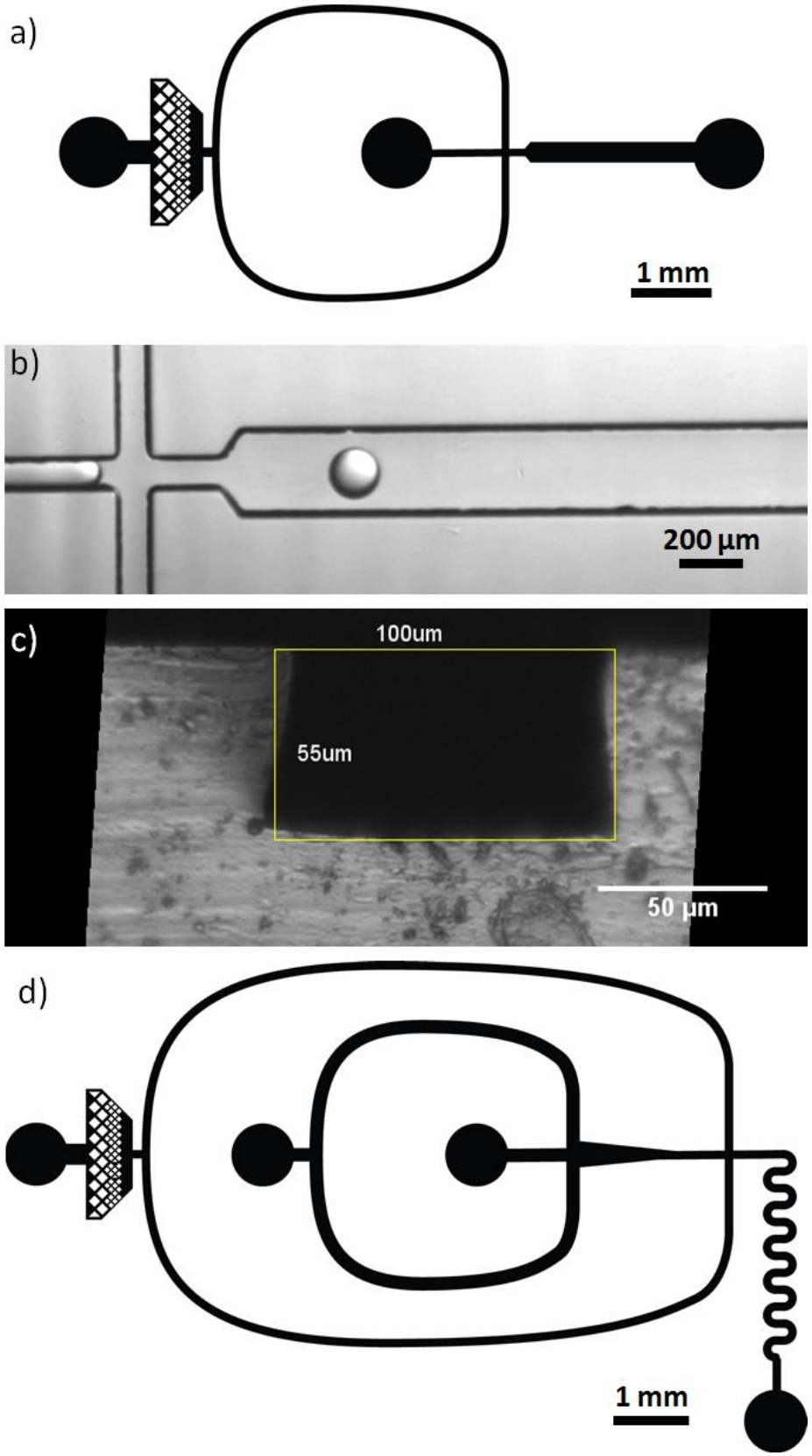

Figure 3.2 (a) *Diagram of the design used for droplet formation.* **(b)** *Image of droplet production at the flow focus junction.* **(c)** *Cross section of a cut PDMS device showing the height and width of the inlet channels of the droplet device.* **(d)** *Diagram of the cell encapsulation droplet device used for later experiments.*

The oil and water are fed into the microfluidic device using either a regulated pressure pump system or syringe pumps, creating microdroplets after the flow focusing junction in the squeezing or dripping regime. The syringe pumps can be set to pump at a constant flow rate, unlike the pressure regulator system, which indirectly controls the inlet flow rates by regulating the pressures at the two inlets, with the flow rate being determined by the applied pressure and the hydrodynamic resistance. This can either be used traditionally or, as described here, modified to include feedback to maintain a constant droplet volume.

The IR laser is adjusted to be incident within the microfluidic channel and when a droplet passes the laser light, some of the light is back-scattered by the interface between the different refractive indices. The back-scatter is then detected by a photodiode, triggering a camera which takes an image of each droplet. From this image, droplet size measurements can be made by measuring the diameter of the droplet within the camera image and from this, the volume can be calculated using the equation found in **Section 1.3.9**. The LabView software then calculates the change in pressure needed to keep the droplet volume at the target volume (as shown in **Section 2.2.5**). This new target pressure is fed to the pressure pump, which changes the input pressure and therefore the flow rate of the aqueous inlet. This allows the droplet volume to remain at a constant volume, accounting for any drift.

A secondary feedback loop can be implemented to control the frequency of droplet production by regulating the pressure at the oil inlet. This frequency is calculated by counting the number of peaks detected in the backscatter signal by the detector each second. If the frequency drifts or a change in the frequency is required, the feedback loop will slowly alter the oil inlet pressure while prioritising the initial feedback loop to maintain monodispersity.

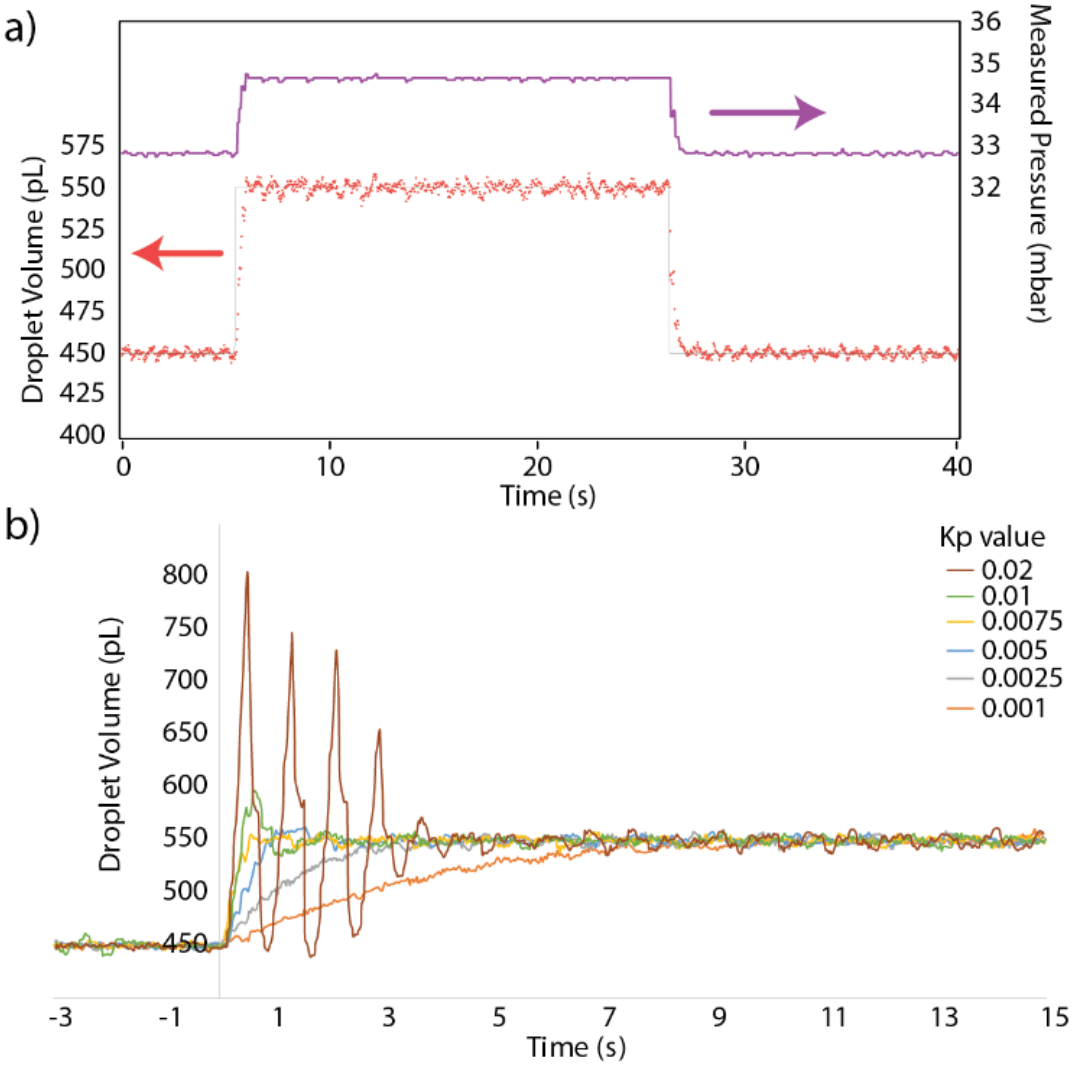

Figure 3.3 (a) *Response of the droplet formation to a change in wanted droplet volume. The volume of each droplet created (red dots) quickly follows the wanted droplet profile (black line) as the pressure at the aqueous inlet is changed (purple line).* **(b)** *Optimisation of the dominant feedback parameter K_p, for a step change in wanted droplet volume from 450 pL to 550 pL, showing the slow responses at low values and oscillation at large values.*

3.3 Calibration of image-based feedback

As with all feedback based systems, the control parameters of the feedback loop are critical to a fast response system. The parameters need to be chosen to provide the optimum conditions between a slow response and overshooting and oscillation. There are three factors which control the changes in input pressures; K_p, K_i and K_d. These are the proportional, integral and derivative constants respectively and are explained more in **Section 2.2.3**. K_p was the dominant term and had to be optimised. **Figure 3.3b** shows the response to a change in the wanted volume from 450 to 550 pL for different values of K_p. As expected, low K_p values (0.001, 0.0025) result in underdamping with a slow response to the desired change, while very high values (0.01, 0.02) result in

overdamping with oscillations around the target value. Changes in K_d and K_i had smaller effects on the response and for the rest of the work the values were kept at $K_p = 0.005$, $K_d = 0$ and $K_i = 0$, where critical damping occurred within 0.5 s.

3.4 Comparing microdroplet generation methods

With the feedback system optimised, it was important to investigate how this system can improve the monodispersity of microdroplet formation. To do this the monodispersity of the droplet volume was measured for both the developed image-based feedback system and three current techniques; a stepper motor driven syringe pump, a pulseless syringe pump and a constant pressure, air over liquid pump without feedback enabled. For each system a minimum of 15,000 300 pL droplets were measured over 50 minutes. **Figure 3.4c** shows that the distribution of microdroplet sizes created using the stepper motor driven syringe pump is relatively broad with periodic oscillations. This behaviour can be understood in terms of the discrete movements of the stepper motor which drives the syringe[117,260]. Significantly narrower distributions can be achieved using pulseless syringe pumps which do not show the same oscillations. However, when compared to pressure driven pumps, which apply a constant pressure, the distribution is still very broad. These oscillations can be seen at smaller time scales as shown in **Figure 3.4b**. Although the applied pressure remains constant through the experiment, the flow rates in the device may change due to channel fouling, leaking or the height of the liquid in the outlet changing. These are variables that cannot be controlled for and any one of which can lead to long-term drift in the droplet volume (see **Figure 3.4a**). This can be countered by using a flow meter placed in the fluid path, with a closed feedback loop. However, the droplet size produced in using a constant flow rate system can also

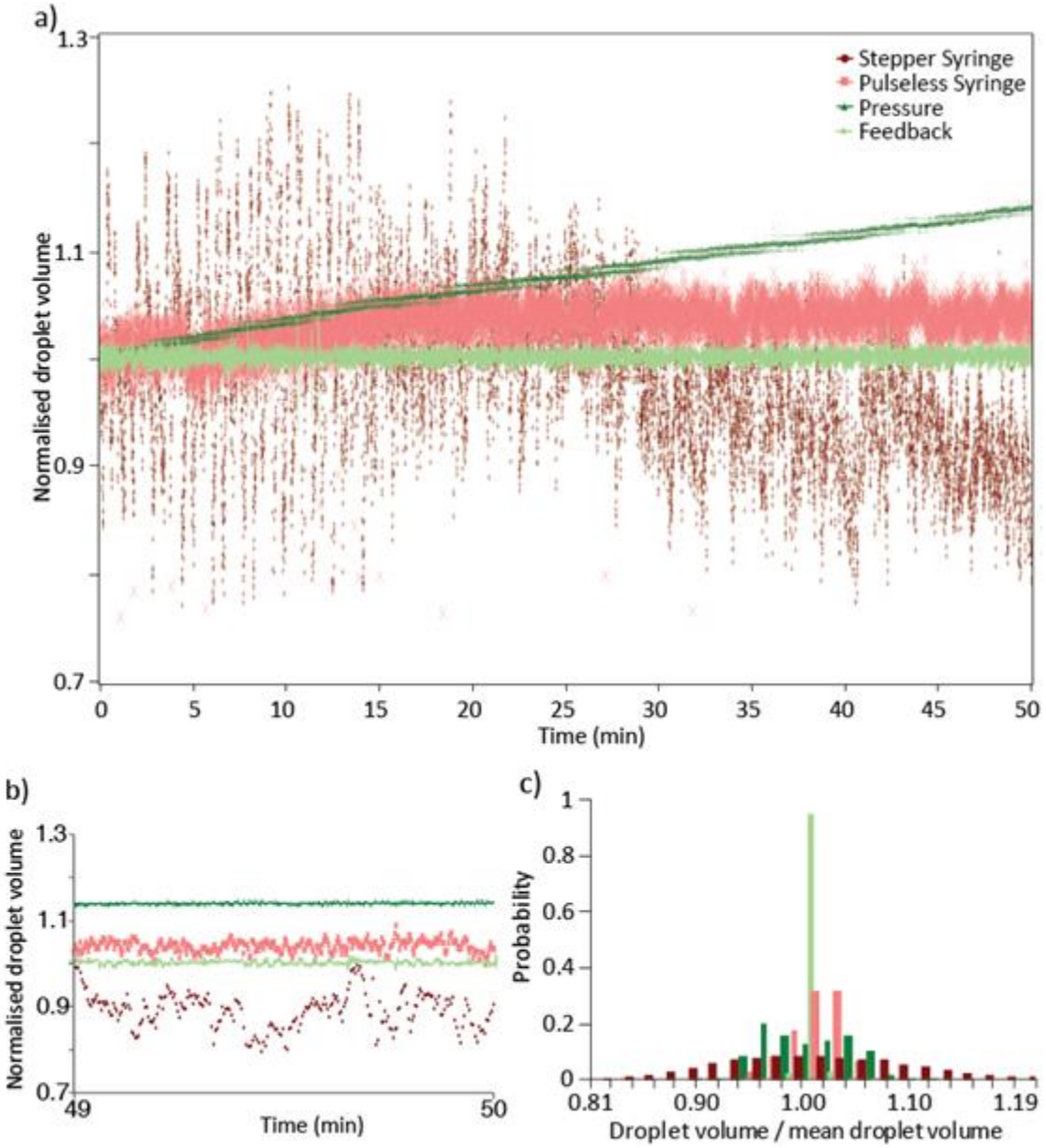

Figure 3.4 (a) *Normalised droplet volumes over a 50 minute timescale created using constant flow rate, stepper motor driven syringe pumps (dark red), pulseless syringe pumps (light red), constant pressure pumps (dark green) and image-based feedback driving a pressure pump, producing droplets at 50 Hz (light green). The improvement in monodispersity of the pressure based systems and the drift cancelling effect of the feedback can be clearly seen.* **(b)** *Detailed view of the changes at short timescales, showing the oscillations due to the syringe pump and drift due to the constant pressure pump.* **(c)** *Normalised histograms of the normalised droplet volume for each of the methods shown.*

change due to temperature changes, fouling or surface wetting effects. Additionally, the flow meters are often limited in the range of liquids which can be used, and can be easily blocked by objects in the liquid such as microparticles or cells, thus limiting their applicability.

	Coefficient of Variation	*Fraction of droplets within percentage of mean volume*		
		5%	*1%*	*0.50%*
Stepper motor syringe	10.98%	41%	9%	*4%*
Pulseless syringe	5.42%	97%	30%	*17%*
Pressure	3.78%	82%	13%	*6%*
Feedback	0.32%	100%	99.70%	*88%*
Frequency feedback	0.40%	100%	98.60%	*80%*

Table 3.1 *Measurements of the distributions in droplet volume measured over a 45 minute period showing the improvement in monodispersity when using active feedback to control droplet production.*

Imaging the droplets provides a more accurate metric of the droplet size than the input flow rates, and by feeding back this information, it is possible to improve the long-term monodispersity of the droplet production, as shown by the distribution data shown in **Table 3.1**, without placing anything in the fluid path. The coefficient of variation in the volume of droplets, created using image based feedback, is significantly improved over the other methods tested and even when compared to using the pressure pumps the coefficient of variation reduces from 3.78% to only 0.32% for 300 pL droplets created over a 50 minute period. This value is close to the resolution limit of our system, which was measured to be the equivalent of 0.19% (the smallest change in pixel size the camera can measure divided by the diameter of a 300 pL droplet).

To confirm that the feedback system provided consistent results, repeats of droplet creation were performed. Three different PDMS devices with identical designs were used with new tubing, new oil and new water with the same software. As can be seen in **Figure 3.5**, without the feedback there is a constant drift of variable gradient (orange and

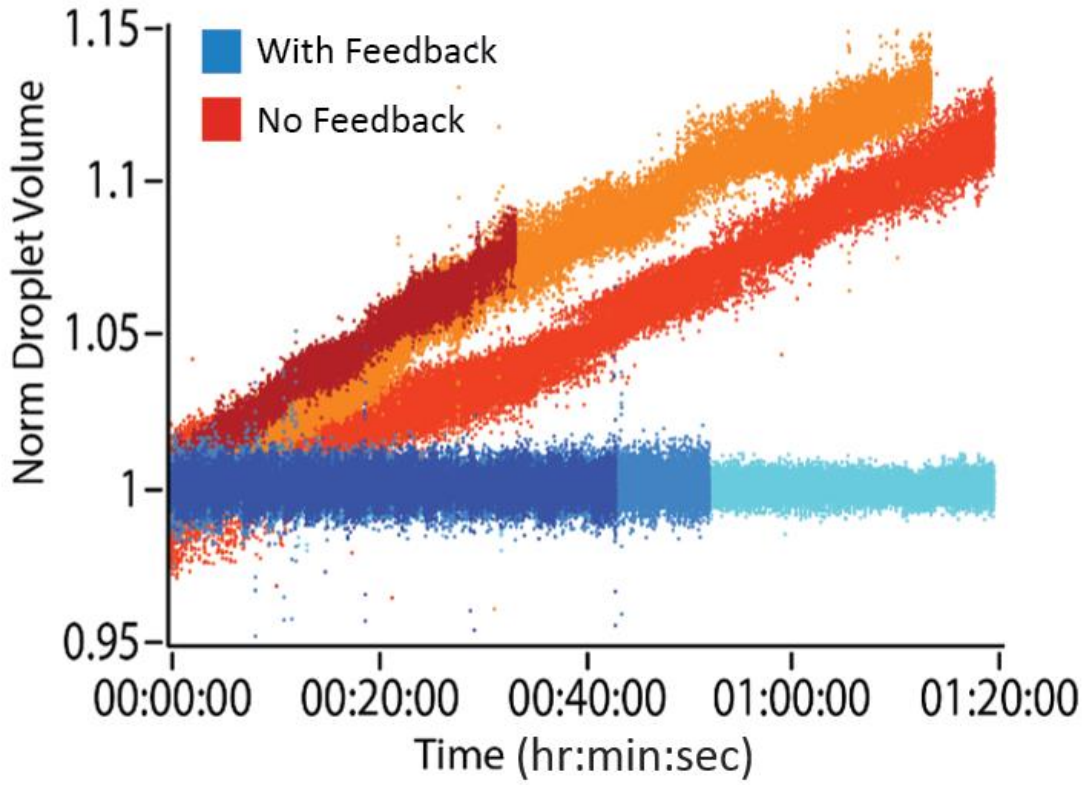

Figure 3.5 *Repeats of droplet creation using pressure pumps both with and without feedback. Droplets were created on different days using different devices of identical design. The repeats without feedback (red and orange) drifted at different rates, while the repeats using the feedback system continued to stay around the required droplet volume.*

red data) The coefficients of variation are also of the same magnitude, 0.47%, 0.50% and 0.43%; all of which are better than previously recorded levels of monodispersity as described in **Section 1.3.14**[124]. There is no drift over time as observed when the feedback loop is applied (blue data). The rate at which the non-feedback drift occurs was measured by linearly fitting the data. Gradients of 0.13 h^{-1} (dark red data), 0.10 h^{-1} (light orange data) and 0.09 h^{-1} (dark orange data) were measured. Although the drifting effect occurs in all cases, the rate at which this occurs is not. Without a consistent drift rate, a linear fix cannot be applied to compensate for the increase in droplet size. The feedback system must be applied to repeatedly adjust the pressure pumps to accommodate for this drift and to keep droplet volume consistent.

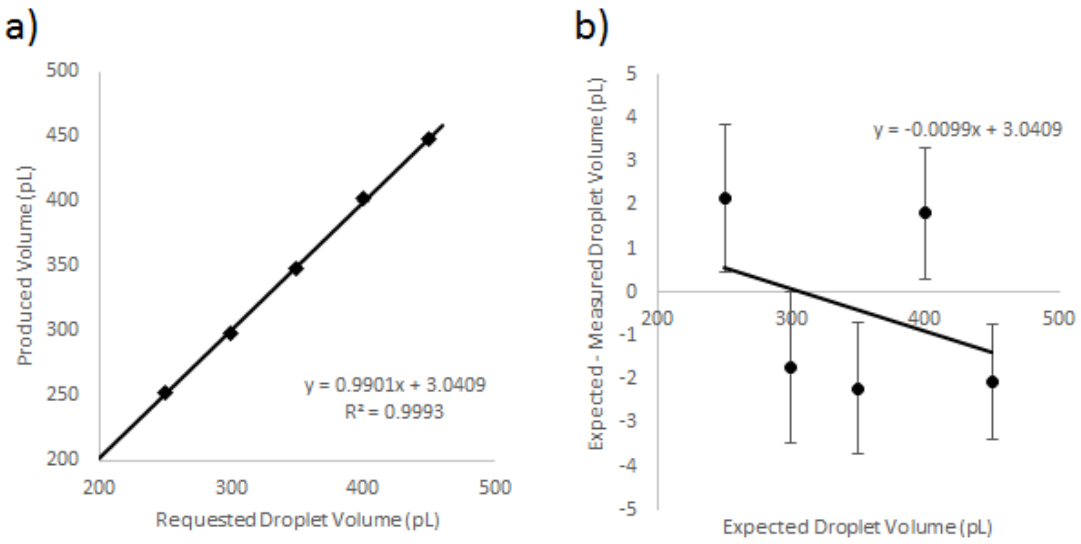

Figure 3.6 (a) *The droplet size produced by the pressure pump with feedback system was confirmed by comparing the input droplet volume controlled by the image feedback system and by removing the droplets from the device and measuring them on a glass slide. The droplet size measured was consistent with that of the input volume. Error bars are present and were calculated using the standard deviation of the measured droplet sizes.* **(b)** *The deviation from the required volume of the measured droplet volume is shown. The error bars are very small and represent the standard deviation of the deviation of each measured droplet.*

3.5 Confirmation of droplet volume measurements

To confirm that the droplet volume being measured within the device using the imaging feedback system was correct, droplets were created at various volumes and measured. The droplets were collected from the outlet of the device and placed onto a glass slide. Images were taken using a camera (ProSilica GE680) and measured using an image processing program (ImageJ). The diameter of the droplet was measured in pixels, using ImageJ, converted into the physical size and finally the volume for each droplet was calculated assuming the droplet is a sphere. 33 droplets for each volume were measured for the five selected input droplet volumes. The measured droplet size was plotted against the expected droplet size in **Figure 3.6a**. The droplet size was found to be consistent with the expected size with a standard deviation of less than 1% for each droplet size measured. The gradient was measured to be 0.9901 and if the trend line is clamped to the origin it gives a gradient of 0.9985. **Figure 3.6b** shows the difference between the expected and measured droplet volumes against the expected droplet volume. This contains the error bars seen in **Figure 3.6b**, calculated using the standard deviation of measured droplet volumes. A gradient of almost zero (-0.0099) and sporadic positioning of points both above and below the x-axis suggests there is no systematic error in the volume calculation.

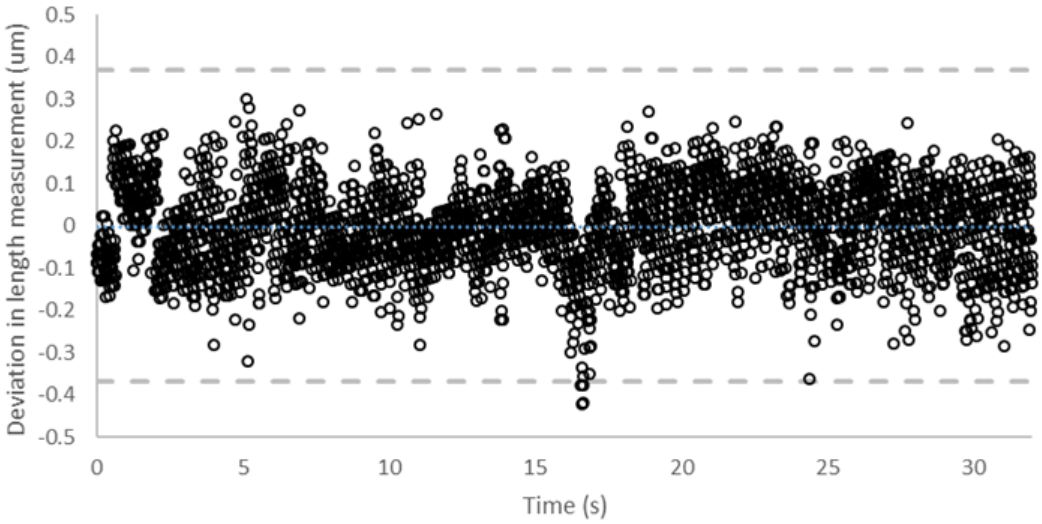

Figure 3.7 *Measurement of the error in length estimation. A stationary droplet was imaged >3600 times as the stage and camera oscillated and the length measured and volume calculated, grey lines represent the width of one pixel.*

To test for any errors in imaging the droplet and in taking a length measurement, a single stationary droplet was measured over 3600 times. Any oscillations in the equipment will have an effect on the droplet length measurements; and so the stage was moved gently to see if this would affect the calculation. As can be seen in **Figure 3.7** the measurements were unaffected with all but 3 of over 3600 images, being within a single pixel width of the mean droplet length. The measurement of droplet length uses quadratic interpolation to find the middle of the intensity peaks, giving sub-pixel accuracy of the length measurement, with a standard deviation of <100 nm, which explains this high accuracy.

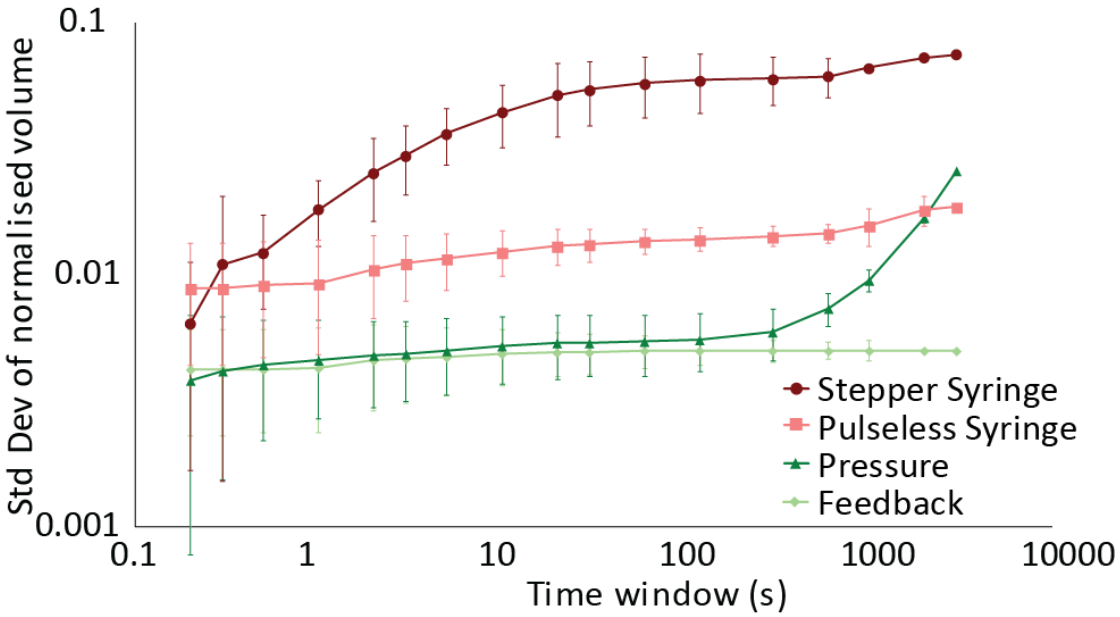

Figure 3.8 *Changes in the distribution of droplet sizes taken for different time windows for the syringe pumps (red and pink), constant pressure pumps (dark green) and image-based feedback controlling pressure pumps (light green). At short timescales the two pressure based systems perform identically, however over long time periods, the drift of the constant pressure system becomes apparent while the image-based feedback remains constant.*

3.6 Microdroplet monodispersity at different time scales

By measuring the standard deviation of the distribution of microdroplet sizes within a given time window, the timescales over which the system is changing can be investigated (**Figure 3.8**). As expected, the syringe pumps show a larger distribution even at short timescales, while the two pressure pump systems have very similar responses over short timescales. At larger timescales the standard deviation of the pressure pump system without feedback becomes greater. This is due to the pressure drift, which in turn causes the droplet volume to gradually increase or decrease. By compensating for the inherent drifting of the flow rates, the feedback results show consistent monodispersity across the range of times measured and are therefore the preferable droplet generation method for both short and long timescales.

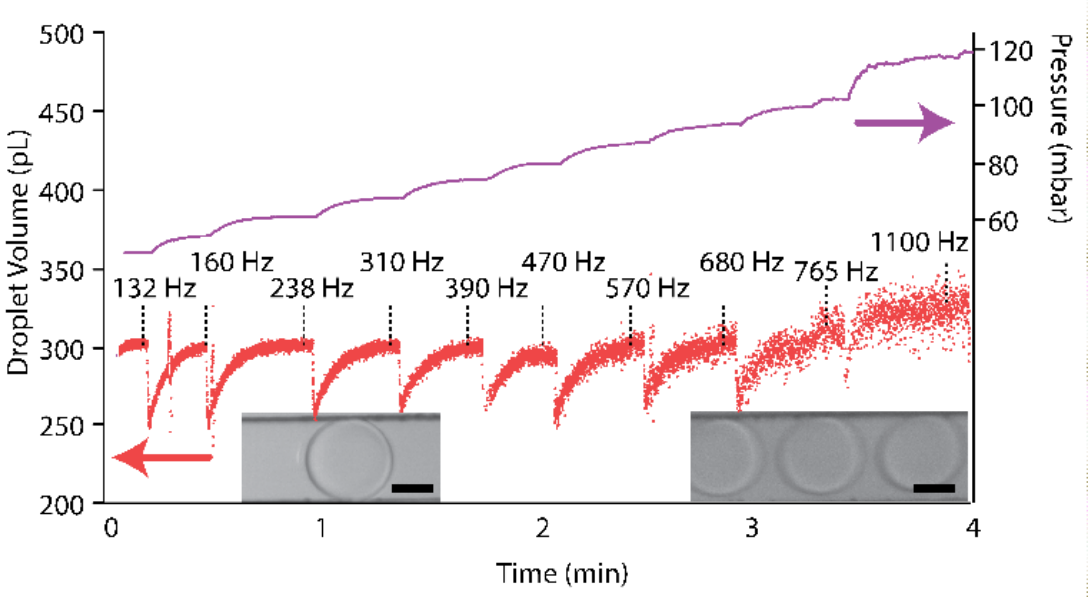

Figure 3.9 *Droplet feedback maintaining droplet volume (red dots) at high droplet formation rates. The oil pressure was increased stepwise and the feedback system was allowed to optimise the aqueous pressure (purple line) to form 300 pL droplets. At higher pressures, the increase in the error in the droplet volume is in part due to motion blue from the fast moving droplets. Insets: images of the droplets at low flow rates (left) and high flow rates (right) showing the increased motion blur. Scale bars are 50 µm.*

3.7 Performance of monodispersity at varying frequencies

All experiments described previously were performed at microdroplet production rates of 50 Hz. To test the capabilities at higher droplet production rates, the oil pressure was increased in a series of steps and the feedback algorithm modified the aqueous pressure to maintain the wanted droplet volume of 300 pL. **Figure 3.9** shows that at low pressures the algorithm can maintain the wanted droplet volume at high production rates. Due to the time taken to transfer the images, process them and save the data, the processing loop is limited to ~250 Hz, thus the size of every droplet cannot be measured at droplet formation rates above this. However, to combat this limitation, an assumption that the imaging captures a representative sample of droplets can be made. The change in droplet volume between consecutive droplets is small compared to that over long time periods and so if the camera misses a droplet, its volume will be almost identical to that of the droplet in the next image. Fast camera imaging of droplet formation at high flow rates confirms the assumption that the variation of droplet volumes within 0.1 s is smaller than the variation seen at the second timescale. At very high pressures (>100 mbar per channel), the linear droplet speed through the channel induces motion blur of the image, resulting in higher uncertainties in the droplet volume. Shorter exposure times (the camera used in this study was limited to 40 µs) or stroboscopic illumination would reduce

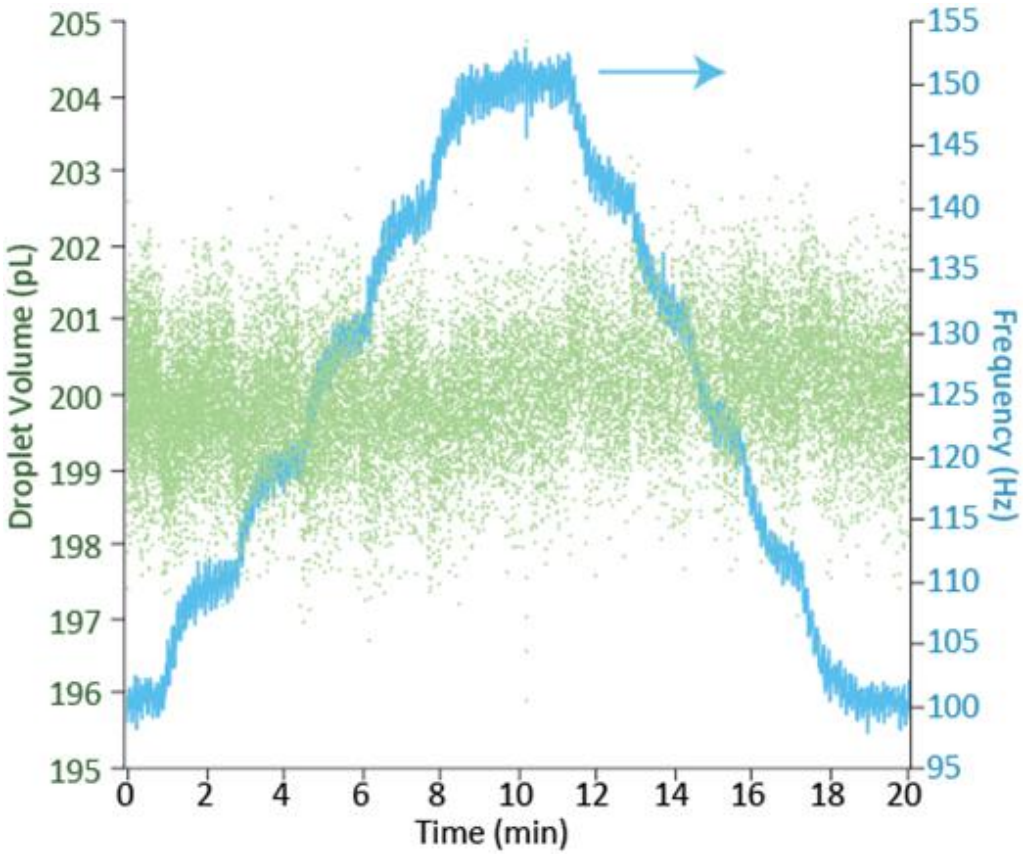

Figure 3.10 *Response of the frequency (blue) and droplet volume (green) due to the frequency feedback system which controls both the aqueous and oil pressures to allow feedback control of both volume and frequency. The required frequency was increased in increments of 10 Hz from 100 Hz to 150 Hz and then back down to 100 Hz with only slight effects on the resulting droplet volume.*

this effect. The use of line cameras to image the droplet would simplify the processing and increase the possible frame rate, allowing faster responses and quality assurance by measuring the size of every droplet, even at high formation rates.

The relatively simple processing required to implement this system could also be performed by a microprocessor and integrated directly with the pressure pump to provide a straightforward system for generating droplets of a given size. Using the faster frame rate, droplet formation remained stable for frequencies up to a limit of 1 kHz.

3.8 Feedback for the frequency of microdroplet generation

The system is not limited to a single feedback pressure. To demonstrate this, a secondary feedback loop was added to alter the oil pressure in order to control both the volume and frequency of droplet production. The droplet frequency was measured from the back-scatter signal which was monitored by a microprocessor, which in turn triggered a counter on each droplet passing. The frequency can be calculated by counting the

number of triggered voltages per second. The software then controllably alters pressures accordingly until the required droplet frequency is obtained. By tuning the feedback parameters, it is possible to prioritise the different measurements. To maintain the high monodispersity, it is important that the feedback loop of the volume acts faster than the frequency, allowing the volume to stay constant even while changing the oil pressure. Therefore, the optimum K_p value for the frequency was set to be 0.0025, smaller than the K_p value for the volume (0.005).

To test the droplet monodispersity when both the volume and frequency feedback systems are running, droplet production frequency was initially set to 100 Hz and then moved up to 150 Hz and back down to 100 Hz, with the required microdroplet volume remaining constant at 200 pL (**Figure 3.10**). As can be seen by the blue data, the time taken for the frequency to stabilise after a change was about 30 seconds.

The uncertainty in the volume was measured to be 0.40%, similar to the that measured when only microdroplet volume feedback was present (0.32%), and so is unaffected by the fluctuations of the pressure pumps caused by the frequency feedback loop. 98.6% and 88% of droplets were within 1% and 0.5% of the mean droplet value. This secondary feedback element allows for even more control in the users microdroplet production, with more consistent volumes than previously produced.

The drift in the droplet frequency as time progresses was investigated and the results can be seen in **Figure 3.11**. Uniform droplet formation was observed at 1 kHz using the stroboscopic illumination described in **Section 3.7**, but at these high droplet formation frequencies the frequency was found to drift with time (blue data points in **Figure 3.11**). This frequency drift can be corrected using the secondary frequency feedback system, as shown by the red data.

The coefficient of variation of the 200 pL droplets created, both with and without frequency feedback, at 1 kHz was 2.4 pL (1.2%); this was measured over 5 minutes. This is higher than the coefficient of variation presented in **Table 3.1** and is due to the reduced light levels when using the 1 µs strobe illumination and the resulting lower signal to noise ratio. Although, there was less variation in the droplet volume when compared to the measurements at 1 kHz as seen in **Figure 3.9**, highlighting the benefits of stroboscopic illumination at high droplet generation frequencies.

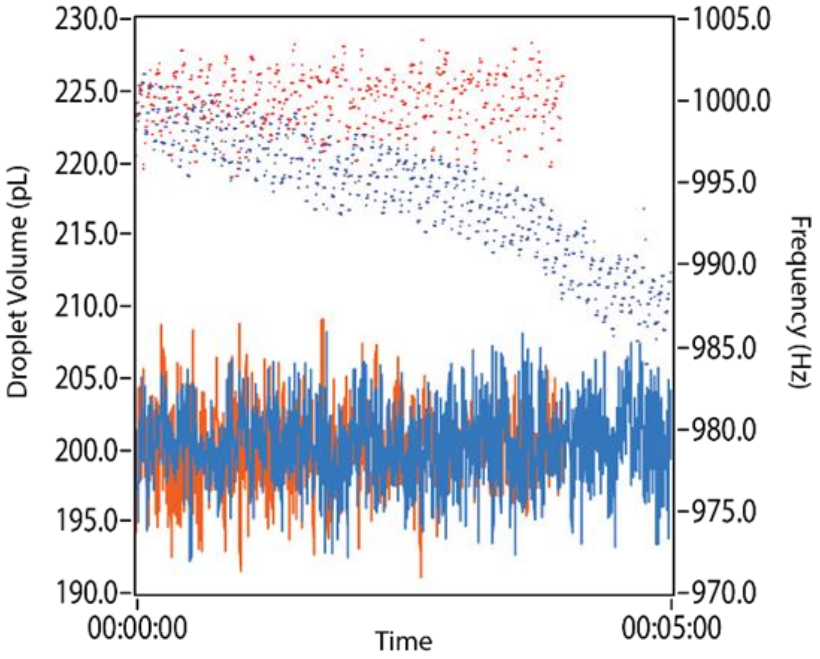

Figure 3.11 *Droplet volumes (lines) and frequencies (points) of droplet creation both with (red) and without (blue) frequency feedback turned on. The droplet volume was set at 200 pL and the frequency of droplet generation starting off at 1 kHz. In both cases the droplet volume remained consistent but the frequency was found to drift if the frequency feedback was not present.*

3.9 Application – Controlling cell concentration within microdroplets

To further demonstrate the potential for image-based closed-loop feedback, the feedback loop was modified to control two aqueous inlets in order to stabilise the concentration of cells encapsulated into microdroplets (**Figure 3.12a**). When cells are placed into a vial or syringe at the inlet of a microfluidic device, they will sediment due to the difference in density between the surrounding medium and the cells. This results in a changing cell concentration being introduced into the device. The nature of this change depends on the experimental setup, but there is generally a decrease in concentration when using syringes and an increase when using vials. This effect can be reduced by density matching the surrounding media with supplements such as Percoll[47] and OptiPrep[2,261]. To density match the cell solution, OptiPrep was added to the cell solution (28%) and this was seen to reduce the drop in cell concentration as the experiment progressed, as shown in **Figure 3.12b** and **Figure 3.12d**. However, even though OptiPrep improves cell concentration consistency there is still a gradual concentration drift. This is due to the inhomogeneous density of a cell sample and the

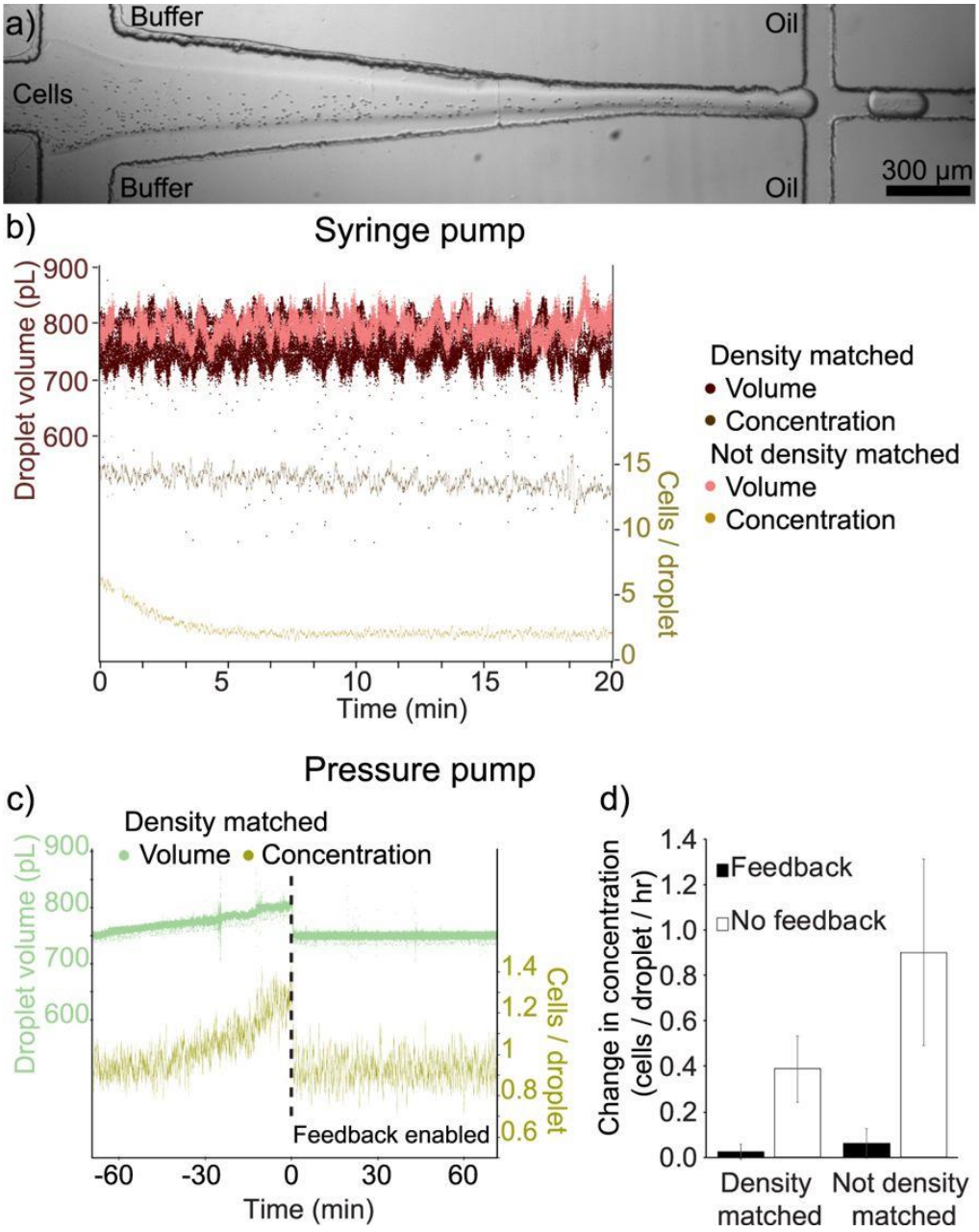

Figure 3.12 *Extension of the feedback system to stabilise average cell encapsulation concentrations in microdroplets. (**a**) Micrograph of the cell encapsulation device, consisting of an aqueous inlet for cell suspension samples which is diluted and flow focused by a dilution buffer, followed by flow focusing with an immiscible oil to form microdroplets. (**b**) Graph showing the variation in droplet volume (red) and average red blood cell count per droplet (yellow) when using syringe pumps. Cells placed in a syringe without density matching quickly settle and the concentration of cells encapsulated quickly falls (yellow curve). By density matching the sample to the cells, there is a slow drift in encapsulation concentration. (**c**) Graph showing the change in volume (green) and cell count per droplet (yellow) for pressure based pumps without feedback (time < 0) and with feedback (time > 0). Drift in the cell count is also present when using pressure pumps, as can be seen before feedback is turned on at time = 0, however this can be compensated for by feedback to alter the dilution factor. (**d**) Extracted rate of change of the cell count per droplet when using pressure pumps with and without feedback for density matched and non-density matched red blood cells. The plots show the mean gradient of linear fits to the cell count per droplet over a thirty minute period, error bars are the standard deviation (N = 3). Scale bar is 300 µm.*

fact that the density matching agent will never truly make the density of the solution match that of the cell sample, **Figure 3.12c**.

Image-based feedback can be used to compensate for this drift by dynamically altering the dilution on-chip. To do this, a device (**Figure 3.2d**) with two aqueous inlets (one with cell solution and one with buffer solution) and one oil inlet is used; where the first flow-focus junction dilutes the cell sample with the additional buffer solution, and a second flow-focus junction generates microdroplets in the same manner as the previous experiments. The number of cells in each droplet was calculated using the method in **Section 2.2.5** and to keep the cell concentration consistent the ratio of the two aqueous inlet pressures was adjusted using the feedback loop described in **Section 2.2.5**. The oil pressure at the oil inlet remains constant.

As seen in the previous experiments, without droplet volume feedback the droplet volume will drift. To prevent the number of cells per droplet changing due to a drifting droplet size, a secondary feedback system must be added to control droplet volume. This system is almost identical to that seen before, but instead of changing the pressure of one inlet, the total pressure across the first two inlets must change, while keeping the ratio between the two constant.

By controlling both the cell solution and buffer solution inlet pressures, the drift in droplet volume as well as cell concentration can be compensated for as shown in **Figure 3.12c**. Although the droplet volume drifts over time (~6% per hour), this cannot fully account for the change in cell concentration (~40% per hour) and so two feedback conditions are required to maintain monodispersed volumes and cell concentrations. **Figure 3.12d** shows that although the density matching agent can reduce the change in cell concentration by 57%, the use of the feedback system provides a greater improvement. When feedback is used the change in cell concentration is less than 7% of that seen when no feedback is used. For best results both OptiPrep and the feedback system can be used.

This experiment highlights that image-based feedback in microdroplet systems goes beyond controlling droplet volume and has the potential to be used in a number of applications.

3.10 Conclusions

By using an imaging system to directly measure the microdroplet volume and using this to enable feedback control over the input pumps, it is possible to improve the monodispersity in volume of the microdroplets formed over long time periods. The combination of closed-loop feedback and fast-response, pulseless, pressure-driven pumping allows highly monodispersed microdroplet samples to be created without prior knowledge of the fluidic properties of the liquids or system. Over a short timescale (seconds) the standard deviation of the pressure pump system both with and without feedback is similar, showing that the monodispersity of the droplets does not suffer in these small time periods. Over long periods the feedback system corrects any drift that may occur and the pressure pump system produces droplets with average volumes less noisy than that of syringe pump based systems. Additional feedback parameters can be added to further extend the control over droplet generation as shown by controlling the frequency of microdroplet generation or the concentration of encapsulated cells, to provide an easy to use and intuitive microdroplet generation system.

Chapter 4. Bright field image-based cell sorting

This is the first of two cell sorting chapters and makes use of the image acquisition and image analysis techniques from **Chapter 3** and applies them to moving cells within a microfluidic device based upon the cell image parameters. Image-based cell sorting is performed by implementing a brightfield image-based sorting technique, with piezoelectronics used to manipulate the fluid flow. Within the device, K562 cells and RBCs are imaged, categorised and sorted based on their morphology presented in the captured image; with an efficiency and purity of 91.3% and 99.4% respectively. The cell model, imaging setup and software will be updated in **Chapter 5** to allow for fluorescent nuclear morphological sorting, but the same piezo sorting device design will be used.

Outputs:

- Crawford, D.F., Whyte, G. Image-based microfluidic cell sorting, Poster session presented at: SelectBio Lab-On-A-Chip and Microfluidics 10th annual conference; 5-6 June 2018; Rotterdam, The Netherlands.
- Heriot Watt IB3 2nd year research prize.

4.1 Overview

Image-based cell sorting[35,252,253,255,256] is an emerging technique, as described in **Section 1.8**, which allows cells with unique spatial morphologies to be isolated and studied. A guide to the recently published IACS technique describes the requirement of expertise in many field areas; optics, electronics, digital processing, microfluidics, mechatronics and flow cytometry, with a PI also needed for project management[35,262]. For most laboratories this high end technique may not be feasible, with high initial start up costs and skilled personnel required; and so this work demonstrates a reproducible microfluidic technique which can be performed using a three camera, microscope setup and easy to manufacture microfluidic devices.

The combination of cell imaging, image processing and piezoelectronic based cell sorting has resulted in an effective way to accurately categorise and manoeuvre different cell types into homogeneous subpopulations. A mixed population of red blood cells (RBCs) and K562 cells have been imaged, analysed and sorted using this method. There is a compromise between imaging at high resolution and the field of view, so previous sorting papers have often had low resolution images of the cells because they needed to see the whole device to monitor the performance. Here, these two tasks have been decoupled with one camera looking in high resolution at the cell morphology, while a second camera is used to overview the device, to view the trajectory of the cells. The ability to locate the cells within the device allows the cell sort to be actuated and the success of which, confirmed. The imaging software is able to locate the cell within the cell image, calculate its projected area and then characterise it into one of two populations. This method successfully resulted in 91.3% of K562 cells being sorted from a mixed K562 and RBC population, with a purity of 99.4%. The following chapter (**Chapter 5**) continues on this path to further improve and expand the capabilities by combining fluorescent imaging and microfluidics to sort cells based on their nuclear morphology.

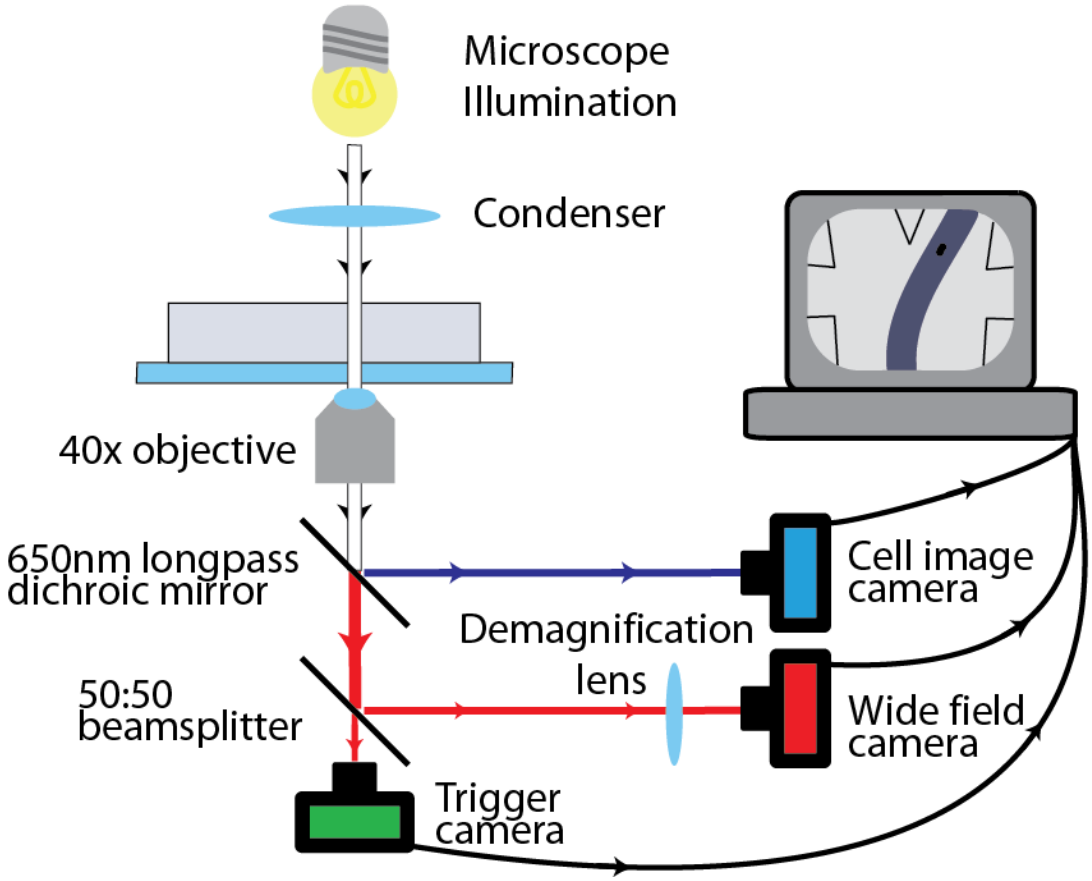

Figure 4.1 *Schematic diagram showing the setup used for image based cell sorting. A microscope is used to illuminate and image the cells. The cell image is split into three cameras. One for imaging the cell (blue), one for determining when the cell is in the sorting region (green) and one for viewing the trajectory of the cells (red).*

4.2 Experimental setup

4.2.1 Optical setup

The system was set up as shown in **Figure 4.1**, where the sorting device was mounted onto an inverted microscope (AE31, Motic). The microscope illumination passes through a condenser lens and onto the microfluidic device. The image produced passes through the 40x oil immersion objective (Olympus) and is split into three paths. A dichroic mirror reflects lower visible wavelengths (<650 nm) into the cell image camera (Thorlabs 340M-USB) while allowing the infrared light to pass through. This IR light is further split using a 50:50 non-polarising beam splitter. The two light paths are imaged by the wide field camera (Allied Vision Mako G-234B POE), via a plano-convex demagnification lens and the trigger camera (Allied Vision Mako U-130B). The field of views of these three cameras can be found in **Table 4.1**, while their imaging regions can be found in **Figure 4.2**.

Camera	Image size (pixels)	Pixel size	Field of view
Cell imaging	**640 x 480**	**0.12 µm**	**76.19 µm x 57.14**
Trigger	**100 x 904**	**0.10 µm**	**9.7 µm x 88.6 µm**
Wide field	**800 x 636**	**0.22 µm**	**177.8 µm x 141.3 µm**

Table 4.1 *Image size and field of view dimensions of the three cameras in use.*

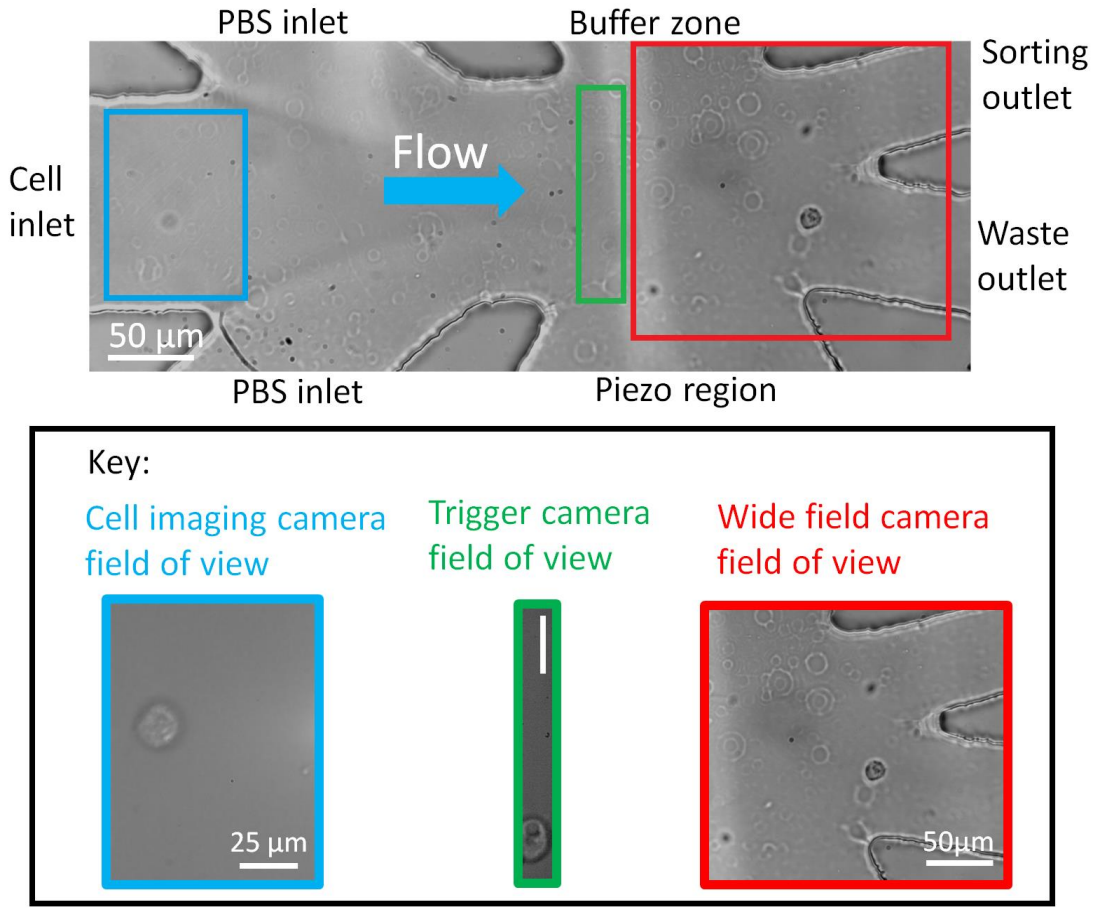

Figure 4.2 *Micrograph of the cell sorting device. Due to the refractive index contrast between the cell solution and the PBS, the flow focusing effect can be observed, with the cells being directed towards the waste outlet. The three coloured regions show the field of views of the cameras. The cell imaging camera (blue) images the cell within the cell inlet, the trigger camera (green) detects the cell once it is parallel with the piezo region and the wide field camera (red) confirms which outlet each cell has been sorted into. The scale bar on the trigger camera image represents 25 µm.*

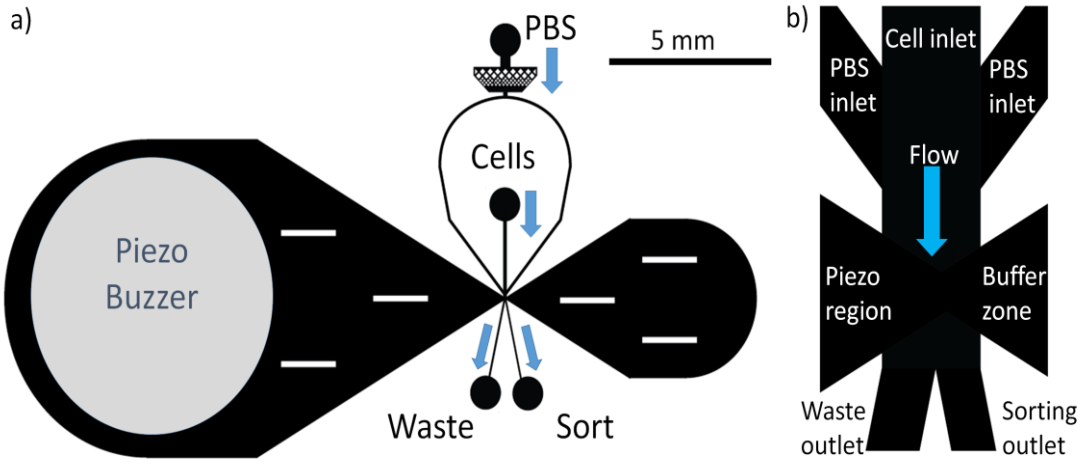

Figure 4.3 (a) *Diagram of cell sorting device. Cells are injected into the middle inlet while PBS in injected into the top inlet to flow focus the cells into the middle of the channel. The cells then flow into either the waste or sort outlet. The cells will flow into the waste outlet unless the piezo buzzer fires. This causes a jet of water to push the cell trajectory into the sort outlet, resulting in a successful sort.* **(b)** *Close up of the sorting region of the device.*

4.2.2 Microfluidic device

To ensure all cell images are in focus, the microfluidic device is 30 µm in height (slightly larger than the diameter of a K562 cell, 20.94±1.08 µm[263]) and so the focal plane of the objective can be adjusted into the middle of the channel. The device contains two inlets and two outlets and the whole design is shown in **Figure 4.3a**. The cell solution (described in **Section 4.2.5**) is injected into the cell inlet, while the flow focusing PBS solution is injected into the flow focusing inlet. The flow focused cells then travel into either the waste or sorting channel, both of which contain outlets. The piezo buzzer is placed above a reservoir of liquid and when actuated, the displaced liquid is focused into the sorting region of the microfluidic device (see piezo region of **Figure 4.3a**). There is also a buffer zone to allow for a smoother cell trajectory**. Figure 4.3b** shows the full cell-sorting region within the device. A pressure based system similar to that seen in **Chapter 3** was trialled initially, but the feedback system needed to direct the cells between the two outlets would have restricted the throughput. Therefore, the piezo actuated cell sorting design was adopted to provide the potential for throughputs of over 1000 cells per second[36].

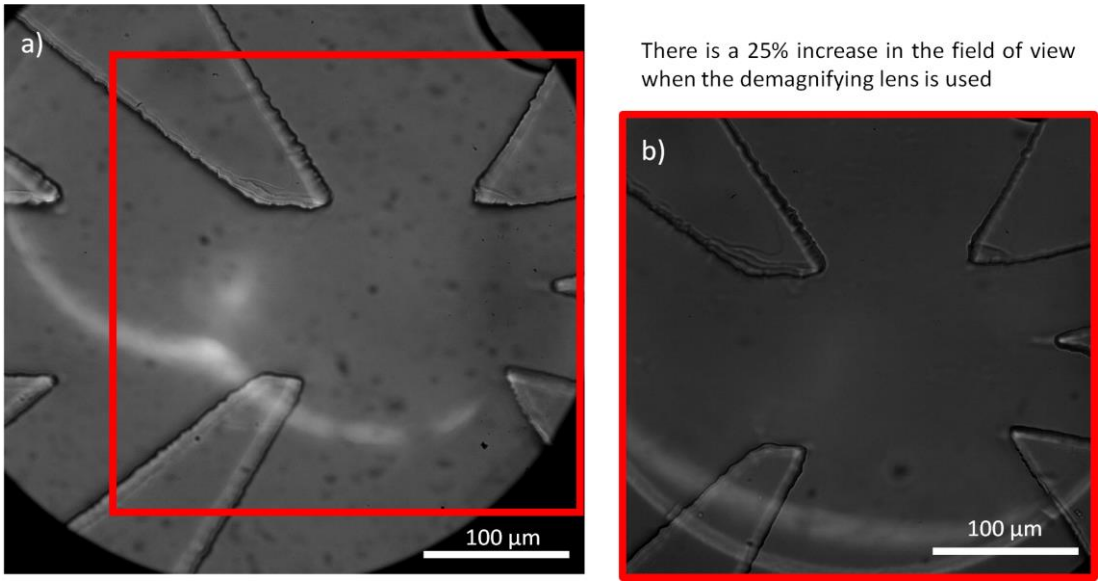

Figure 4.4 *Images of the sorting region within the microfluidic device taken by the wide field camera.* **(a)** *Image taken with the demagnification lens in front of the camera, leading to a 25% increase in the field of view.* **(b)** *The same image taken without the lens. Notice the cell inlet channel is not visible.*

4.2.3 Demagnification lens

To allow for both the cell inlet channel and the sorting channels to be viewed at once, a demagnification lens is placed in front of the wide field camera. This increases the field of view by 25%, as seen in **Figure 4.4**, aiding analysis of the cell trajectory. As the region of interest is reduced during a cell sort, the demagnification allows for a reduced image size to be used when imaging an equivalent area; resulting in a larger framerate of recorded videos used to confirm the success of the sort. The field of view of the all three cameras can be found in **Table 4.1**.

4.2.4 Visualising the flow

The larger field of view described in the previous section allows for a larger area of the sorting region to be viewed and this helps with positioning the flow focused cell solution into the waste channel. It is important that the cell flow is positioned close to the inner channel wall of the waster channel; too far one way and the waste cells may flow directly into the sorting channel, too far the other way and the piezo pulse may not be strong enough to move target cells into the sorting channel. If the cells are suspended in the same PBS + pluronic solution as the flow focus solution, the flow cannot be visualised as seen in **Figure 4.5a**. To create a contrast between the cell solution and the flow focusing solution, initial tests were done using Trypan Blue, as seen in **Figure 4.5b**. By gradually raising and lowering the outlet vials, the flow path could be observed and

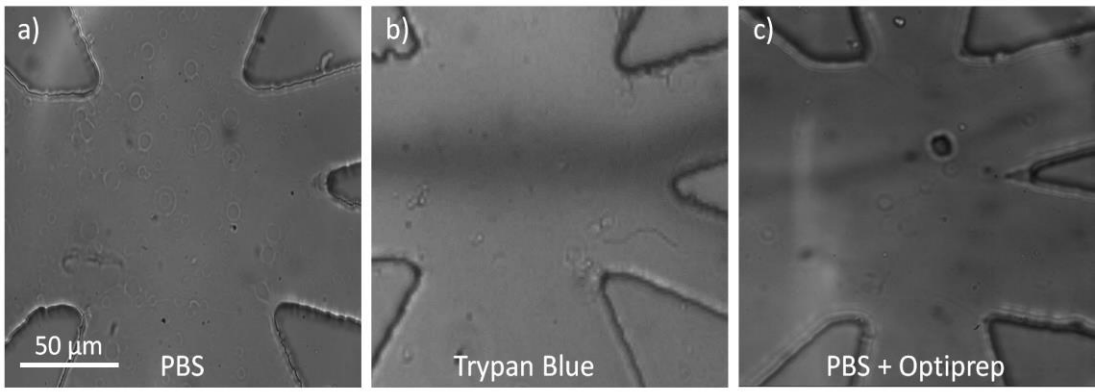

Figure 4.5 *Images of the flow focused cell solution.* **(a)** *cells in PBS solution.* **(b)** *cells in PBS + Trypan blue solution.* **(c)** *Cells in PBS and OptiPrep solution.*

moved into the required position. To prevent the cells from settling at the bottom of the syringes a density matching agent, OptiPrep, was used. It was observed that the cell solution containing OptiPrep appears darker than that of the PBS and so the flow path of the cells can be observed (**Figure 4.5c**). This is due to the refractive index, n_{ri}, difference between the cell solution, which contains OptiPrep[264] (n_{ri} = 1.42), and the flow focusing PBS[265] (n_{ri} = 1.34).

4.2.5 Cell solution preparation

To prepare the sample of mixed cell types the following process was carried out: PBS (without Calcium and Magnesium), with 1% dissolved pluronic powder, was prepared as a cell suspension media which maintains the cells for the duration of the experiment, but reduces adhesion of the cells to each other and the device surfaces. Fresh RBCs were obtained from a healthy volunteer via a skin prick, and diluted in the sample PBS to a concentration of 6 million cells per mL. K562s were removed from culture by pipetting, spun down and resuspended in the sample PBS, again at a concentration of 6 million cells per mL. These were mixed together with OptiPrep (33%) to maintain a more constant concentration throughout the experiment. OptiPrep has a density of 1.32 g/mL and PBS has a density of 1 g/mL, resulting in a final solution density of ~1.1 g/mL, which corresponds to that of an RBC. The final solution is made up of three equal parts, giving a final concentration of 2 million cells per mL for both the RBCs and the K562 cells.

4.2.6 Flow rates

The aforementioned mixed cell solution is fed into a 100 µL glass syringe and injected into the cell inlet by a pulseless syringe pump (Cetoni NeMESYS), via PTFE

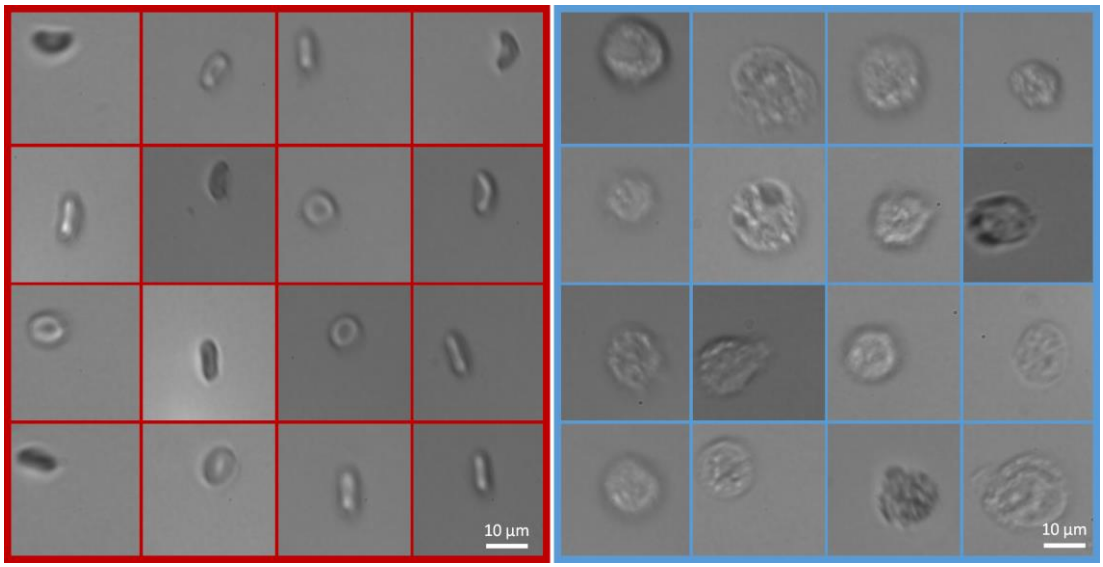

Figure 4.6 *Images of RBC (images within red box) and K562 cells (images within blue box) taken by the cell imaging camera.*

tubing. The flow focusing PBS (calcium and magnesium free PBS with 1% pluronic) is also injected using the syringe pump, but a larger 500 µL glass syringe is used. The same syringe driver is used for both solutions to maintain a constant ratio of flow rates, even if the flow rate is periodic or experiences pulsation. The flow rates of the cell solution and PBS are 3.4 µL/hr and 17.2 µL/hr respectively.

4.3 Cell imaging and image analysis

As the cells flow into the cell inlet, they will flow into the cell imaging region, the blue region in **Figure 4.2**, and will be imaged by the cell imaging camera. Images of K562 cells and RBCs taken by the imaging camera can be seen in **Figure 4.6**. These images taken are processed using LabView v2011. An initial background image of the sorting region is taken and subtracted from each further image. The greyscale image is converted into a binary image using thresholding; if the absolute difference in pixel intensity is above a certain threshold the pixel value will be 1. Alternatively, if the pixel intensity is less than the threshold the pixel value in the binary image is 0. The binary image may contain regions of pixels with values of 0 on the cell perimeter, as seen in **Figure 4.7c** and **Figure 4.7h**. This perimeter is important for calculating the cell area. To solve this problem, the convex hull area of the cell is calculated using a convex hull transform. This transform performed uses the extremal pixels of the binary image, with a value of 1, as the boundary coordinates; these coordinates create a perimeter, with the pixels inside the perimeter also given a value of 1 (as seen in **Figure 4.7d** and **Figure 4.7i)**

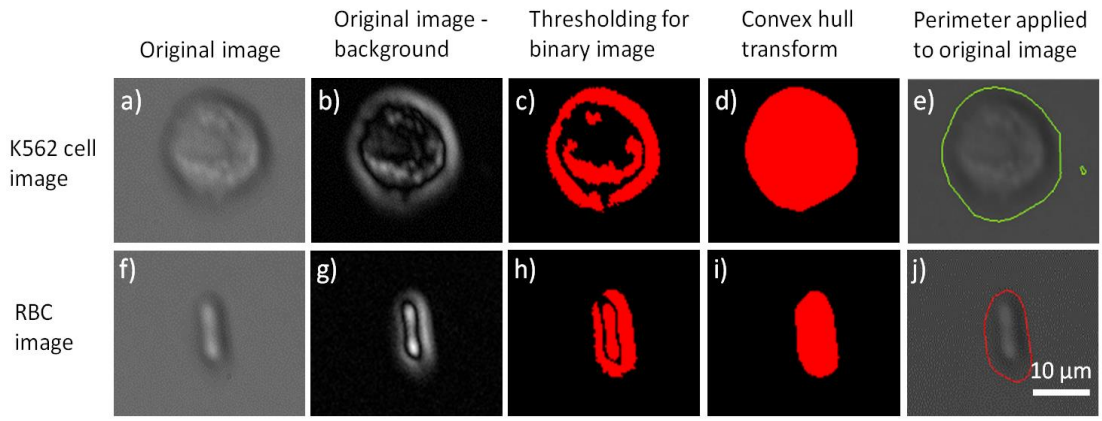

Figure 4.7 *Image processing of K562* **(a-e)** *and RBC* **(f-j)** *images.* **(a,f)** *Raw images of the K562 and RBC cells.* **(b,g)** *The background is subtracted from the raw images.* **(c,h)** *Using a threshold, these are turned into binary images.* **(d,i)** *The convex hull area of the binary image is calculated to remove any gaps on the cell perimeters. This value is used to determine if the cell is a K562 or an RBC.* **(e,j)** *This perimeter is plotted on the raw images.*

The area within this perimeter could then be calculated to provide the convex hull area. The values of the cell convex hull area were used to separate the images into three categories: no cell present if the area is less than 20 μm^2, a K562 cell if the area is above 120 μm^2, and an RBC if the area is between the two aforementioned values. In the two latter cases, images are recorded and numbered for later analysis.

4.4 Decision making performance

To test the decision making software, thousands of images of K562 cells and RBCs were taken in flow and their areas were calculated using the method described in **Section 4.3**. A histogram was generated, highlighting the fraction of each cell population which falls into one of 30 cell area populations (**Figure 4.8)**. The bins were from 0 μm^2 to 442.5 μm^2 and each covered a spread of 15 μm^2. On average, the area of RBCs was less than that of the K562 cells, but the variation in cell area was much greater in K562 cells, with some K562 cells being smaller than some of the larger RBCs. A cut-off value of 120 μm^2 was used to separate hits, which were K562 cells to be sorted; and waste, which were RBCs to be ignored. To test the deterministic ability of this characterising metric a ROC curve was generated as described in **Section 2.3.9**, (**Figure 4.9a**). The curve is very steep with the true positive rate reaching 0.9 when the false positive rate is only 0.0002. The area under the curve is 0.996, highlighting the success of this metric. To further investigate the robustness of the decision making, the efficiency and purity of various cell area thresholds were plotted in **Figure 4.9b**. The area thresholds used in

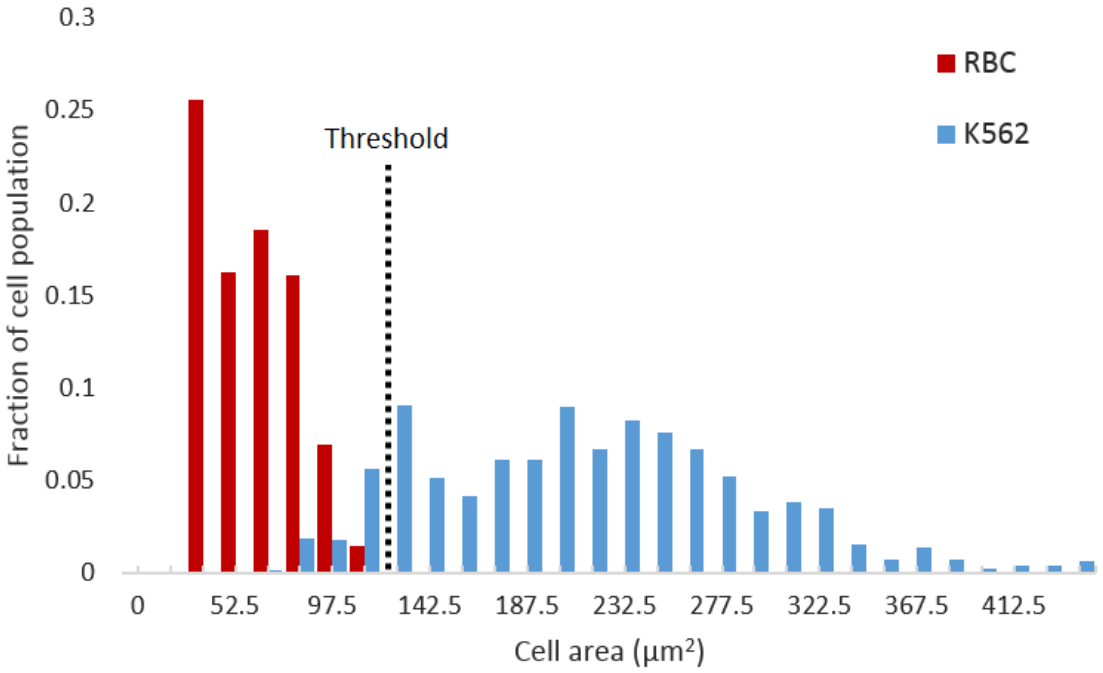

Figure 4.8 *Fraction of K562 cells (blue) and RBCs (red) with specific areas. As expected the area of most RBCs are smaller than that of most K562 cells. The spread of the K562 cells is greater than the spread of the RBCs and the smaller K562 cells overlap into the RBC region. A cut off area measurement of 120 µm² was used to separate the two cell types, with smaller and larger cells being determined as waste and hits respectively; the dashed black line represents this threshold.*

further experiments are from 105-115 µm and, as shown in **Figure 4.9c**, in this region the purity never falls below 0.98, while providing an efficiency above 0.92. Therefore, further experiments were carried out using an area threshold within this region.

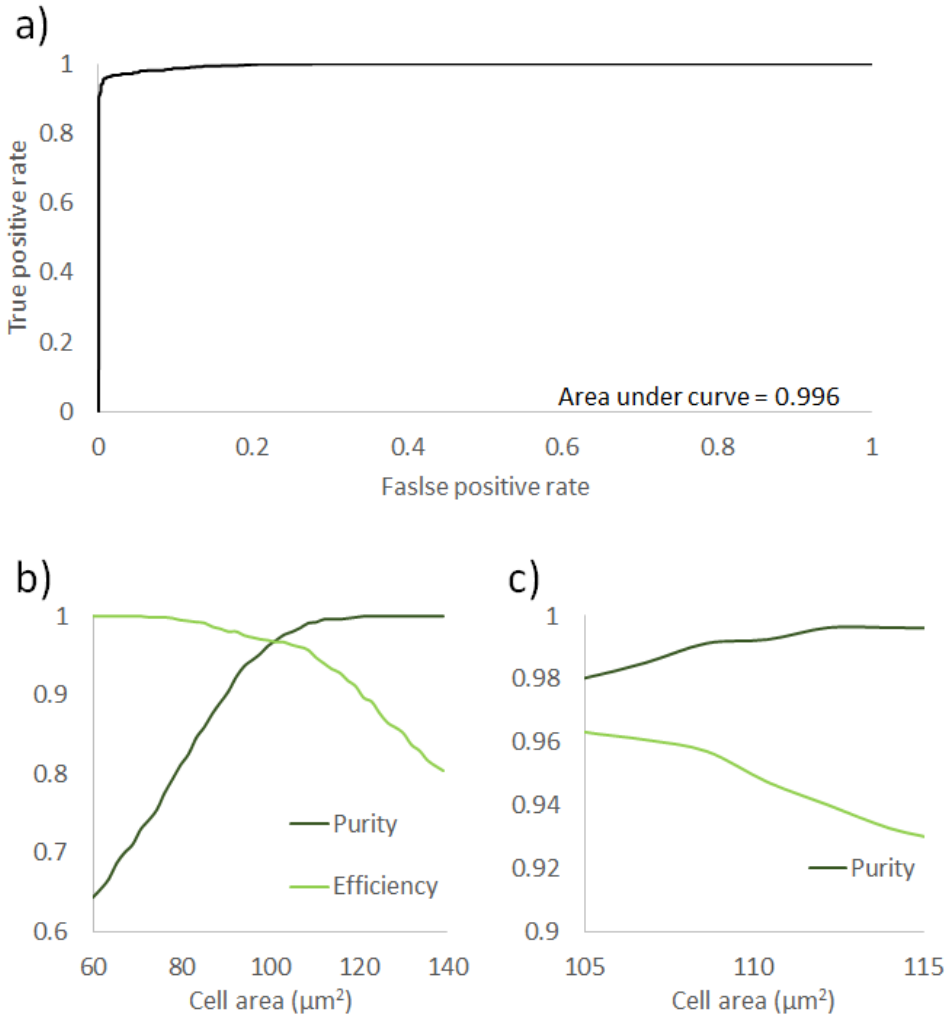

Figure 4.9 (a) *ROC demonstrating the characterisation success of the area threshold used to determine the difference between an RBC and a K562 cell.* ***(b)*** *The efficiencies and purities that can be expected when different area thresholds are used.* ***(c)*** *Close-up of* ***(b)*** *showing the efficiency and purity that can be expected with the used threshold.*

To test the decision making software in real time, the cell mixture of K562 cells and RBCs was passed through the microfluidic sorting device, with the software targeting K562 cells. In total, 1941 cells were imaged over three runs and the software classified them either as a "hit" (if a K562 was detected) or "waste" (if an RBC was detected). These images were saved into two folders, either "hit" or "waste" and each image within these folders was manually classified as correct or incorrect. The number of cells of each cell type, which were accepted and rejected, can be seen in **Figure 4.10**. As expected there are a number of K562 cells which will be sent to the waste outlet, roughly 8% of the total K562 population. However, the number of RBCs which were missorted is low and the purity of the hit population of K562s is 99.4% with 91.9% of the K562s correctly identified.

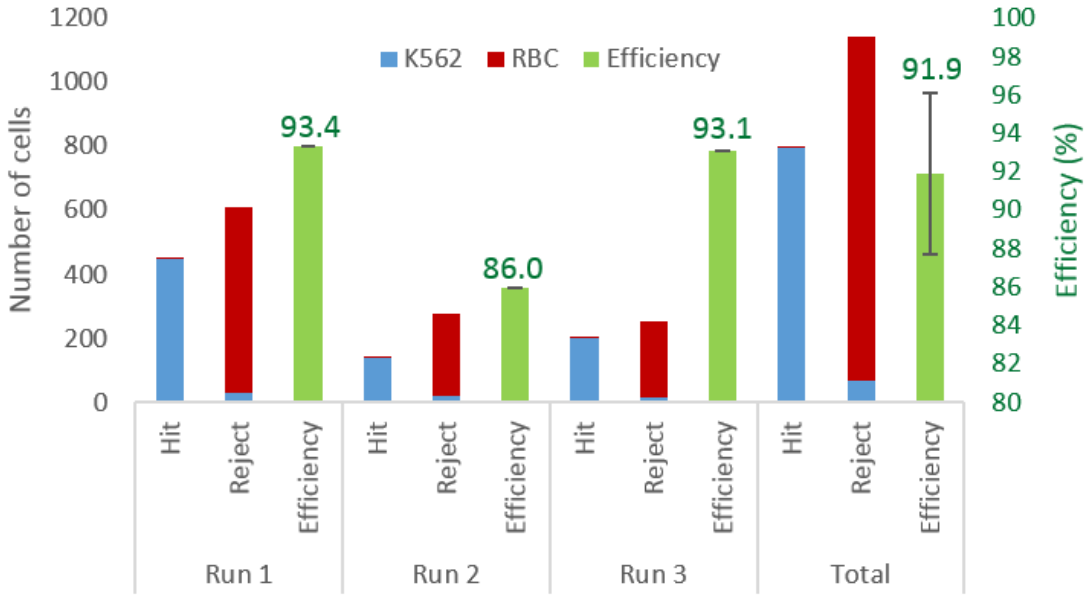

Figure 4.10 *Number of K562 cells (blue) and RBCs (red) characterised into the hit (K562 target cell) and waste (RBC non-target cell) categories. As expected there are a fraction of smaller K562 cells which are determined to be waste and the efficiency of the K562 detection is plotted for each run (green). There are a small number of RBCs in the hit category but this number is kept to a minimal by optimising the area threshold.*

4.5 Sorting synchronisation using the trigger camera

Once a cell has been imaged and a decision on its class made, it must be sorted into the correct outlet. The waste outlet channel is slightly larger than that of the sorting channel and so, by balancing the outlet vials, the flow of the cells defaults into the waste channel unless acted upon by an external force. To move a cell into the waste outlet the piezo must controllably fire. If the cell is at the correct position within the sorting channel at the time of piezo fire, it will follow a temporary trajectory into the sorting channel and will be successfully sorted. However, if the cell is not far enough along the sorting channel by the time the piezo fires, the trajectory may have corrected back to the initial path down the waste outlet. Alternatively, if the cell is too far down the sorting channel it may not be affected by the liquid displacement and will again continue down the waste outlet. It is therefore important to fire the piezo when the cell is in the correct position within the sorting channel.

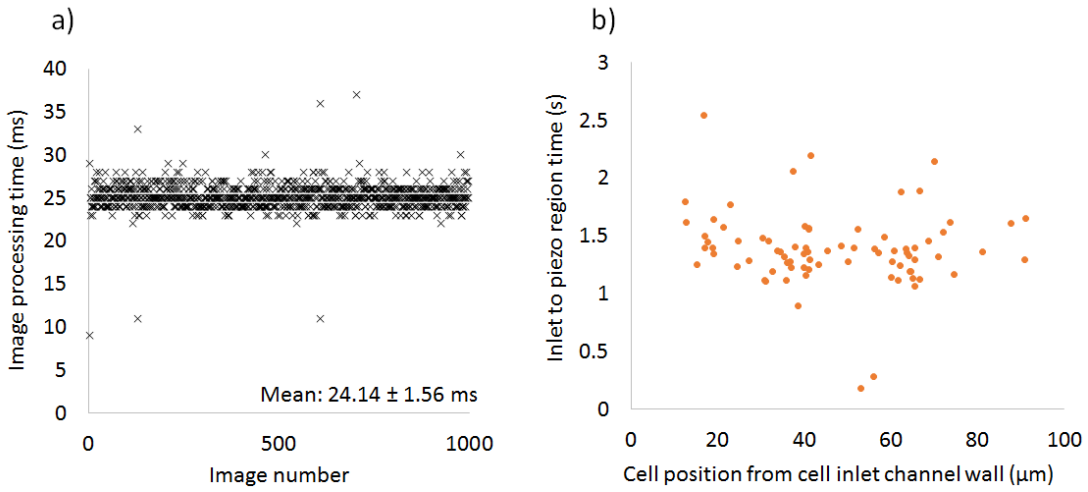

Figure 4.11 (a) *Time taken for decision making software to take in an image and provide a decision for 1000 images.* **(b)** *The movement of a number of cells within the microfluidic device was observed and the time taken for the cells to move from the cell inlet region to the sorting region was recorded. The average time taken is 1.4 ± 0.3 seconds with a range of 2.4 seconds. The journey time is independent of the initial position within the cell inlet channel wall.*

It was hoped that the cells could be imaged by the cell imaging camera, with the piezo being fired after a set amount of time. A test sort was performed where K562 cells were imaged and the piezo was fired after 1.4 seconds (the average time for a cell to reach the piezo region from the imaging region). The sorting was ineffective and only managed to move 53% of the cells.

Several factors can interfere with this synchronisation: the image processing is performed on a computer and depending on the complexity of the shapes in the image (and the computer background processes) it may take varying lengths of time to make a decision. The cell imaging has to be carried out before the flow focus to reduce motion blur and so there is a length of channel the cell is required to move before the piezo can fire. The flow rate can also change; either randomly, or by the user changing the velocity of the flow. The flow will also not be constant across the channel due to the laminar flow profile. The imaging area is finite, so a cell captured at the "top" of the image has a shorter distance to travel than one in the "bottom". All of these factor together meaning that we need a way to synchronise the piezo to the moment when the cell is in the right place.

To test the cell classification jitter, 1000 images were classified and the time taken for each classification was plotted in **Figure 4.11a**. The mean processing time was 24.14 ± 1.56 ms, with a range of 28 ms. To investigate the variation in the cell journey time within the microfluidic channel, the time taken for 80 cells to reach the sorting region

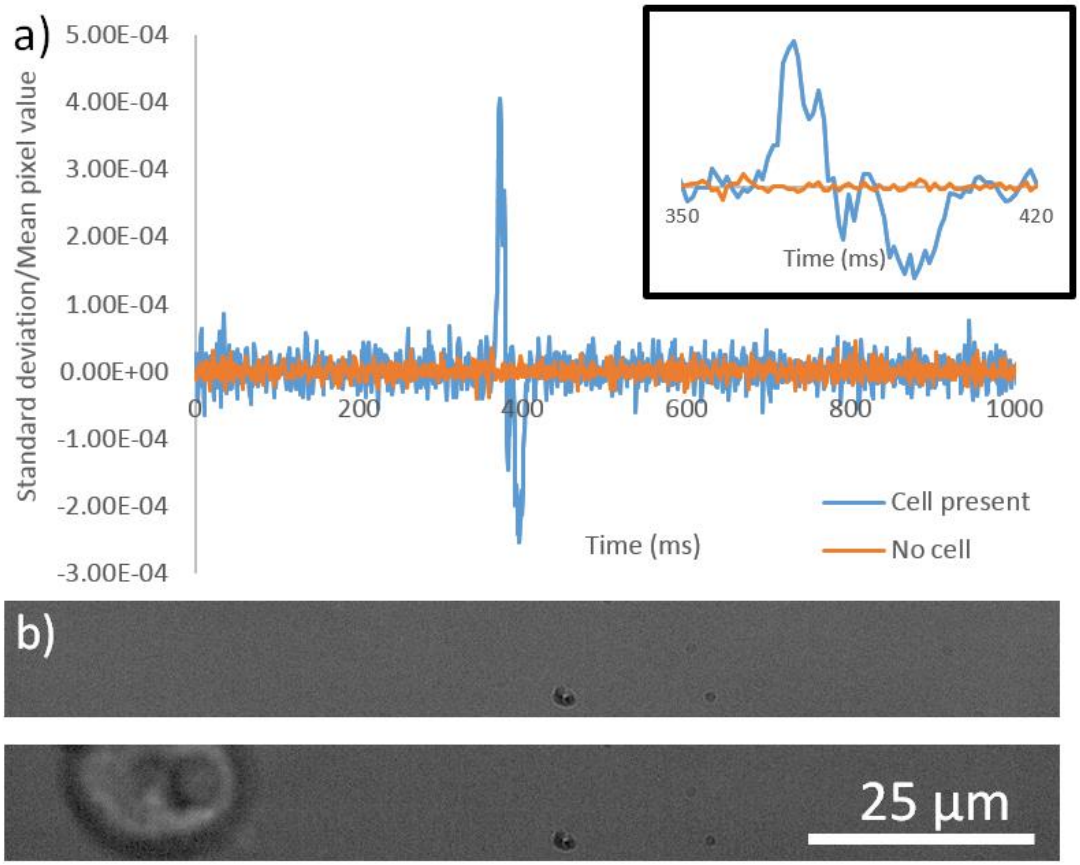

Figure 4.12 (a) *Signals of the standard deviation/mean of the images taken in the case of a cell being present and no cell. The peak in the signal where the cell is present is above the threshold of* $2x10^{-4}$ *and so will alert the software.* **(b)** *Images taken from the trigger camera with no cell and with a cell.*

from when they are first imaged, by the cell imaging camera, was recorded. As shown in **Figure 4.11b**, the mean journey time was roughly 1.4 seconds but there was significant variation of 2.4 seconds, which is a factor of 100 times greater than the jitter in the classification software. The variation was also independent of the initial cell position within the cell inlet channel and recordings taken by the wide field camera highlighted that in the cases where cells were not sorted, there were instances of the piezo firing both too early and too late. As the cell journey time is inconsistent, the cell position at the sorting region must be confirmed and so a third camera was added, the trigger camera.

The trigger camera images the start of the sorting region, see **Figure 4.2**. Its purpose is to detect the presence of a cell and to advise the piezo when to fire. The images taken are wide enough to cover the full width of the sorting channel but the height of the image is reduced to allow for faster frame times, 1000 fps. With a combined flow rate of 20.4 µL/hr, the cells travel in the 30 x 112.5 µm channel with a velocity of 1.26 mm/s. For an RBC with a diameter of 6 µm and a K562 cell with a diameter of 20 µm this leads

to 12 and 23 images being taken of each cell respectively; which is the same order of magnitude as the number of points on the insert graph in **Figure 4.12a** which appear above the noise, 40. This allows the cell to be accurately detected, but if throughput is increased, this may become a limiting factor.

To detect a cell within the image, the standard deviation over the mean of all pixels is calculated for each image. If this value of an image is over a threshold then a cell is detected. Images taken by this camera both with and without cells and the resulting values of standard deviation / mean pixel values can be seen in the images in **Figure 4.12**. The threshold value for detection is $2x10^{-4}$. This improved the accuracy of the cell sorting which will be discussed in the following sections.

4.7 Optimising amplitude and timing of piezo fire

The movement of the piezo is controlled by a data acquisition device (National Instruments USB 6002 DAQ) which provides the piezo with a voltage between - 10V and 10V; this signal can be sent to the DAQ for a designated length of time. The piezo is initially given a signal of -nV (where n is a predetermined value) causing the piezo to bend away from the reservoir. When a cell is detected the piezo is given a signal of +nV and will bend towards the reservoir, forcing a displacement of liquid into the sorting channel. This results in the cell solution trajectory moving into the sorting outlet at the far side of the piezo channel.

To provide the most effective sort, the magnitude and length of the signal must be optimised. Piezo voltages from 1V to 10V, in increments of 1V, and piezo on times from 0.05 ms to 0.5 ms in varying increments were tested in different sorting runs, resulting in 80 combinations of voltages and on times. The videos taken, showing the movement of cells and the outlet they left the device in, were manually analysed to determine the sorting success of the sort. As would be expected, for low voltages, the resulting piezo movement was too weak to displace enough liquid flow and, although some movement was observed, the trajectory of the cell solution did not move into the sorting channel (**Figure 4.13a**). In other cases, the piezo movement was too aggressive and the trajectory moved into the buffer zone, taking the cell with it (**Figure 4.13c**). Finally, there were a number of combinations which resulted in the trajectory moving into the sorting outlet for a short period of time, before moving back to the waste outlet, as the piezo relaxes back to its neutral position (**Figure 4.13b**).

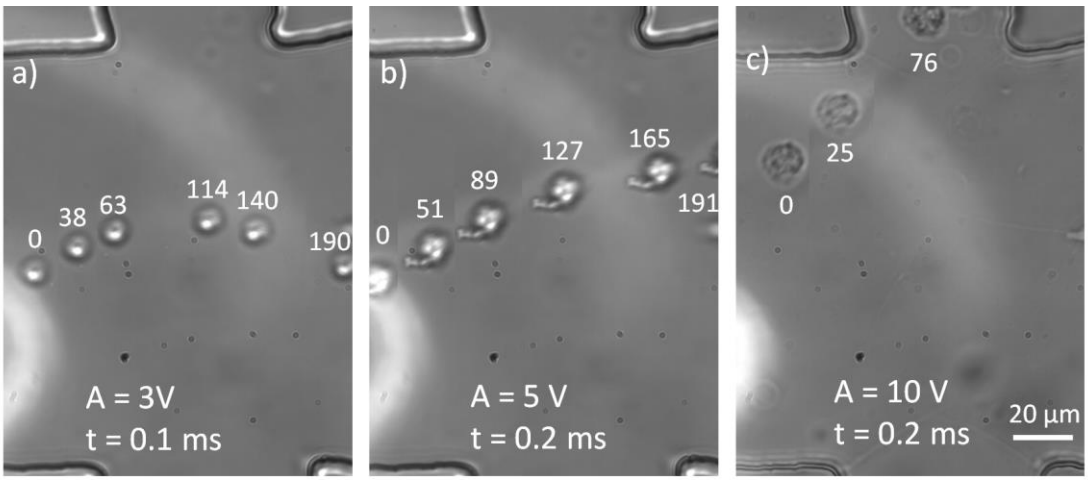

Figure 4.13 *Images showing a single cell trajectory during the firing of the piezo. The amplitude and length of time of the signal sent to the piezo, and the time point of each cell position can be found on the images* **(a)** *Cell movement when the piezo pulse is too weak to move the cell into the sorting outlet.* **(b)** *Cell movement when the piezo pulse is optimised to move the cell into the sorting outlet.* **(c)** *Cell movement when the piezo pulse is to large and the cell is forced into the buffer zone. The numbers above and below the cells represent the time point at which they were imaged in milliseconds.*

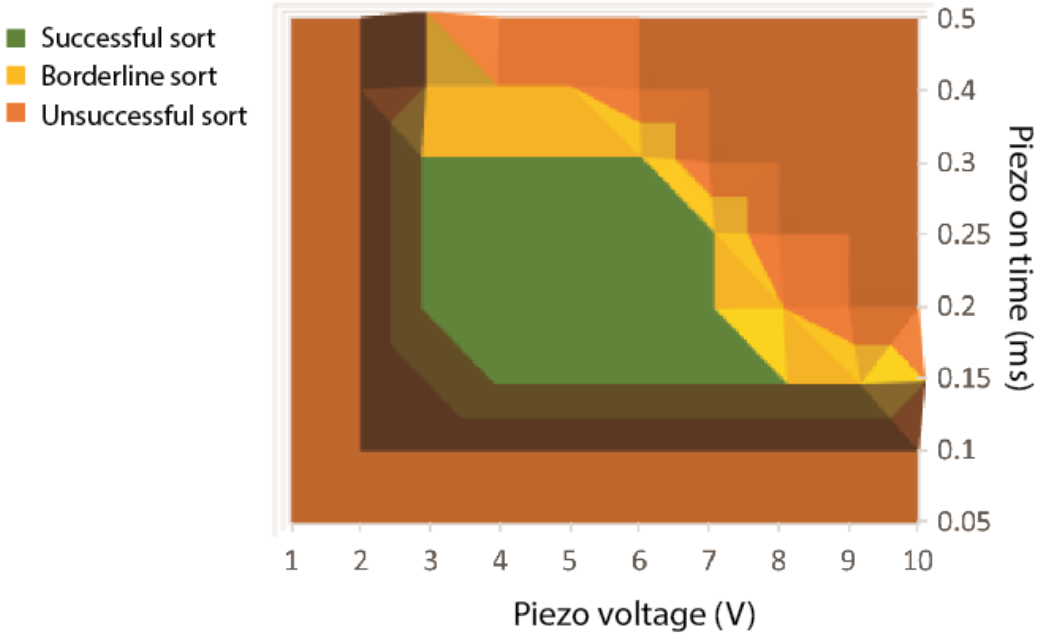

Figure 4.14 *Heat map with the success of various combinations of piezo voltages and piezo on times. Successful sorts are represented with green, unsuccessful sorts with red and borderline sorts with yellow.*

Figure 4.15 *Using the optimised piezo firing values of 4V and 2.5 ms, three runs were carried out with K562 cells (the target cell) and RBC cells being sent to waste. The combined sorting efficiency of the piezo was measured to be 98.4%.*

The results of each combination can be visualised in **Figure 4.14**, where the green, yellow and red colours show if each magnitude and on time combination result in: a successful sort, a borderline sort (where most of the cells are sorted but not all) and an unsuccessful sort respectively. For the final experiments the piezo voltage and on time was set to 4V and 2.5 ms respectively.

4.8 Success of piezo actuation

With the piezo timing and fire signal optimised, tests were performed to measure the efficiency of the sorting. RBCs and K562 cells were passed through the device and the aim was to separate the K562 cells, which were the target cells to be sorted; from the RBCs, which should go to waste. Images were taken of each cell and the decision making software discussed in **Section 4.4** categorised each cell as a hit (K562) or a rejection (RBC). The cell will then flow into the sorting region and be detected by the trigger camera.

If the cell is a hit, the piezo will be fired. If the cell should be rejected, the piezo will not fire and the trigger camera will then wait for the next cell to be detected by the cell imaging camera. The wide field camera can then be used to determine if each cell has been sorted into the required outlet. See examples of a hit event, a K562 cell being sorted; and a reject event, an RBC being rejected, in **Figure 4.16a** and **Figure 4.16b**

respectively. When the videos of the cell trajectories were analysed, the sorting efficiency was found to be much improved. **Figure 4.15** shows the fraction of cells which were sorted, when the piezo fired, for each of the three runs. The combined sorting efficiency of the piezo was 98.4%. No rejected cells were found to have been missorted into the sorting outlet. This analysis did not take into account whether the cells being sorted and rejected were K562 cells or RBCs, only if the event was a hit or rejection.

4.9 RBC and K562 cell sorting success

The final analysis of the sorting experiments was to quantify the efficiency and purity of the cell sorter, taking into account the imaging, the decision making and the piezo sort. To obtain this information each cell was imaged and given a number which corresponded to a trajectory video. This way the cell type could be manually characterised post-experiment and the outlet, which the cell was sorted to, recorded. This provides a more accurate representation of the success of the sorter.

Figure 4.16d shows the fraction of K562 cells and RBCs which were sorted for all three runs. The desired outcome was for all K562 cells to be sorted and no RBCs to be sorted. Over the three runs, there were 726 K562 cells and 943 RBCs measured. Of these cells, 663 K562 cells and 4 RBCs were found to have been sorted into the sorting outlet, while the remaining 63 K562 cells and 939 RBCs ended up in the waste outlet. This equates to 91.3% of K562s and 99.6% of RBCs ending up in the correct outlet.

In the field of cell sorting it is common to determine the success of a method by the efficiency and purity of the final sorted sample, especially when isolating rare samples[266]. The efficiency and purity of the system is calculated using the below equations.

$$Efficiency = \frac{Number\ of\ K562\ cells\ in\ outlet}{Number\ of\ imaged\ K562\ cells} \quad \textbf{(4.1)}$$

$$Purity = \frac{Number\ of\ K562\ cells\ in\ outlet}{Total\ number\ of\ cells\ in\ outlet} \quad \textbf{(4.2)}$$

Efficiency is the proportion of the total K562 cell population which has been sorted and the purity is the proportion of cells found in the sorting outlet which are K562 cells. The efficiency of the system was found to be 91.3% and the purity of the system is 99.4% (**Figure 4.16c**). This is comparable with results found in the first image based cell

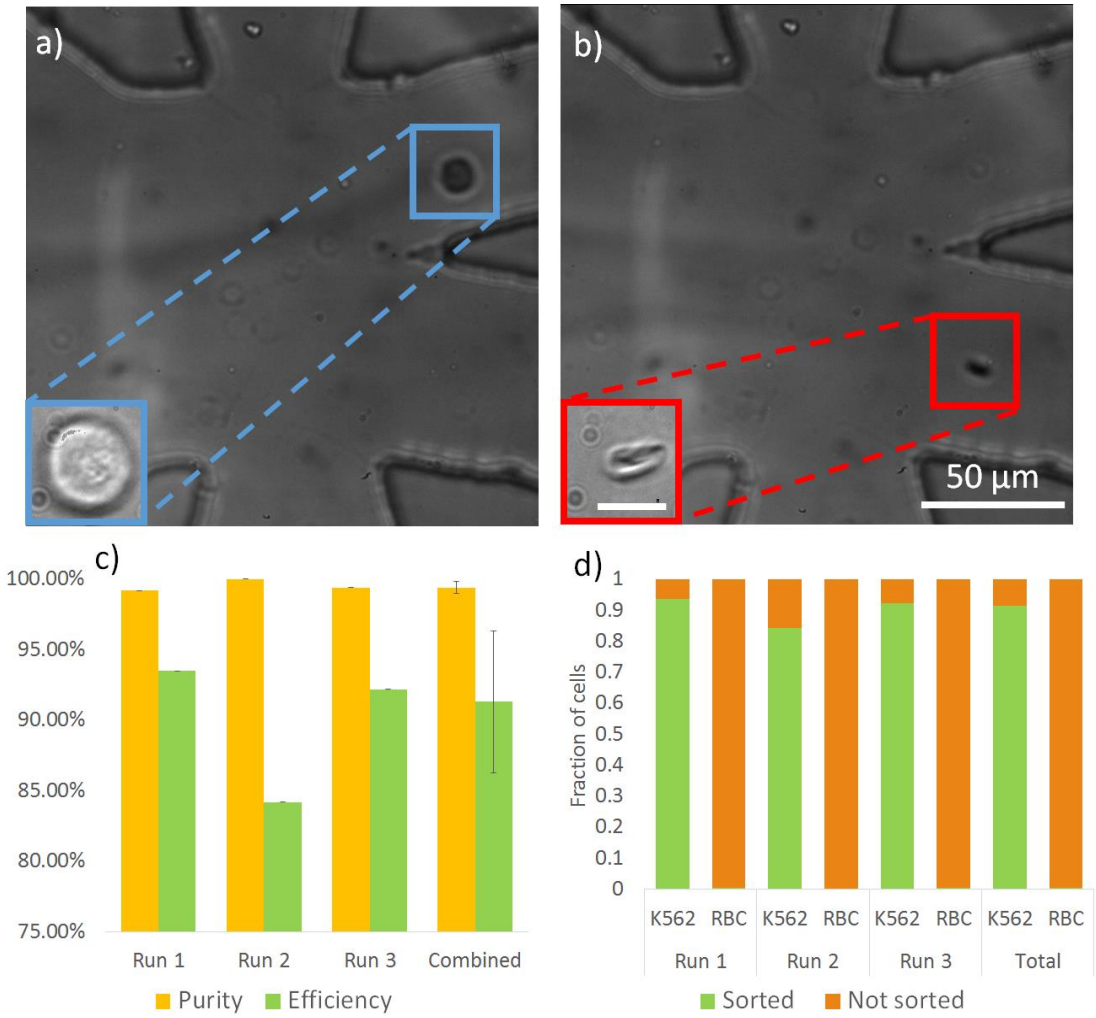

Figure 4.16 *Micrographs of the cell sorting region take by the wide field camera showing* **(a)** *a K562 cell (blue) being sorted and* **(b)** *an RBC (red) continuing into the waste channel. The smaller cell images within the coloured squares are the corresponding images of the cells taken via the cell imaging camera. The scale bar for the insets is 10 µm.* **(c)** *The final purity and efficiency of the system. The combined efficiency of the three runs is 91.3% while the combined purity is 99.4%. (d) The final outlet location for over 1500 cell events.*

sorting paper published in 2018 which provided purities of 99% and efficiencies between 67.7% and 82.0%[35]. The throughput of the system is currently at 0.21 Hz. This is not as fast as other current methods (>100Hz)[35], but the larger efficiency in the sorting may be attractive for smaller, precious and rare cell samples.

4.10 Conclusion

By combining image-based decision making and a piezoelectronic sorting technique, it is possible to separate different cell types (K562 cells from RBCs), using bright field imaging, with high efficiency and purity. The three independent parts of the sorting technique; imaging, decision making and sorting, work well both independently and when combined. The decision making software is useful in identifying 91.9% of the K562 cells, while accurately characterising 99.4% of the RBCs. The thresholds in the software prioritise purity over efficiency. The movement of the piezo has been optimised to ensure target cells are smoothly directed into the sorting outlet, while unwanted cells successfully continue into the waste outlet. The three camera setup allows the cells to be accurately identified and located throughout their entire journey in the sorting channel. Three test runs were performed to determine the effectiveness of the cell sorting, with 1941 cells processed. K562 cells were targeted and sorted with an efficiency of 91.3% and the sorting outlet channel had a purity of 99.4%. These results highlight that high levels of efficiency can be achieved, even when purity is prioritised. This chapter allowed for the calibration of the piezo and three camera system. **Chapter 5** improves on the method used in this chapter, by adding a fluorescent based imaging system and improved machine learning software.

Chapter 5. Fluorescent nuclear image-based sorting

The work in this chapter extends the work carried out in previous chapters, with the heterogeneity of sub-cellular structures (cell nuclei) investigated, compared to the external cellular morphologies discussed in **Chapter 4**. The microscope setup was updated to allow for fluorescence-based imaging and the real-time classification algorithm was modified to extract quantitative features from the image and to use machine learning to classify the cell type. The use of fluorescent imaging opens up a wide range of new cell types which can be identified, sorted and analysed. Cells with differences in their internal cell structure can be split into subpopulations and the function of these differences further understood.

The SAFH fibroblast cells were provided by Nattaphong Rattanavirotkul (University of Edinburgh) and the hepatocytes were provided by Jordan Portman (University of Edinburgh). These samples were provided live and were used in the devices with no further preparation. A population of Jurkat cells were provided by Ewa Guzniczak (Heriot Watt University) which were grown and cultured using the techniques described in **Section 2.3.2**.

5.1 Overview

The ability to investigate how differences in the internal morphologies of cells affect cell function is of great interest to cell biologists[248]. Previous methods (described in **Section 1.4**) only measure one dimensional measurements such as total fluorescent intensity; but this has its limitations, leaving cells with different internal morphologies (but similar fluorescent intensities) inseparable[42]. These differences can be observed using imaging cytometry but only recently has this imaging technique been merged with cell sorting[35,267]. As described in **Section 4.1** the IACS technique is costly and complex[262] to implement, limiting its potential adoption. In this chapter a more widely applicable cell sorting technique is presented which allows for fluorescent imaging and subcellular morphology classification.

This work focuses on investigating nuclear morphological differences between cells of the same cell type, using fluorescent markers similar to those described in **Section 1.5**. This allows images of the nuclei to be taken, which can be analysed and classified into subpopulations. Due to the subtleties of some of the morphological differences, the previous classification method of using a single measurement as a threshold does not work. To improve this, the images of the cells are segmented and analysed to extract 25 measurements. Machine learning algorithms are then used to analyse these measurements to predict the most likely cell subpopulation the image belongs to. The algorithm was tested on a number of cell models and could predict the correct cell types with high levels of efficiency and purity. By implementing the algorithm into the cell sorting software, cells can be imaged, classified and sorted in real time, within the microfluidic device as the cells flow through the device.

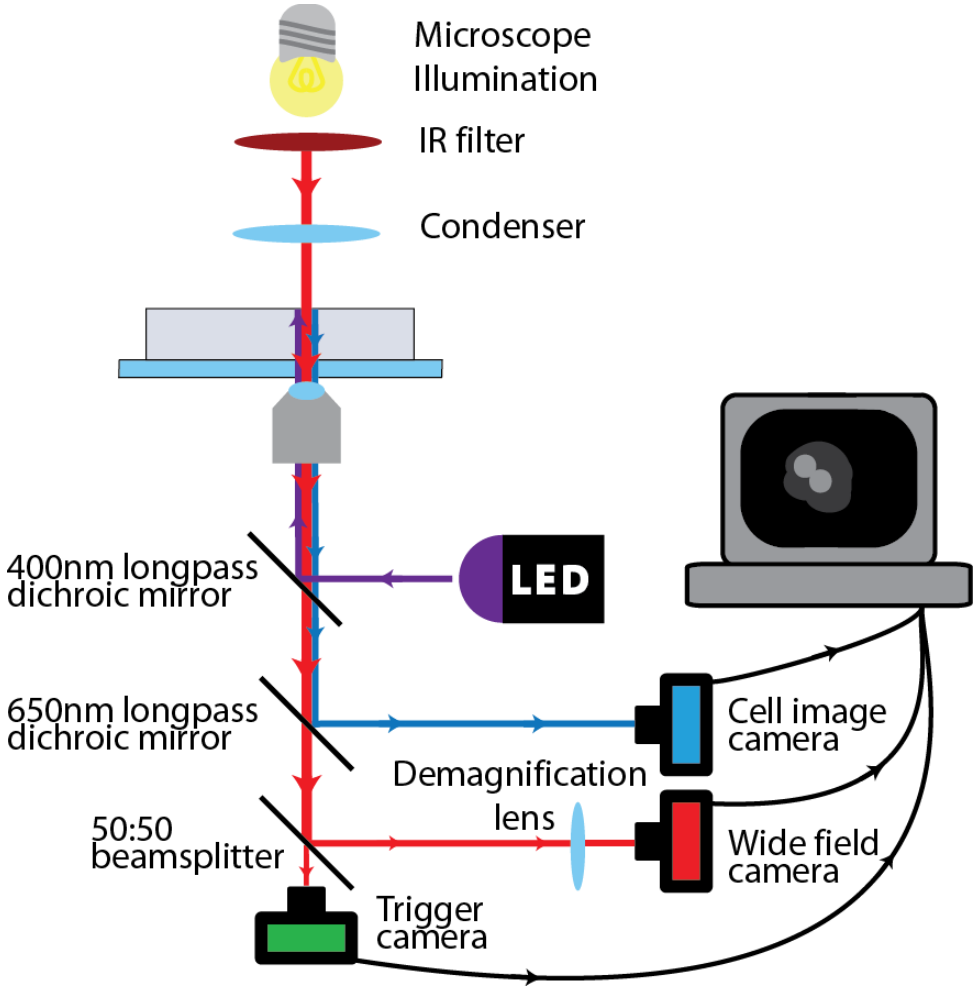

Figure 5.1 *Schematic diagram showing the setup used for fluorescent image based cell sorting. A microscope is used to illuminate and image the cells within the microfluidic channels. A 365 nm LED is used to illuminate the fluorescent dye within the cell nuclei and this light is directed into the cell imaging camera (blue). The filtered infrared (IR) light from the microscope illumination is split between the trigger camera (green) and the wide field camera (red).*

5.2 Experimental setup

To image, analyse and sort cells based on their fluorescing nuclear morphology, a modified setup of the previous chapter's cell sorting setup was used (see **Figure 5.1**). The main change in the system is the ability to excite fluorescence within the passing cells and to image the emitted light using one of the three cameras used previously. The cells themselves, are stained with Hoechst 33342 stain (using the methods described in **Section 2.3.6**) which causes the DNA within the cell, and hence the nucleus, to fluoresce. To excite the Hoechst stain within the cells, a 365 nm LED is directed into the back aperture of the objective lens (via a 400 nm longpass dichroic mirror) which focuses onto the microfluidic device. The emitted 497 nm fluorescence from the cells is then reflected by the 650 nm longpass dichroic mirror and detected by the cell imaging camera,

previously used for imaging the RBCs and K562s in the brightfield in **Chapter 4**. To allow for brightfield imaging of the cells and to monitor the device during the sorting (without overexposing the fluorescent images) an infrared (IR) 700 nm filter is used on the microscope's halogen light source to block most visible wavelengths. The IR light transmitted through the sample is directed away from the cell imaging camera by transmission through the 650 nm longpass dichroic mirror. A 50:50 beamsplitter then splits the light equally onto the trigger and widefield cameras, allowing cell movement and position to be observed.

The microfluidic devices used to sort the cells are the same as in **Chapter4** and the method of cell injection remains the same. There are a number of different cell models used in the experiments described in this chapter, and so the cell solutions used will compromise of 33% OptiPrep and 66% cell solution; containing the two cell types, suspended in PBS and 1% pluronic.

5.3 Imaging the four cell models

There are four different cell models which have been investigated in this work, images of which can be found in **Figure 5.2**. The four models are: (A) fibroblast SAHF positive cells which contain 'spotty' nuclei vs SAHF negative cells, which contain 'smooth' nuclei **(Section 1.7.1),** (B) healthy vs apoptotic K562 cells (**Section 1.7.2**), (C) Jurkat vs K562 cells and (D) mono vs bi-nucleated hepatocyte cells **(Section 1.7.3)**. Models A, B and D are found in mixed populations, while the remaining model C is a manually mixed solution which acts as a proof of concept. Both Jurkat and K562 cells are a form of leukaemia and so are similar cell types. With this mixed population it is easy to control the concentration of each cell type.

In the previous chapter, the software was able to determine the cell type by measuring the total area of the cell, with RBCs being noticeably smaller than the larger K562 cells. However, the nuclear morphological differences in the four cell models are much more complex; with differences in the number, shape and internal structure of the nuclei needing to be observed. To investigate these differences, a library of images of each cell model and cell type (within each model) was obtained. For models A, B and D, the mixed solutions were injected into a microfluidic device and cytometrically flown past the cell imaging camera. This allowed hundreds or thousands of images of both cell types in each of the three models to be obtained. As lighting conditions and the focus of the images can change from experiment to experiment, at least three imaging cytometry

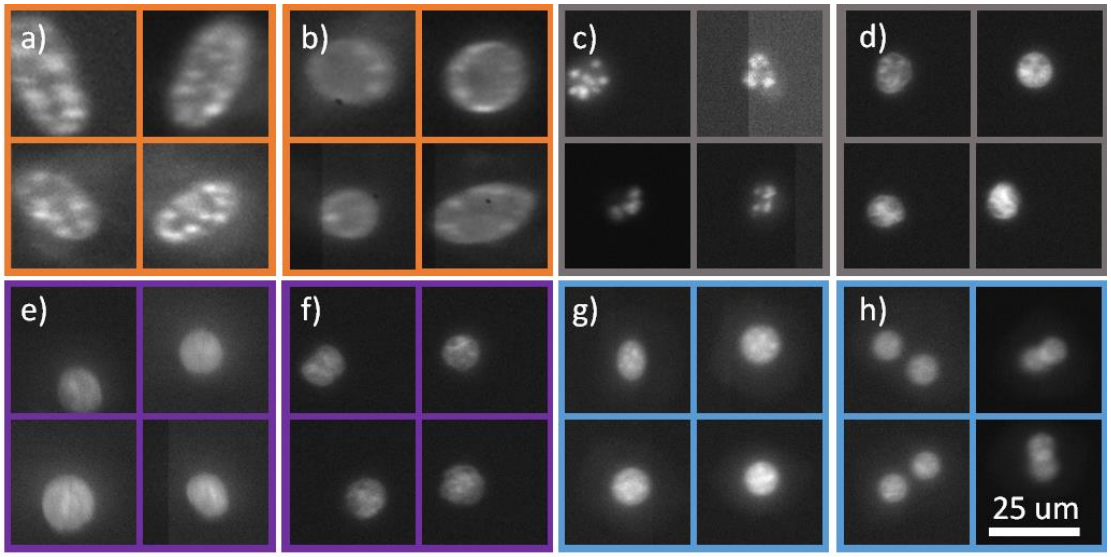

Figure 5.2 *Images of the nuclei of the four cell models (each with two cell types) used in this chapter;* **(a)** *SAHF positive and* **(b)** *SAHF negative fibroblasts (orange),* **(c)** *apoptotic and* **(d)** *healthy K562 cells (grey),* **(e)** *Jurkat and* **(f)** *K562 cells (purple), and* **(g)** *mononucleated and* **(h)** *binucleated mouse hepatocyte cells.*

runs were performed to provide the machine learning software (LabVIEW Analytics and Machine Learning Toolkit) with a more robust data set. Images of the four cell models can be found in **Figure 5.2**.

To accurately train the machine learning to identify the correct subpopulation, the obtained images were manually classified and used as a supervised training set. The cells from the third model (C), Jurkat vs K562, are cultured separately and therefore could be passed through the device and imaged individually, resulting in two preclassified data sets. Once the images were obtained and classified it was possible to train the machine learning algorithm. Cell models A, B and C all contain one nucleus, while cells found in cell model D may contain multiple nuclei. This means a machine learning algorithm for cell model D must be more complex and so the machine learning discussed in the following subsection only applies to cell models A, B and C.

5.4 Training of the machine learning algorithm

Similarly to how the RBCs and K562s were identified within the images in **Chapter 4**, the nuclei of each cell present in the image must be detected. As only the fluorescent blue light is incident on the camera, the microfluidic channel in the background of the image is dark and so a simple intensity threshold can be used to remove the background, providing a processed secondary image which is used to locate the bright particles present in the image. The thresholds used are preset fractions of the maximum

intensity in the image, 60%, 70% and 80%. This is done using National Instruments Vision software.

For cell models A, B and C, it is important that only one nucleus and therefore one cell is present in the image. If multiple cells or a cluster of cells is present, non-target cells may be sorted into the outlet at once, leading to contaminations in the post-sort populations. This may be missed if the fluorescent signal of the two nuclei are of varying intensities; as a threshold may remove both the background and the less intense nuclei, leaving only one nuclei to be further analysed. To ensure that any cases of multiple nuclei are recognised, three values for the threshold are used to remove the background from each image and the number of particles present in each case is calculated. This helps locate darker nuclei which may have previously been removed by the software, an example of which can be found in the flow diagram in **Figure 5.3**. The threshold which results in the highest number of detected particles is then selected, to ensure all nuclei are detected.

Although undetected nuclei would be a problem, detecting false nuclei could also give rise to potential miscalculations. If there is debris in the microfluidic channel or individual pixels outwith the nucleus that are above the threshold, then it is important that these are not incorrectly identified as particles or nuclei. As these particles are smaller, a particle size threshold is used to remove smaller particles in the image. This erases the extra particles from the image so they will not be included in nuclei detection calculations, this can be seen in the blue section of the flow diagram in **Figure 5.3**; where individual pixels and smaller clusters of pixels are detected and removed, leaving only the larger particles of the nuclei.

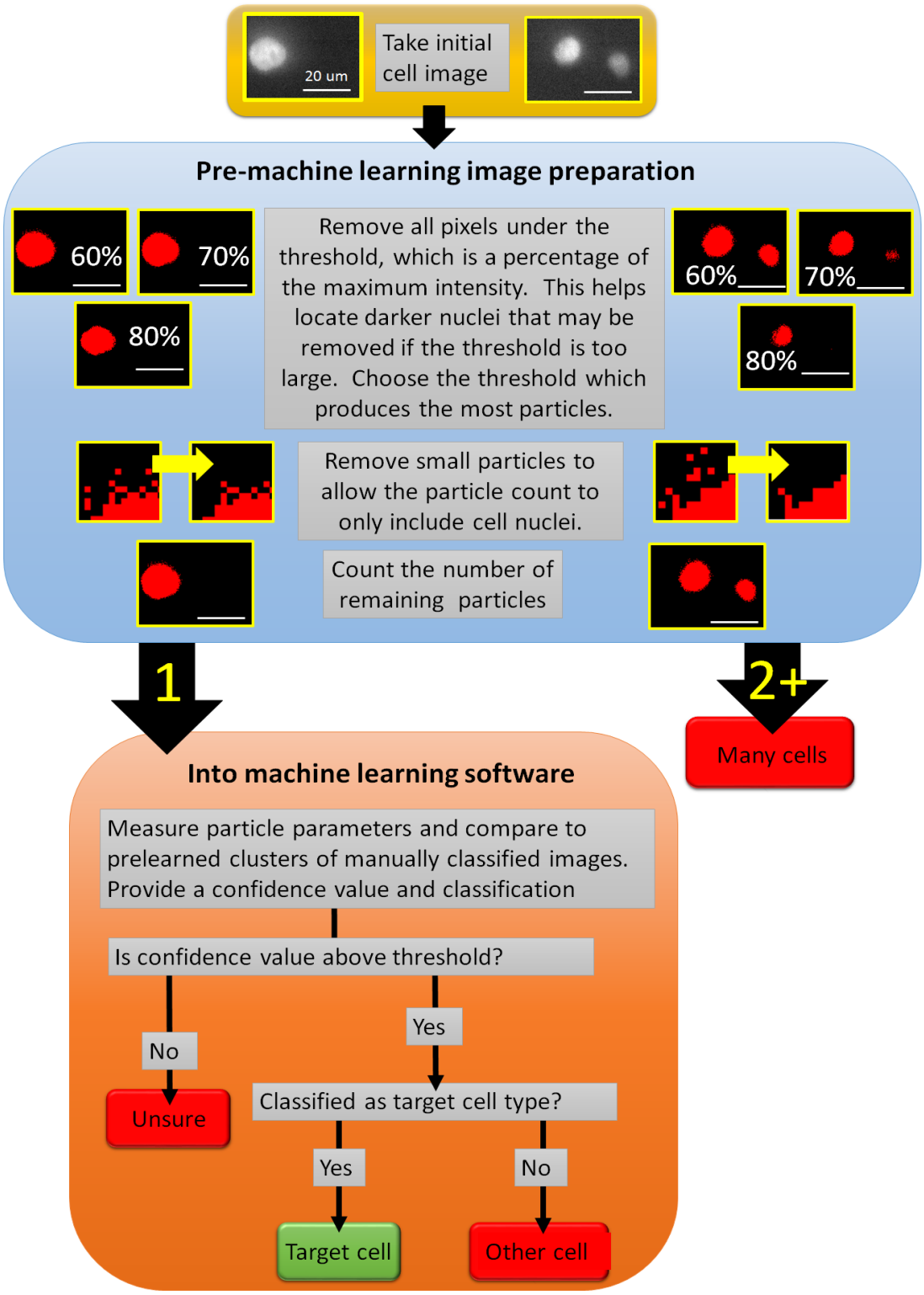

Figure 5.3 *Flow diagram of the machine learning process. The cell images go through a pre-classification process; three intensity thresholds are used to locate all nuclei within the image. Small particles are then removed from the image. The number of remaining nuclei is then counted. If the image has two or more nuclei, it is classed as a multi cell image. If the image has only one nucleus it will enter the machine learning stage. 25 measurement parameters are taken for the particle and these are compared to those of manually classified images. The image is classified as the target cell or the non-target cell and given a confidence value. If this value is below the pre-set threshold it will be classed as in image that the software is unsure of. If the image is above the threshold, it will be given its final classification. All scale bars are 20 µm.*

Once the image processing is complete, the number of particles within the image is counted. If more than one particle is present, the image is classified as containing multiple cells. If only one particle is present, the image is further analysed by extracting 25 measurement parameters (all 25 measurement parameters can be found in **Section 2.3.9**). The measurement for each parameter gives a location within the 25 dimensional space. Every image with a single cell therefore has a position in this 25-dimensional space which is used, together with the manually defined classification, by the machine learning software to characterise the clusters which correspond to each class.

Once the machine learning has built up a model of how the measurements can relate to the classification, new unclassified images can be classified by following the same image preparation as described previously. If the image contains a single particle, measurements are taken and it is given a position in the 25-dimentional graph. The machine learning algorithm can classify new images by comparing their 25-dimensional position to that of the predetermined clusters of images. It determines the likelihood that the cell in the new image belongs to a particular cell type; by giving each cell image a "confidence value" (between 0 and 1) for both cell types. The largest of the two confidence values is attributed to the cell image and the cell is characterised as that particular cell class. The machine learning uses this process to class all new cell images as one of the predefined cell types.

To improve the purity, the confidence value can also be used in order to remove classifications which are less certain by adding a threshold to allow for higher purities; with only cells similar to those previously classified (with high confidence values) being considered, while those under the threshold are classified as unknown and can be sent to waste. Cells that provide a confidence value over the threshold can then be accepted or rejected, depending on the target cell type. This process is illustrated in the orange box in the flow diagram in **Figure 5.3**.

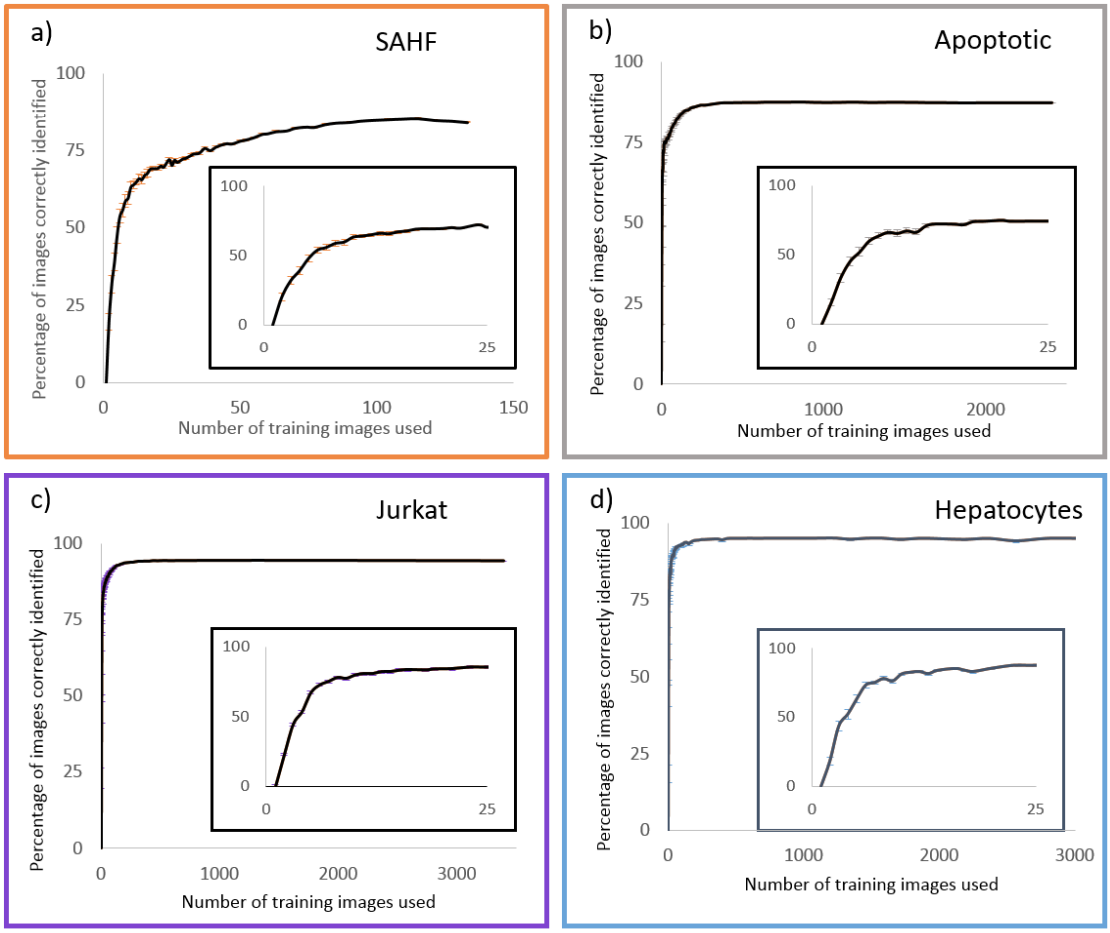

Figure 5.4 *Graphs showing the classification success of the machine learning algorithm, when trained with different numbers of randomly selected training images, for the four different cell models. The inset graphs highlight how the algorithm performs with lower numbers of initial images. All measurements were repeated 100 times and the coloured error bars represent the standard error. Note: the hepatocyte model was only training and classifying single particle images, therefore mononucleated hepatocytes.*

Intuition suggests that the greater the number of manually classified images initially used to train software, the more accurate it will be at classifying new images. To test this theory, the software was trained numerous times with different numbers of randomly selected, manually classified, images. The whole library of manually classified images for the cell model was then fed into the machine learning software and the results compared to the original manual classification to determine the fraction of correctly classified images. This was repeated 100 times for all four cell models and the mean values can be found on resulting graphs in **Figure 5.4**. These measurements are based on classifying each image to the highest class without using the confidence value threshold.

Cell models A, B and C are as expected but due to the multiple nuclei present in the binucleated hepatocyte cells, only the images containing one particle (mononucleated

hepatocytes) were classified for this graph; this will be discussed more **in Section 5.6** and for the remainder of this section only cell models A, B and C will be discussed.

The number of images of cell model A (133) taken compared to B (2408) and C (3390) is comparatively low, but in all three cases the fraction of cells correctly identified seems to be tending towards an asymptote. This value is the best possible outcome that the software can provide, even with an infinite number of preclassified initial cell images. For each cell model, the value of this asymptote and the number of images needed to reach it can be obtained from the graphs. For cell model A, the software can classify new cell images 84.0 ± 1.5% of the time (where the error is the standard deviation) and it only needs 90 images to reach this performance. For cell model B, with a sufficient number of initial images the software is correct 87.4 ± 0.1% of the time; and it only needs 500 images to reach this value, although it reaches 85.0 ± 1.4% with only 150 images. The software provides the best results for cell model C, with the maximum success rate reaching 94.2 ± 0.1%, with the graph levelling off at about 300 initial images. With the graphs of all three cell models levelling off before the total number of images, this shows that the software is currently optimised and more images would improve the machine learning classification very little, if at all. Based on this analysis, the maximum possible purities for all three cell classes would be under 95% which is less than ideal.

The confidence value threshold can be used to further improve the system. To understand how it effects the purity and efficiency of the classification and to quantify its success when compared to other methods, ROC curves were used.

5.5 Characterising the success of the machine learning software

To test the machine learning's ability to identify the correct cell type, ROC curves were plotted for the four different cell classes and can be found **in Figure 5.5** (again the graph for cell class D was obtained using only the images containing one particle). The coloured dots represent the results from the machine learning software, while the solid black lines represent an alternative method of using the most indicative of the 25 aforementioned particle measurements as a threshold. The most indicative value is the measurement which separates the two cell types most successfully. The generation of the solid lines on the ROC curves is done using the same method used in **Section 2.3.9**, when RBCs and K562s were separated using a single measurement of the cell area. The measurements used for cell models A, B, C and D were; bounding rectangle width, waddle disk diameter, compactness factor and again compactness factor respectively.

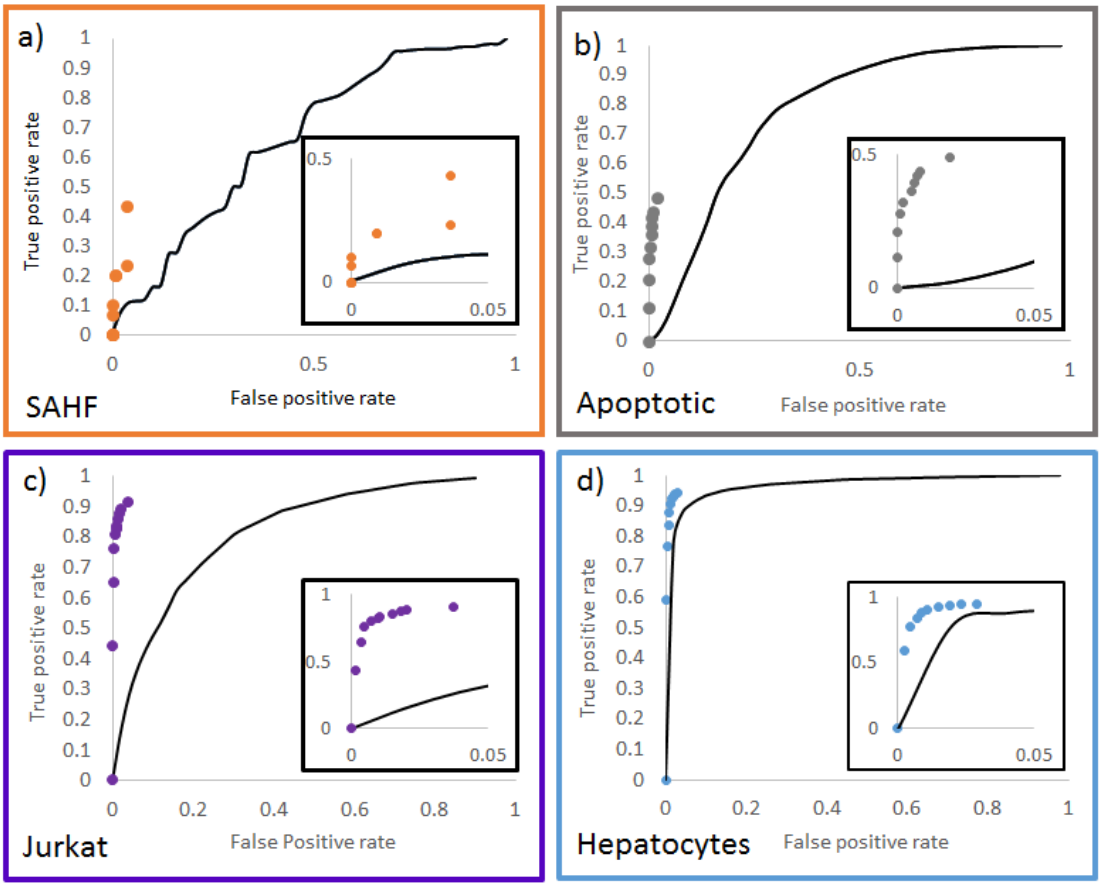

Figure 5.5 *ROC curves generated for the four cell models. The filled black lines represent how the false and true positive values change as the confidence value threshold is changed. The coloured dots show the true and false positive values produced when various thresholds are applied to the machine learning algorithm. As the machine learning technique does not produce values with high false positive rates, the inserts show the performance of both classification techniques at low false positive values.*

To generate the coloured points on the graph, thousands of manually preclassified images of each cell model were passed into the machine learning software and if the confidence value of an image was below the threshold, the image was classified as 'unsure'; if the confidence value of an image was above the threshold it was characterised as the target cell or non-target cell discussed before. This was repeated for eleven different confidence values (from 0 to 1, in increments of 0.1).

SAHF positive fibroblasts, apoptotic K562 cells, Jurkat cells and mononucleated hepatocytes were chosen as the target cells for each of the four cell models. The true positive value was defined as the fraction of manually classified target images which were correctly identified. The false positive value was defined as the fraction of non-target cell images which were classified as target cell images.

As can be seen in **Figure 5.5**, in all four graphs the machine learning values do not reach the top right side of the plot, as the curves for the single measurement threshold

do. In the case of a single measurement being used as a threshold, the initial graph used to make the ROC curve contains two overlapping bell shaped curves due to their Gaussian like distributions (as seen in **Section 2.3.9**). When the threshold line reaches the edges of the bell curves, both the true positive and true negative values will either be 0 (where everything is sent to waste), or 1 (where everything will be sorted). This means the whole curve will start at the bottom left of the graph and will move to the top right, but this is not the case when the machine learning results are plotted. As the confidence value threshold does not change the outcome of the machine learning classification, it is unlikely that all of the images are classified by the machine learning software as the target cell type. This means that the true and false positive values are unlikely to reach a value of 1.

The priority of the developed sorting system is to generate output subpopulations with high levels of purity (i.e. low false positives), even at the expense of efficiency (i.e. low true positives) and so points close to the y-axis are preferable to a high true positive rate with a higher false positive rate (i.e. top right of the ROC curve). The slopes of classes A and B are steep but the maximum true positive values are 0.43 and 0.49 respectively. This suggests that many of the target cells are classed non-target cells, even before the threshold is applied. Roughly half of the target cells may be lost but the purity is very high, as seen by the low false positive values, and so pure subpopulations can be obtained. Model C on the other hand provides both high true positive values and low false positive values, with maximum true positive and true negative values of 0.91 and 0.04 respectively. The inserts within the graphs **in Figure 5.5** help illustrate that for all true positive values, the false positive value does not go above 0.05. They also highlight the slow increase of all three ROC curves of the single measurement method of classification.

This is due to the single most indicative values of both cell types being too similar. The values of the compactness factor and the Heywood circularity factor (the two most indicative values) for all of the cell model C images can be seen in **Figure 5.6a**. The purple points are Jurkat images, while the pink points are K562 images. As expected the two clusters overlap, explaining the poor performance of the indicative value classification method.

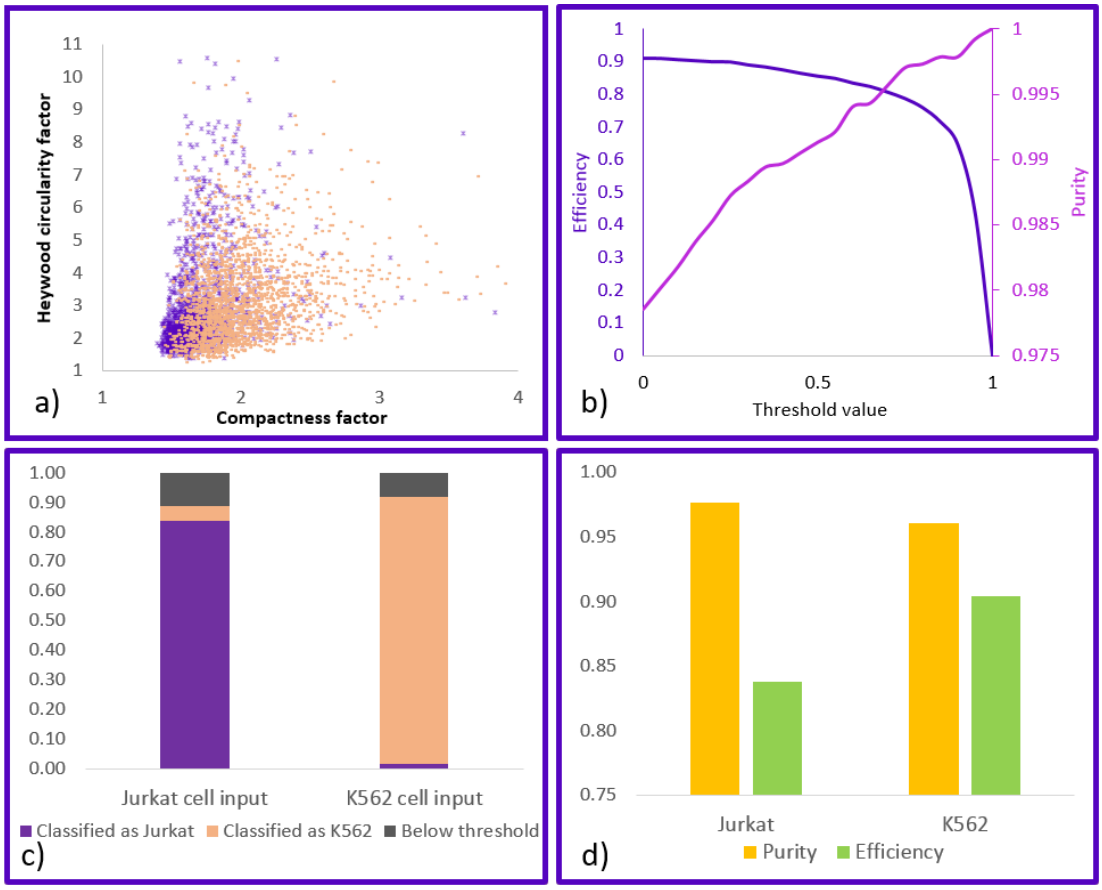

Figure 5.6 *All graphs and charts are for cell model C* **(a)** *Graph plotting the compactness factor and Heywood circularity factor of all Jurkat vs K562 images. These measurements are the two most indicative of the 25 taken.* **(b)** *Graph showing the efficiency and purity of the machine learning classification as the confidence factor threshold is changed.* **(c)** *Chart showing the machine learning classification results of new Jurkat and K562 input images.* **(d)** *Chart with the purity and efficiency of the machine learning software when both Jurkat and K562 cells are the target cells.*

To further investigate the success of the machine learning algorithm with thresholding, the efficiency and purity of the Jurkat vs K562 (model C) at various threshold values was plotted in **Figure 5.6b**. At all threshold values the purity remains above 0.975, but a threshold of 0.65 was chosen to use for future experiments to provide a theoretical purity of 0.99 while maintaining a high efficiency of 0.83. These settings were used to test over 1000 images of both Jurkat and K562 cells, with the resulting classification for each image compared to the true cell type. The fraction of Jurkat and K562 which were classified as each cell type (or waste) can be found in **Figure 5.6c**, with 83.8% of Jurkat cells and 90.4% of K562 cells identified correctly. The threshold removed 9.4% of all images, improving the purity of the output at the expense of efficiency, the results of which are in **Figure 5.6d**. The final classified population of Jurkat and K562 cells had purities of 97.7% and 96.1% respectively. The purity is slightly lower than the theoretical value of 99% but the efficiency is actually higher than the

theoretical value (83%). When compared to the purity value obtained without the thresholding there is a noticeable improvement; the previous classification method could only provide a maximum of 94.2% (as shown in **Figure 5.4c**). This method can now be used to classify Jurkat cells in flow to sort a mixed cell population.

5.6 Detecting bi-nucleated cells

For cell model D, the mono and binucleated hepatocytes, the machine learning software must be more complex, compared to that used for cell models A, B and C. The same initial steps of using three thresholds to find the number of particles within an image and removing small particles, as done in the previous section, are used (and this is shown in the flow diagram in **Figure 5.8**). However, due the possibility of multiple nuclei in a single cell, extra steps need to be taken to ensure that the machine learning software is robust enough to distinguish between a single binucleated cell and two mononucleated cells in close proximity. In many cases if there are two cells within an image, the nuclei will be further apart, when compared to a single cell with two nuclei, and so the distance between the nuclei can be used to distinguish between these two situations. If the centre of the two particles is greater than the average diameter of a hepatocyte cell (20-30 μm)[268,269] then the image is likely to contain two cells and so it will be classified as an image with multiple cells. If the particles are close together then it is likely that only one binucleated cell is present. Example images of both these cases can be found in **Figure 5.7**.

In most cases each nucleus would appear as individual particles on the image, but there are cases where, due to perspective, the nuclei overlap and therefore are counted as one particle (examples of this can be seen in the top row of **Figure 5.7**). The machine learning software can be trained to distinguish between these two cases. Thousands of preclassified images were fed into the machine learning software. As with cell models A and B, the cell images had been manually classified as either a mononucleated cell, a binucleated cell or multiple cells. If the machine learning software only detects one particle in the image there are two possibilities; there is either one nuclei or there are two overlapping nuclei, which the particle counter cannot differentiate between.

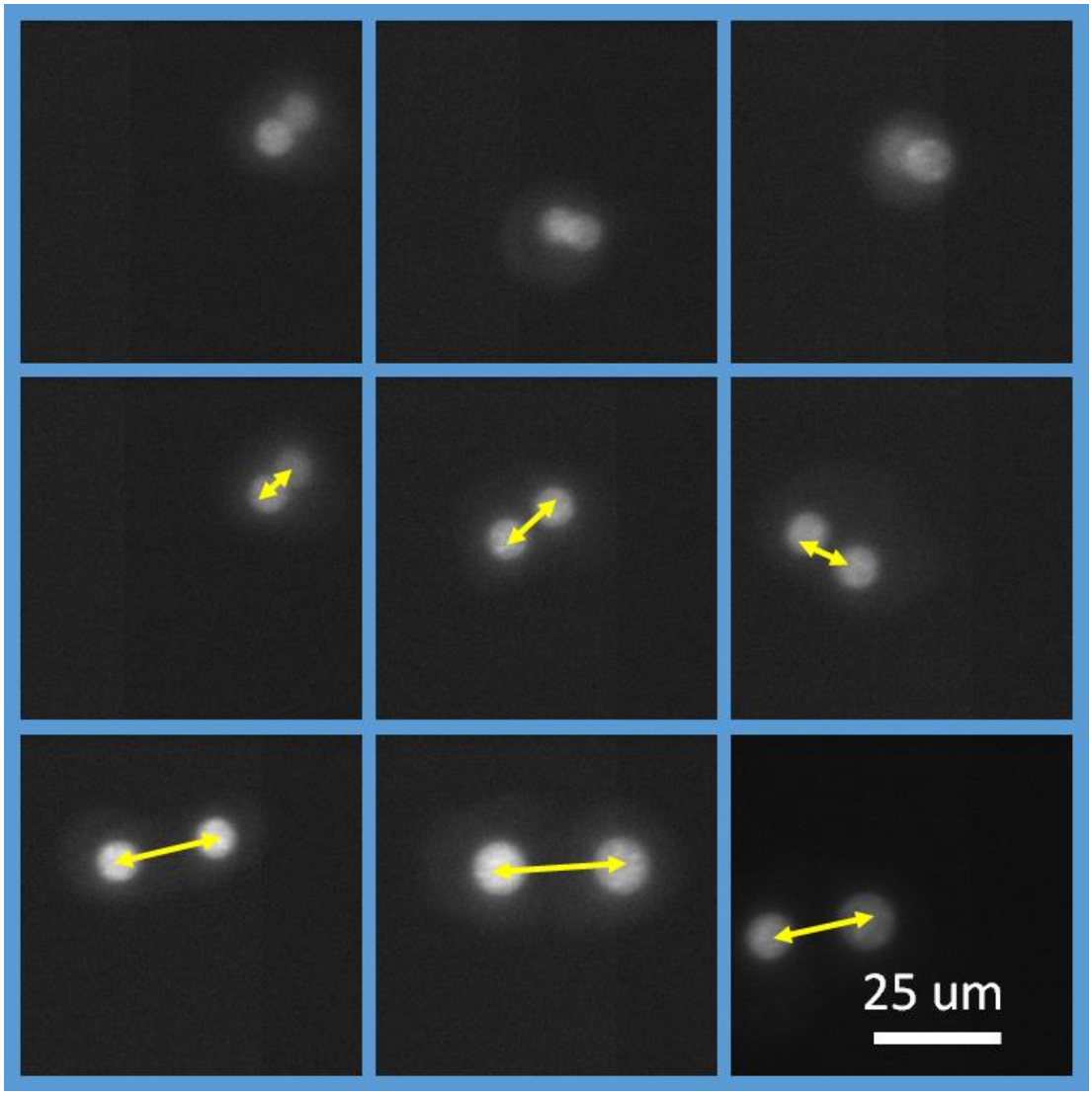

Figure 5.7 *Cell images of hepatocytes. The top and middle rows both show images of binucleated hepatocytes, but in the top row the nuclei appear to overlap due to perspective, while the nuclei of the cells in the middle row are more easily distinguishable. The middle and bottom rows both contain two nuclei but the images in the bottom row contain two mononucleated cells. One way to distinguish the two, is to look at the distance between the nuclei.*

The machine learning software gathers all images that contain one particle and uses the 25 dimensional analysis described in **Section 5.4**. The images have previously been manually classified and so the success of the software, in locating mononucleated cells, can be tested using the method described in **Section 5.4**, where varying numbers of images are used to train the system; which is then used to classify all the images in the cell model image library. The resulting logarithmic graph can be seen in **Figure 5.4d**, with the maximum classification success reaching 94.8 ± 0.1%. It reaches this value after about 200 images, so with 3009 images used to train the final machine learning

classification for a single particle, the software is optimised. Like the previous software for cell models A, B and C the next step was adding a confidence factor threshold.

A flow chart of the machine learning software is shown in **Figure 5.8**. The images are subjected to the same pre-machine learning image preparation as seen previously in **Figure 5.3**, with intensity and particle size thresholds being applied, before a count of the remaining particles. The machine learning software then performs one of three steps depending on the results of the particle count. If there are three or more particles detected, there must be more than two cells in the image (either three mononucleated cells or a mono and binucleated cell) and so the image is classed as a multiple cell image. If there is one particle present, the aforementioned machine learning software will seek to determine the class of the cell (either one nucleus or two overlapping nuclei) using the 25 measurements, and the confidence value threshold is used to reject images which the machine learning software is unsure of. If there are two particles detected then the distance of their separation is used to estimate if one or two cells are present; if there are two, the image will be classified as a multiple cell image. If there is only one then it is likely a single binucleated cell is present. However, to rule out two very close mononucleated cells and to make sure that there are no overlapping nuclei in the image (as some cells can contain more than two nuclei) a second machine learning classification is performed. The technique is almost identical to that done for a single particle, with one change; the number of measurements is doubled, with 25 measurements taken for each particle. If either of the particles is found to contain multiple nuclei, then the image is classified as a multiple cell image, else the image is confirmed as a single cell with two nuclei. Like before, a threshold is used to improve purity. The various outcomes of the whole machine learning process can be found in the flow diagram in **Figure 5.8**.

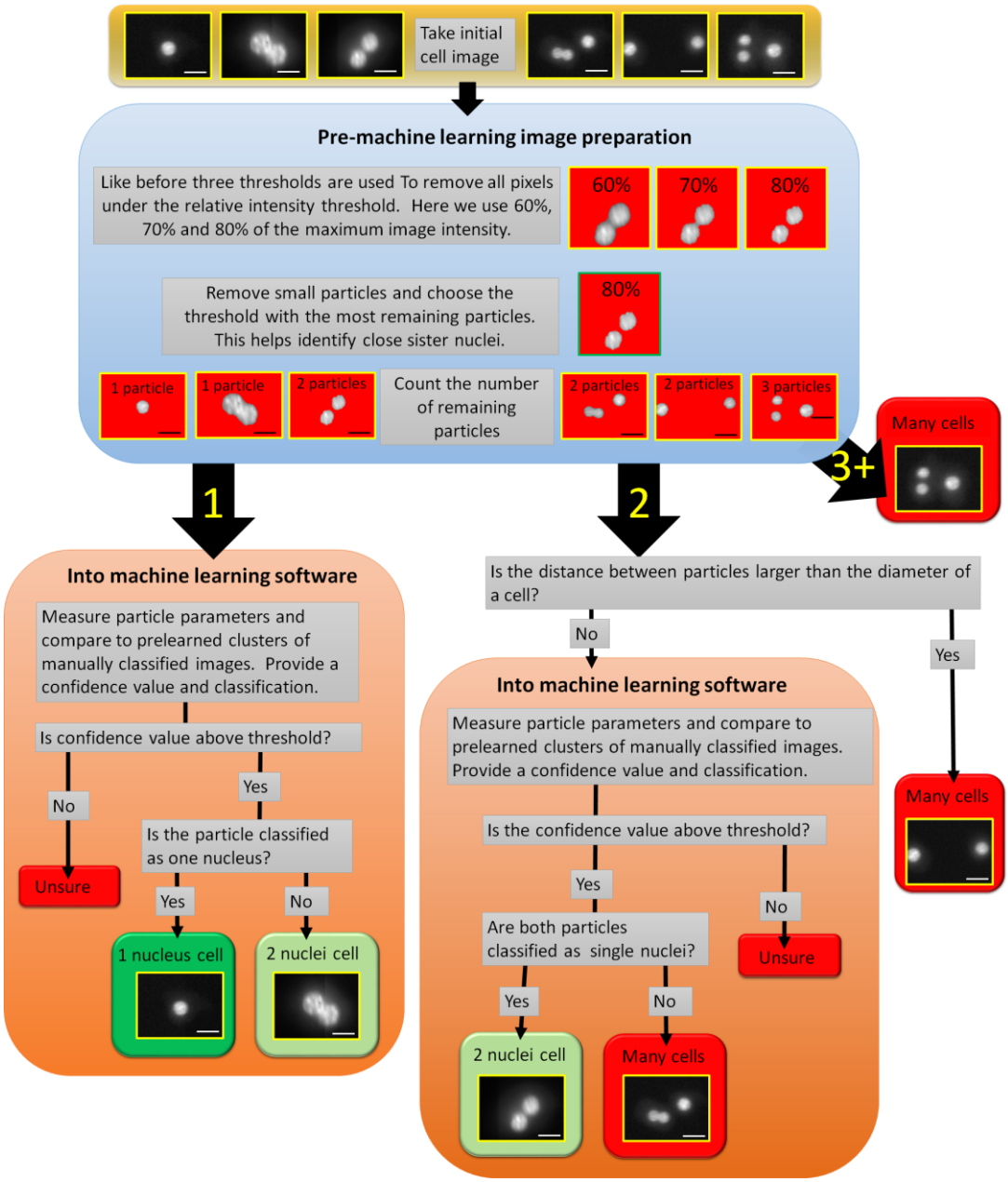

Figure 5.8 *A flow diagram of the cell model D machine learning process. The pre-machine learning image preparation is the same as seen previously in* ***Figure 5.3****, with intensity and particle size thresholds being applied. The remaining particles are then counted, with images containing more than 2 particles classified as a many cells. Images with 1 or 2 particles pass to the machine learning stage. In the case of 1 particle; 25 measurement parameters are taken and these are compared to those of manually classified images. The image is then classified as a mononucleated cell or a binucleated cell and given a confidence value. If this value is below the confidence value threshold the image is classified as 'unsure'. If the value is above the threshold the image will be classed as a '1 nucleus cell' or a '2 nucleus cell'. In the case of two particles being present, an initial test is done to see if the two particles are further apart than one cell diameter, if so the image is classed as many cells. If the particles are closer together then the 25 measurements are taken for each particle and the results are compared to the measurements of previous images. A classification and confidence value is then provided by the software. If the confidence value is below the pre-set threshold, then the image is classified as 'unsure'. If the value is above the threshold the image is classified as '1 nucleus cell' or '2 nuclei cell'. All scale bars are 50 µm.*

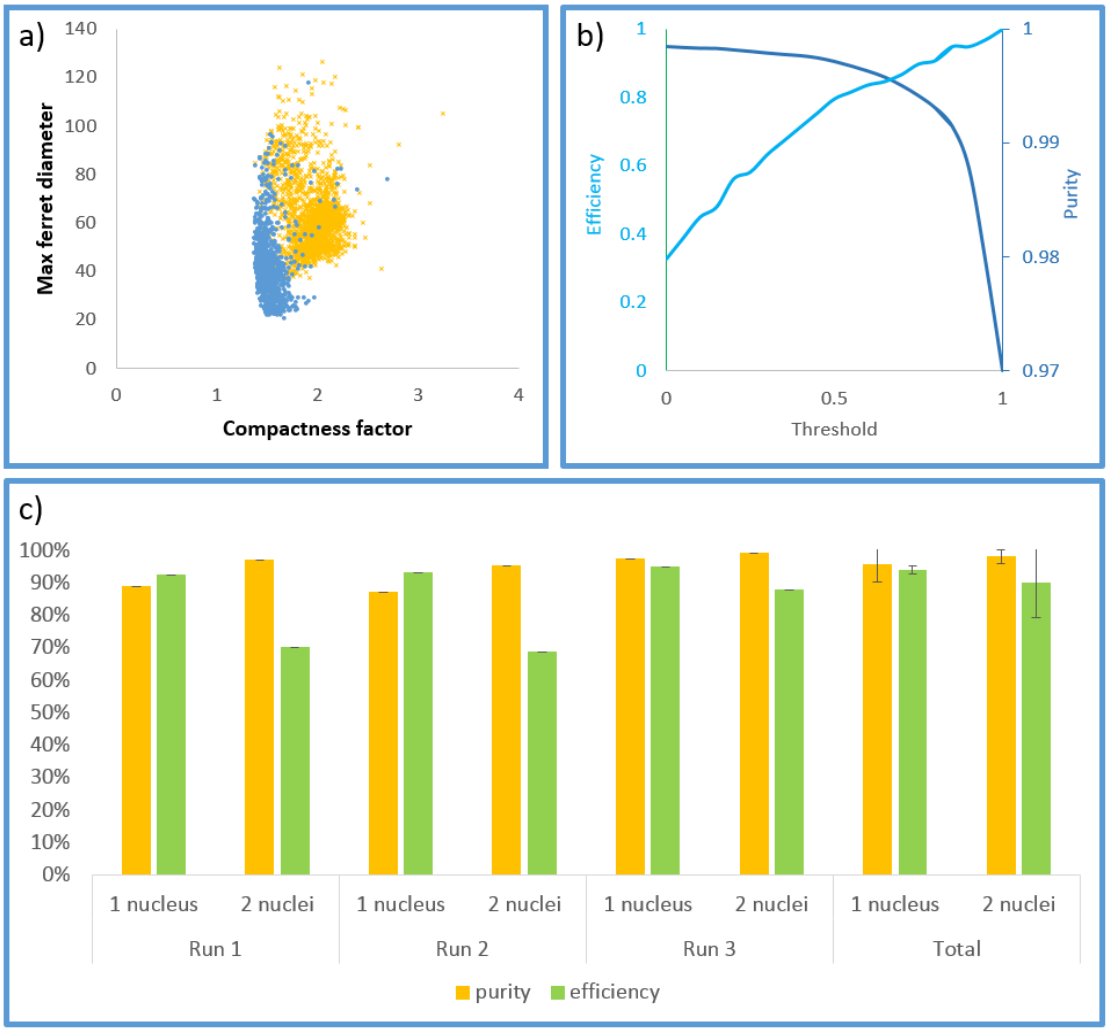

Figure 5.9 *All graphs and charts are for cell model D* **(a)** *Graph plotting the compactness factor and maximum Feret diameter of all single particle images. These measurements are the two most indicative of the 25 taken.* **(b)** *Graph showing the efficiency and purity of the machine learning classification as the confidence factor threshold is changed.* **(c)** *The efficiency and purity of the machine learning outputs for three hepatocyte runs. The 'total' column shows the total purity and efficiency when all images are taken into account and the error bars are the standard deviation of the three runs.*

To test the deterministic ability of the combination of the machine learning software and the confidence value threshold, a ROC curve was generated using the method used in **Section 2.3.9** and it can be found in **Figure 5.5d**. The black line of the most indicative value threshold is much steeper than that of the other three cell models. This can be understood by looking **at Figure 5.9a** which shows the measurements of the compactness factor and the maximum Feret diameter (described in **Section 2.3.9**) for each single particle image. There is a much more obvious separation of the two classes than seen in the case of class C. Even with this classification method generating a steep ROC

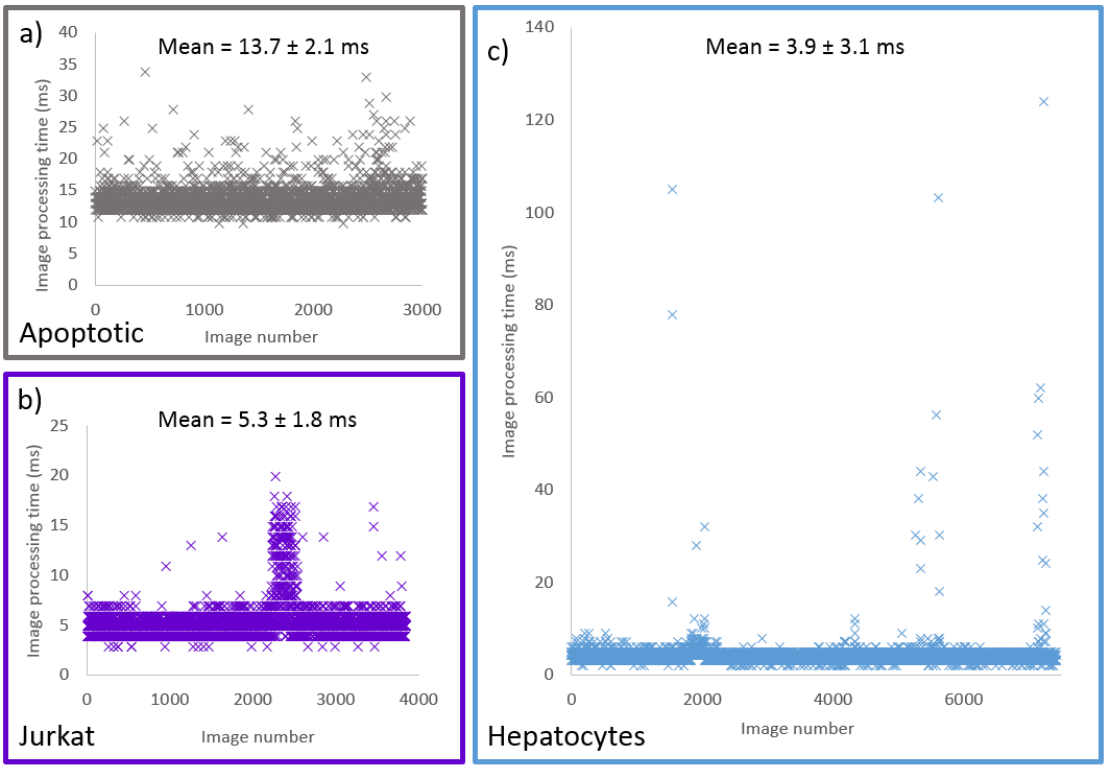

Figure 5.10 *The time taken for the machine learning software to perform a classification for* **(a)** *Apoptotic vs healthy K562 cell images.* **(b)** *Jurkat vs K562 images.* **(c)** *Mononucleated and binucleated hepatocytes. The Each point represents the classification time for a single image.*

curve, the accompanying curve of the thresholding, machine learning, classification method is steeper; indicating its superiority. The purity and efficiency of the classification outcomes were plotted for 11 threshold values (from 0 to 1 in intervals of 0.1), which can be found on **Figure 5.9b**. For all threshold values the purity is greater than 97.5% and greater than the previous maximum value when the thresholding is not used (94.8%). A threshold of 0.4 gives a purity of 99.0% while providing a high efficiency of 92.7%. This classification value threshold was used for single particle image classifications.

To test the success and repeatability of the machine learning software, thousands of images of hepatocytes were taken in flow over multiple runs. The images were then fed into the software and the resulting four classifications (either one nucleus, two nuclei, multiple cells or waste) were analysed and manually confirmed as either correct or incorrect. The purity and efficiencies of each run can be found in **Figure 5.9c**. The output population of mononucleated cells was 95.7 ± 5.5 % pure and the software was able to pick out 93.9 ± 1.2% of the mononucleated input images. While the purity and efficiency of the binucleated cells was 98.1 ± 2.0% and 90.0 ± 10.0% respectively. There is a non-negligible variation between the different runs as shown by the standard deviations with

the purity and efficiency values. But even with these uncertainties the purity values are still better than any of the other three cell models and the efficiencies are both over 90%. This cell model will therefore be used to test the sorting system in future experiments.

Before the machine learning software is tested in flow, it is important to know that the time taken for an image to be classified is not so large that it will affect the system's ability to sort the cells. To do this the image libraries of cell models B, C and D were classified using the software and the time taken for each image was recorded. The results were plotted on the three graphs in **Figure 5.10**. Surprisingly the average time taken for each cell model was less than that in the previous chapter, where only a single threshold value was used (24.1 ± 1.5 ms). The fastest average time was that of the cell model which used the more complicated software (cell model D, the hepatocytes), with an average time of 3.9 ± 3.1 ms. Although the variation in the values was much larger with 20 out of the 7418 images taking longer than 25 ms to be classified, with the maximum value reaching 124 ms. This is still small enough that it should not prevent cells from being sorted when the three camera setup is used. With similar flow rates used, the time between a cell being imaged and appearing at the trigger camera should still be the same as seen in **Section 4.5** (1.4 ± 2.4s). If there is a case when the image processing takes too long, then the cell will continue to waste. The synchronisation with the trigger camera has a timeout and so if the cell is not seen quickly enough, it is assumed that it was missed and so the sort action is cancelled. This prevents any negative impact to the purity of the sort.

5.7 Future work – Sorting the cells

With the imaging and decision making elements of the cell sorting working, the next step was to physically sort the cells within a microfluidic device. With both the microfluidic device design and the sorting setup remaining the same as in **Chapter 4**, similar sorting results would be expected. To test the overall performance of the system, an attempt was made to sort binucleated hepatocytes (from cell model D). A mixture of mononucleated and binucleated hepatocytes, within PBS (with 1% pluronic) and 33% OptiPrep was injected into the microfluidic device. The software was set to detect mononucleated cells, with the piezo firing once the cell was detected, at the piezo region, by the trigger camera. Initial test results can be seen in **Figure 5.11**, where an image of a mononucleated cell being sorted by the piezo can be seen; while a binucleated cell is allowed to pass into the waste channel. More experiments will be required to determine

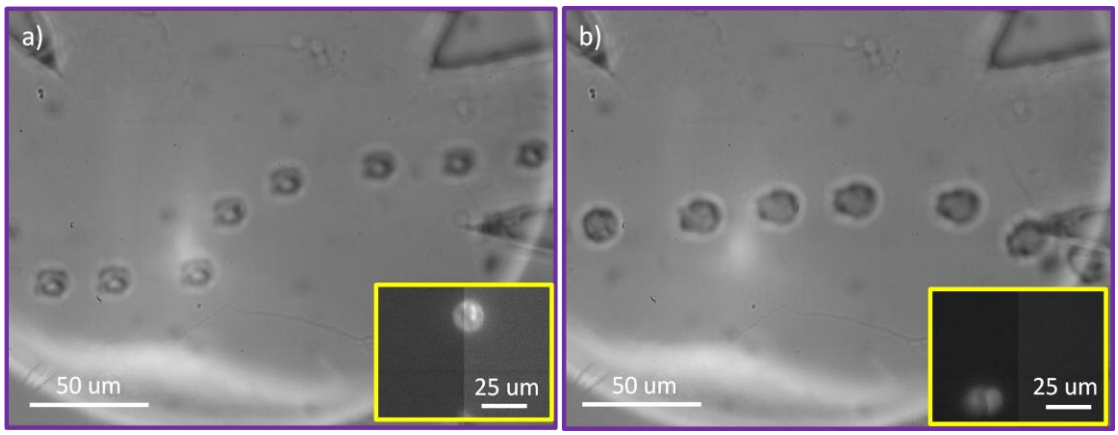

Figure 5.11 *Images showing the trajectory of single hepatocyte cells within the microfluidic device when the software is set to target mononucleated cells.* **(a)** *A mononucleated cell (see inset image) is sorted into the sorting outlet.* **(b)** *A binucleated cell (see inset image) is left to flow into the waste outlet.*

the success of the fluorescence based nuclear cell sorting technique but preliminary tests look promising.

With the machine learning algorithm only needing 200 cell model D images to be close to maximum performance, it may be possible to train the machine learning in flow, during an experiment. The device system could run as a cytometric system where cells are allowed to flow into the waste channel while being imaged by the cell imaging camera. The machine learning software could quickly auto classify the cell image, with low certainty classifications being manually checked. The resulting classified images could then be used to train the machine learning software as the experiment is running. The software will then be ready to classify new cells and the in flow sorting can be enabled. This will allow the classification to be tailored to the cell sample of that particular day and so the results should be more accurate. In previous experiments multiple runs have to be performed to make the machine learning software robust enough to deal with cell images from a new run, as cell images can differ slightly from run to run. This may be due to the health of the cell sample, the focus of the microscope, the uptake of the Hoechst dye, etc. By using the same data set of cell images that will be sorted to train the software, the experiment changes from a multi-day experiment to one that can be done in one day. The current setup works successfully but it would be interesting to try this single day method in the future.

5.8 Conclusion

By modifying the previous setup in **Chapter 4** to allow for fluorescent imaging, it is possible to observe the nuclear morphologies of various cell models. Using this imaging technique it was possible to observe; differences in the nuclear shape (healthy vs apoptotic K562 cells and Jurkat vs K562 cells), differences in the number of nuclei (mononucleated and binucleated hepatocytes) and even differences in sub nuclear morphology (spotty SAHF positive vs smooth SAHF negative fibroblast nuclei). A new classification technique has been demonstrated, where preclassified images are used to train a machine learning algorithm. A threshold is then applied to filter out cases where the algorithm is unsure. It has been shown that this technique provides better results than that of the previously used one measurement threshold, providing purities and efficiencies of up to 98.1 ± 2.0% and 93.9 ± 1.2% respectively. Initial tests show that when used to classify cells in flow, the system is able to successfully pick out target cells and sort them into the correct outlet.

Conclusions

The main goal of this project was to employ real-time image-based feedback to microfluidic systems to enhance current applications and to create new ones. The ability to observe experiments occurring within the microfluidic device and adjust the flow in the system accordingly has been critical in both the improvement of monodispersity in microdroplet generation and the ability to sort cells based on their morphologies. The main accomplishments within this body of work are:

1. Delivering a technique which displays a superior droplet monodispersity when compared to the state-of-the-art, with a coefficient of variation of 0.32%.
2. Employing two feedback systems to accurately control and adjust the feedback and volume of droplet generation in flow, for the first time.
3. Creating a microfluidic image-based sorting technique, which can distinguish between different cell types using brightfield imaging and sort them into different subpopulations with a purity of 99.4% and an efficiency of 91.3%.
4. Building a fluorescent imaging system which can image cell nuclei and accurately identify the corresponding cell type.

To provide more precise droplet formation with a wide range of controllable parameters, a closed loop image feedback system was employed. Microdroplets were imaged after formation and the volume of each droplet and the frequency of the overall droplet production was calculated. Using these measurements, a dual feedback system could accurately control and change both the volume and frequency of droplet formation to values of a user's choice. The volume control provided a coefficient of variation of the system measured to be 0.32%, which is the smallest found to date. The work also demonstrated how image-based feedback could be used in other applications such as controlling the average number of cells per droplet, by regulating the ratio of the flow rates of two aqueous inlets. This work was published in Crawford, *et al* [119] and it has been claimed that such a tight control over both the frequency and volume of droplet formation may be useful in applications such as PCR[270].

By taking advantage of the ability to image cells within a microfluidic device, a setup was built to image cells in flow and to use real-time software to categorise them into specific subpopulations. The software then feeds this back to a piezo-electric element, which was set up to inject a pulse of liquid into the device to sort the identified target cells. The system was initially tested using a solution of RBCs and K562 cells mixed together, and from the brightfield transmission image of the cells, the projected

area of each imaged cell was used as a defining characteristic. If the area of a cell was over a predefined threshold, the cell would be classified as a target K562 cell and would be directed to the sorting outlet; cells with a measured projected area under this threshold were directed to the waste channel. It was shown that K562 cells could be sorted with an efficiency of 91.3% and a purity of 99.4%. This is comparable to current image-based sorting techniques[35].

To widen the applicability of the developed image based cell sorting technique, the setup was adapted to allow for fluorescent imaging. This increased the range of cell types that could be identified, such as similar cell types with different nuclear morphologies. The optical setup directed the fluorescence emission to one camera, in this case to image the fluorescently stained nucleus of each cell; while another two cameras were used to confirm the position of the cell, at both the piezo region to allow synchronised sorting, and the outlets to visually confirm the correct sort. Four cell models were imaged in flow and fed into a machine learning software. The trained software was then able to accurately predict cell classes ~97% of the time with an efficiency >85%. Initial sorting tests were positive showing that the cells could be imaged, identified and sorted within the devices. Building upon this work it should be possible to develop a fluorescent-imaging sorter which can be adapted to a wide variety of microscopes and in a range of different labs. Image-based cell sorting will open up a whole new world of possibilities in the field of genomics and it will surely become the gold standard technique in the years to come.

References

1. Huebner, A. *et al.* Microdroplets: a sea of applications? *Lab Chip* **8**, 1244–1254 (2008).

2. Mazutis, L. *et al.* Single-cell analysis and sorting using droplet-based microfluidics. *Nat. Protoc.* **8**, 870–91 (2013).

3. Kruger, J. *et al.* Development of a microfluidic device for fluorescence activated cell sorting. *J. Micromechanics Microengineering* **12**, 486–494 (2002).

4. Huh, D., Gu, W., Kamotani, Y., Grotberg, J. B. & Takayama, S. Microfluidics for flow cytometric analysis of cells and particles. *Physiol. Meas.* **26**, R73 (2005).

5. Sun, T. & Morgan, H. Single-cell microfluidic impedance cytometry: a review. *Microfluid. Nanofluidics* **8**, 423–443 (2010).

6. Ezkurdia, I. *et al.* Multiple evidence strands suggest that there may be as few as 19,000 human protein-coding genes. *Hum. Mol. Genet.* **23**, 5866–5878 (2014).

7. Terry, S. C., Herman, J. H. & Angell, J. B. A gas chromatographic air analyzer fabricated on a silicon wafer. *IEEE Trans. Electron Devices* **26**, 1880–1886 (1979).

8. Sackmann, E. K., Fulton, A. L. & Beebe, D. J. The present and future role of microfluidics in biomedical research. *Nature* **507**, 181–189 (2014).

9. Volpatti, L. R. & Yetisen, A. K. Commercialization of microfluidic devices. *Trends Biotechnol.* **32**, 347–350 (2014).

10. Zare, R. N. & Kim, S. Microfluidic platforms for single-cell analysis. *Annu. Rev. Biomed. Eng.* **12**, 187–201 (2010).

11. AVCI, H., GÜZEL, F. D., Erol, S. & Akpek, A. Recent advances in organ-on-a-chip technologies and future challenges: a review. *Turkish J. Chem.* **42**, 587–610 (2018).

12. Ahn, J. *et al.* Microfluidics in nanoparticle drug delivery; From synthesis to pre-clinical screening. *Adv. Drug Deliv. Rev.* **128**, 29–53 (2018).

13. Gong, M. M. & Sinton, D. Turning the page: advancing paper-based microfluidics

for broad diagnostic application. *Chem. Rev.* **117**, 8447–8480 (2017).

14. Lin, J.-M. *Cell Analysis on Microfluidics*. (Springer, 2018).

15. Zhu, P. & Wang, L. Passive and active droplet generation with microfluidics: a review. *Lab Chip* **17**, 34–75 (2017).

16. Bhatia, S. N. & Ingber, D. E. Microfluidic organs-on-chips. *Nat. Biotechnol.* **32**, 760 (2014).

17. Yu, F. & Choudhury, D. Microfluidic bioprinting for organ-on-a-chip models. *Drug Discov. Today* (2019).

18. Lee, H. & Cho, D.-W. One-step fabrication of an organ-on-a-chip with spatial heterogeneity using a 3D bioprinting technology. *Lab Chip* **16**, 2618–2625 (2016).

19. Li, Y., Zhu, K., Liu, X. & Zhang, Y. S. Blood-vessel-on-a-chip Platforms for Evaluating Nanoparticle Drug Delivery Systems. *Curr. Drug Metab.* **19**, 100–109 (2018).

20. Naseer, S. M. *et al.* Surface acoustic waves induced micropatterning of cells in gelatin methacryloyl (GelMA) hydrogels. *Biofabrication* **9**, 15020 (2017).

21. Lee, J. & Kim, S. Kidney-on-a-Chip: A new technology for predicting drug efficacy, interactions, and drug-induced nephrotoxicity. *Curr. Drug Metab.* **19**, 577–583 (2018).

22. Beckwitt, C. H. *et al.* Liver 'organ on a chip'. *Exp. Cell Res.* **363**, 15–25 (2018).

23. Huh, D. A human breathing lung-on-a-chip. *Ann. Am. Thorac. Soc.* **12**, S42–S44 (2015).

24. Kimura, H., Sakai, Y. & Fujii, T. Organ/body-on-a-chip based on microfluidic technology for drug discovery. *Drug Metab. Pharmacokinet.* **33**, 43–48 (2018).

25. Low, L. A. & Tagle, D. A. Microphysiological systems ("organs-on-chips") for drug efficacy and toxicity testing. *Clin. Transl. Sci.* **10**, 237 (2017).

26. Sharma, S., Zapatero-Rodríguez, J., Estrela, P. & O'Kennedy, R. Point-of-care diagnostics in low resource settings: present status and future role of microfluidics.

Biosensors **5**, 577–601 (2015).

27. Na, W., Nam, D., Lee, H. & Shin, S. Rapid molecular diagnosis of infectious viruses in microfluidics using DNA hydrogel formation. *Biosens. Bioelectron.* **108**, 9–13 (2018).

28. Ghazani, A. A. *et al.* Comparison of select cancer biomarkers in human circulating and bulk tumor cells using magnetic nanoparticles and a miniaturized micro-NMR system. *Nanomedicine Nanotechnology, Biol. Med.* **9**, 1009–1017 (2013).

29. Nasseri, B. *et al.* Point-of-care microfluidic devices for pathogen detection. *Biosens. Bioelectron.* **117**, 112–128 (2018).

30. Carrilho, E., Martinez, A. W. & Whitesides, G. M. Understanding Wax Printing: A Simple Micropatterning Process for Paper-Based Microfluidics. *Anal. Chem.* **81**, 7091–7095 (2009).

31. Mahadeva, S. K., Walus, K. & Stoeber, B. Paper as a platform for sensing applications and other devices: A review. *ACS Appl. Mater. Interfaces* **7**, 8345–8362 (2015).

32. Xu, G. *et al.* Paper-Origami-Based Multiplexed Malaria Diagnostics from Whole Blood. *Angew. Chemie Int. Ed.* **55**, 15250–15253 (2016).

33. Tsai, T.-T., Shen, S.-W., Cheng, C.-M. & Chen, C.-F. Paper-based tuberculosis diagnostic devices with colorimetric gold nanoparticles. *Sci. Technol. Adv. Mater.* **14**, 44404 (2013).

34. Fu, E. Paper Microfluidics for POC Testing in Low-Resource Settings BT - Applications of Microfluidic Systems in Biology and Medicine. in (ed. Tokeshi, M.) 325–352 (Springer Singapore, 2019). doi:10.1007/978-981-13-6229-3_12

35. Nitta, N. *et al.* Intelligent Image-Activated Cell Sorting. *Cell* **175**, 266-276.e13 (2018).

36. Chen, C. H., Cho, S. H., Tsai, F., Erten, A. & Lo, Y.-H. Microfluidic cell sorter with integrated piezoelectric actuator. *Biomed. Microdevices* **11**, 1223 (2009).

37. English, B. P. & Singer, R. H. A three-camera imaging microscope for high-speed

single-molecule tracking and super-resolution imaging in living cells. in *Biosensing and Nanomedicine VIII* **9550**, 955008 (International Society for Optics and Photonics, 2015).

38. Bhagat, A. A. S. *et al.* Microfluidics for cell separation. *Med. Biol. Eng. Comput.* **48**, 999–1014 (2010).

39. Bailey, R. C., Kwong, G. A., Radu, C. G., Witte, O. N. & Heath, J. R. DNA-encoded antibody libraries: a unified platform for multiplexed cell sorting and detection of genes and proteins. *J. Am. Chem. Soc.* **129**, 1959–1967 (2007).

40. Yi, C., Li, C. W., Ji, S. & Yang, M. Microfluidics technology for manipulation and analysis of biological cells. *Anal. Chim. Acta* **560**, 1–23 (2006).

41. Lagus, T. P. & Edd, J. F. A review of the theory, methods and recent applications of high-throughput single-cell droplet microfluidics. *J. Phys. D. Appl. Phys.* **46**, 114005 (2013).

42. Wyatt Shields IV, C., Reyes, C. D. & Lopez, G. P. Microfluidic cell sorting: a review of the advances in the separation of cells from debulking to rare cell isolation. *Lab Chip* **15**, 1230–1249 (2015).

43. Chabert, M. & Viovy, J.-L. Microfluidic high-throughput encapsulation and hydrodynamic self-sorting of single cells. *Proc. Natl. Acad. Sci. U. S. A.* **105**, 3191–3196 (2008).

44. Sarioglu, a F. *et al.* A microfluidic device for label-free, physical capture of circulating tumor cell clusters. *Nat. Methods* **12**, 1–10 (2015).

45. Theberge, A. B. *et al.* Suzuki-Miyaura coupling reactions in aqueous microdroplets with catalytically active fluorous interfaces. *Chem. Commun. (Camb).* **2009**, 6225–7 (2009).

46. Courtois, F. *et al.* An integrated device for monitoring time-dependent in vitro expression from single genes in picolitre droplets. *Chembiochem A Eur. J. Chem. Biol.* **9**, 439–446 (2008).

47. Huebner, A. *et al.* Development of quantitative cell-based enzyme assays in microdroplets. *Anal. Chem.* **80**, 3890–6 (2008).

48. Macosko, E. Z. *et al.* Highly Parallel Genome-wide Expression Profiling of Individual Cells Using Nanoliter Droplets. *Cell* **161**, 1202–1214 (2015).

49. Theberge, A. B., Whyte, G. & Huck, W. T. S. Generation of picoliter droplets with defined contents and concentration gradients from the separation of chemical mixtures. *Anal. Chem.* **82**, 3449–3453 (2010).

50. Salmon, A. R. *et al.* Monitoring Early-Stage Nanoparticle Assembly in Microdroplets by Optical Spectroscopy and SERS. *Small* 1–9 (2016). doi:10.1002/smll.201503513

51. Zhang, Y. & Jiang, H. R. A review on continuous-flow microfluidic PCR in droplets: Advances, challenges and future. *Anal. Chim. Acta* **914**, 7–16 (2016).

52. Jang, M., Yang, S. & Kim, P. Microdroplet-based cell culture models and their application. *BioChip J.* **10**, 310–317 (2016).

53. Huebner, A. *et al.* Static microdroplet arrays: a microfluidic device for droplet trapping, incubation and release for enzymatic and cell-based assays. *Lab Chip* **9**, 692–698 (2009).

54. Brouzes, E. *et al.* Droplet microfluidic technology for single-cell high-throughput screening. *Proc. Natl. Acad. Sci.* **106**, 14195–14200 (2009).

55. Frenz, L. *et al.* Droplet-based microreactors for the synthesis of magnetic iron oxide nanoparticles. *Angew. Chemie Int. Ed.* **47**, 6817–6820 (2008).

56. Bendall, S. C. *et al.* Single-cell mass cytometry of differential immune and drug responses across a human hematopoietic continuum. *Science (80-.).* **332**, 687–696 (2011).

57. Fong, E. J. *et al.* A Microfluidic Platform for Precision Small-volume Sample Processing and Its Use to Size Separate Biological Particles with an Acoustic Microdevice. *J. Vis. Exp.* 1–11 (2015). doi:10.3791/53051

58. Sun, M., Bithi, S. S. & Vanapalli, S. A. Microfluidic static droplet arrays with tuneable gradients in material composition. *Lab Chip* **11**, 3949–3952 (2011).

59. Mardis, E. R. The impact of next-generation sequencing technology on genetics.

Trends Genet. **24**, 133–141 (2008).

60. Fu, A. Y., Chou, H., Spence, C., Arnold, F. H. & Quake, S. R. An Integrated Microfabricated Cell Sorter. **74**, 5206–5212 (2002).

61. Macosko, E. Z. *et al.* Highly Parallel Genome-wide Expression Profiling of Individual Cells Using Nanoliter Droplets. *Cell* **161**, 1202–1214 (2015).

62. Christopher, G. F. & Anna, S. L. Microfluidic methods for generating continuous droplet streams. *J. Phys. D. Appl. Phys.* **40**, R319–R336 (2007).

63. Bruus, H. *Theoretical microfluidics*. **18**, (Oxford university press Oxford, 2008).

64. Di Carlo, D. Inertial microfluidics. *Lab Chip* **9**, 3038–3046 (2009).

65. Schlichting, H. & Gersten, K. *Boundary-layer theory*. (Springer, 2016).

66. Shui, L., Eijkel, J. C. T. & van den Berg, A. Multiphase flow in microfluidic systems – Control and applications of droplets and interfaces. *Adv. Colloid Interface Sci.* **133**, 35–49 (2007).

67. Zhao, C.-X. & Middelberg, A. P. J. Two-phase microfluidic flows. *Chem. Eng. Sci.* **66**, 1394–1411 (2011).

68. Hu, Y., Pine, D. & Leal, L. *Drop deformation, breakup, and coalescence with compatibilizer*. *Physics of Fluids* **12**, (2000).

69. Baroud, C. N., Gallaire, F. & Dangla, R. Dynamics of microfluidic droplets. *Lab Chip* **10**, 2032–2045 (2010).

70. Pamme, N. Continuous flow separations in microfluidic devices. *Lab Chip* **7**, 1644–1659 (2007).

71. Bibette, J., Calderon, F. L. & Poulin, P. Emulsions: basic principles. *Reports Prog. Phys.* **62**, 969–1033 (1999).

72. Tadros, T. F. *Applied surfactants: principles and applications*. (John Wiley & Sons, 2006).

73. Baret, J.-C. Surfactants in droplet-based microfluidics. *Lab Chip* **12**, 422–433 (2012).

74. Rosen, M. J. & Kunjappu, J. T. Surfactants and Interfacial Phenomena. *Inc., Hoboken, New Jersey* 150–225 (2012).

75. Holt, D. J., Payne, R. J. & Abell, C. Synthesis of novel fluorous surfactants for microdroplet stabilisation in fluorous oil streams. *J. Fluor. Chem.* **131**, 398–407 (2010).

76. Aronson, M. P. The role of free surfactant in destabilizing oil-in-water emulsions. *Langmuir* **5**, 494–501 (1989).

77. Wagner, O. *et al.* Biocompatible fluorinated polyglycerols for droplet microfluidics as an alternative to PEG-based copolymer surfactants. *Lab Chip* **16**, 65–69 (2016).

78. Thorsen, T., Roberts, R. W., Arnold, F. H. & Quake, S. R. Dynamic Pattern Formation in a Vesicle-Generating Microfluidic Device. *Phys. Rev. Lett.* **86**, 4163–4166 (2001).

79. Garstecki, P., Fuerstman, M. J., Stone, H. A. & Whitesides, G. M. Formation of droplets and bubbles in a microfluidic T-junction—scaling and mechanism of break-up. *Lab Chip* **6**, 437–446 (2006).

80. Leshansky, A. M. & Pismen, L. M. Breakup of drops in a microfluidic T junction. *Phys. Fluids* **21**, 23303 (2009).

81. Christopher, G. F., Noharuddin, N. N., Taylor, J. A. & Anna, S. L. Experimental observations of the squeezing-to-dripping transition in T-shaped microfluidic junctions. *Phys. Rev. E* **78**, 36317 (2008).

82. Cramer, C., Fischer, P. & Windhab, E. J. Drop formation in a co-flowing ambient fluid. *Chem. Eng. Sci.* **59**, 3045–3058 (2004).

83. Utada, A. S., Fernandez-Nieves, A., Gordillo, J. M. & Weitz, D. A. Absolute Instability of a Liquid Jet in a Coflowing Stream. *Phys. Rev. Lett.* **100**, 14502 (2008).

84. Deng, C., Wang, H., Huang, W. & Cheng, S. Numerical and experimental study of oil-in-water (O/W) droplet formation in a co-flowing capillary device. *Colloids Surfaces A Physicochem. Eng. Asp.* **533**, 1–8 (2017).

85. Guillot, P., Colin, A. & Ajdari, A. Stability of a jet in confined pressure-driven biphasic flows at low Reynolds number in various geometries. *Phys. Rev. E* **78**, 16307 (2008).

86. Hong, Y. & Wang, F. Flow rate effect on droplet control in a co-flowing microfluidic device. *Microfluid. Nanofluidics* **3**, 341–346 (2007).

87. DE MENECH, M., GARSTECKI, P., JOUSSE, F. & STONE, H. A. Transition from squeezing to dripping in a microfluidic T-shaped junction. *J. Fluid Mech.* **595**, 141–161 (2008).

88. Anna, S. L. & Mayer, H. C. Microscale tipstreaming in a microfluidic flow focusing device. *Phys. Fluids* **18**, 121512 (2006).

89. Garstecki, P., Stone, H. A. & Whitesides, G. M. Mechanism for Flow-Rate Controlled Breakup in Confined Geometries: A Route to Monodisperse Emulsions. *Phys. Rev. Lett.* **94**, 164501 (2005).

90. Dollet, B., van Hoeve, W., Raven, J.-P., Marmottant, P. & Versluis, M. Role of the Channel Geometry on the Bubble Pinch-Off in Flow-Focusing Devices. *Phys. Rev. Lett.* **100**, 34504 (2008).

91. Utada, A. S., Fernandez-Nieves, A., Stone, H. A. & Weitz, D. A. Dripping to Jetting Transitions in Coflowing Liquid Streams. *Phys. Rev. Lett.* **99**, 94502 (2007).

92. Vladisavljević, G. T., Duncanson, W. J., Shum, H. C. & Weitz, D. A. Emulsion Templating of Poly(lactic acid) Particles: Droplet Formation Behaviorfile:///C:/Users/Graeme/Downloads/CambridgeCore_CitationExport_5Apr2019.ris. *Langmuir* **28**, 12948–12954 (2012).

93. Fu, T., Wu, Y., Ma, Y. & Li, H. Z. Droplet formation and breakup dynamics in microfluidic flow-focusing devices: from dripping to jetting. *Chem. Eng. Sci.* **84**, 207–217 (2012).

94. Tseng, Y.-H. & Prosperetti, A. Local interfacial stability near a zero vorticity point. *J. Fluid Mech.* **776**, 5–36 (2015).

95. Anna, S. L. Droplets and Bubbles in Microfluidic Devices. *Annu. Rev. Fluid Mech.*

48, 285–309 (2016).

96. Stone, H. A. Dynamics of Drop Deformation and Breakup in Viscous Fluids. *Annu. Rev. Fluid Mech.* **26**, 65–102 (1994).

97. Shim, J. *et al.* Ultrarapid Generation of Femtoliter Microfluidic Droplets for Single-Molecule-Counting Immunoassays. *ACS Nano* **7**, 5955–5964 (2013).

98. Zhu, P. *et al.* Droplet Breakup in Expansion-contraction Microchannels. *Sci. Rep.* **6**, 21527 (2016).

99. Zhu, P., Kong, T., Kang, Z., Tian, X. & Wang, L. Tip-multi-breaking in Capillary Microfluidic Devices. *Sci. Rep.* **5**, 11102 (2015).

100. Köster, S. *et al.* Drop-based microfluidic devices for encapsulation of single cells. *Lab Chip* **8**, 1110–1115 (2008).

101. Niu, X., Gielen, F., Edel, J. B. & deMello, A. J. A microdroplet dilutor for high-throughput screening. *Nat. Chem.* **3**, 437 (2011).

102. Nguyen, N.-T., Lassemono, S. & Chollet, F. A. Optical detection for droplet size control in microfluidic droplet-based analysis systems. *Sensors Actuators B Chem.* **117**, 431–436 (2006).

103. Elbuken, C., Glawdel, T., Chan, D. & Ren, C. L. Detection of microdroplet size and speed using capacitive sensors. *Sensors Actuators A Phys.* **171**, 55–62 (2011).

104. Musterd, M., van Steijn, V., Kleijn, C. R. & Kreutzer, M. T. Calculating the volume of elongated bubbles and droplets in microchannels from a top view image. *RSC Adv.* **5**, 16042–16049 (2015).

105. Ferraro, D. *et al.* Controlling the distance of highly confined droplets in a capillary by interfacial tension for merging on-demand. *Lab Chip* **19**, 136–146 (2019).

106. Chen, X., Glawdel, T., Cui, N. & Ren, C. L. Model of droplet generation in flow focusing generators operating in the squeezing regime. *Microfluid. Nanofluidics* **18**, 1341–1353 (2015).

107. Glawdel, T. & Ren, C. L. Droplet formation in microfluidic T-junction generators operating in the transitional regime. III. Dynamic surfactant effects. *Phys. Rev. E*

86, 26308 (2012).

108. Bransky, A., Korin, N., Khoury, M. & Levenberg, S. A microfluidic droplet generator based on a piezoelectric actuator. *Lab Chip* **9**, 516–520 (2009).

109. Abate, A. R. & Weitz, D. A. Single-layer membrane valves for elastomeric microfluidic devices. *Appl. Phys. Lett.* **92**, 243509 (2008).

110. Baroud, C. N., de Saint Vincent, M. R. & Delville, J.-P. An optical toolbox for total control of droplet microfluidics. *Lab Chip* **7**, 1029–1033 (2007).

111. Link, D. R. *et al.* Electric control of droplets in microfluidic devices. *Angew. Chemie - Int. Ed.* **45**, 2556–2560 (2006).

112. Ward, T., Faivre, M., Abkarian, M. & Stone, H. A. Microfluidic flow focusing: Drop size and scaling in pressure versus flow-rate-driven pumping. *Electrophoresis* **26**, 3716–3724 (2005).

113. Nisisako, T., Torii, T. & Higuchi, T. Droplet formation in a microchannel network. *Lab Chip* **2**, 24–26 (2002).

114. Faustini, M. *et al.* Microfluidic approach toward continuous and ultrafast synthesis of metal-organic framework crystals and hetero structures in confined microdroplets. *J. Am. Chem. Soc.* **135**, 14619–14626 (2013).

115. Zeng, W., Li, S. & Wang, Z. Closed-loop feedback control of droplet formation in a T-junction microdroplet generator. *Sensors Actuators A Phys.* **233**, 542–547 (2015).

116. Zeng, W., Jacobi, I., Beck, D. J., Li, S. & Stone, H. A. Characterization of syringe-pump-driven induced pressure fluctuations in elastic microchannels. *Lab Chip* **15**, 1110–1115 (2015).

117. Zeng, W., Jacobi, I., Li, S. & Stone, H. A. Variation in polydispersity in pump- and pressure-driven micro-droplet generators. *J. Micromechanics Microengineering* **25**, 115015 (2015).

118. Abate, A. R., Romanowsky, M. B., Agresti, J. J. & Weitz, D. A. Valve-based flow focusing for drop formation. *Appl. Phys. Lett.* **94**, 10–13 (2009).

119. Crawford, D. F., Smith, C. A. & Whyte, G. Image-based closed-loop feedback for highly mono-dispersed microdroplet production. *Sci. Rep.* **7**, 10545 (2017).

120. Korczyk, P. M., Cybulski, O., Makulska, S. & Garstecki, P. Effects of unsteadiness of the rates of flow on the dynamics of formation of droplets in microfluidic systems. *Lab Chip* **11**, 173–175 (2011).

121. Gielen, F. *et al.* Interfacing Microwells with Nanoliter Compartments: A Sampler Generating High-Resolution Concentration Gradients for Quantitative Biochemical Analyses in Droplets. *Anal. Chem.* **87**, 624–632 (2015).

122. Gulati, S. *et al.* Microdroplet formation in rounded flow-focusing junctions. *Microfluid. Nanofluidics* **20**, 2 (2016).

123. Dutka, F., Opalski, A. S. & Garstecki, P. Nano-liter droplet libraries from a pipette: step emulsificator that stabilizes droplet volume against variation in flow rate. *Lab Chip* **16**, 2044–2049 (2016).

124. Vladisavljević, G. T. *et al.* Long-term stability of droplet production by microchannel (step) emulsification in microfluidic silicon chips with large number of terraced microchannels. *Chem. Eng. J.* **333**, 380–391 (2018).

125. Li, X., Li, D., Liu, X. & Chang, H. Ultra-monodisperse droplet formation using PMMA microchannels integrated with low-pulsation electrolysis micropumps. *Sensors Actuators B Chem.* **229**, 466–475 (2016).

126. Chen, Y. *et al.* Rare cell isolation and analysis in microfluidics. *Lab Chip* **14**, 626–645 (2014).

127. Chin, L., Andersen, J. N. & Futreal, P. A. Cancer genomics: from discovery science to personalized medicine. *Nat. Med.* **17**, 297 (2011).

128. Walker, A. & Parkhill, J. Single-cell genomics. (2008).

129. Fulwyler, M. J. Electronic separation of biological cells by volume. *Science (80-.).* **150**, 910–911 (1965).

130. H. R. Hulett, W. A. Bonner, Janet Barrett, L. A. H. Cell Sorting : Automated Separation of Mammalian Cells as a Function. *Science (80-.).* **166**, 747–749

(1969).

131. Faraghat, S. A. *et al.* High-throughput, low-loss, low-cost, and label-free cell separation using electrophysiology-activated cell enrichment. *Proc. Natl. Acad. Sci.* **114**, 4591–4596 (2017).

132. Norouzi, N., Bhakta, H. C. & Grover, W. H. Sorting cells by their density. *PLoS One* **12**, e0180520 (2017).

133. Fu, A. Y., Spence, C., Scherer, A., Arnold, F. H. & Quake, S. R. A microfabricated fluorescence-activated cell sorter. *Nat. Biotechnol.* **17**, 1109 (1999).

134. Krüger, J. *et al.* Development of a microfluidic device for fluorescence activated cell sorting. *J. Micromechanics Microengineering* **12**, 486 (2002).

135. Yin, H. & Marshall, D. Microfluidics for single cell analysis. *Curr. Opin. Biotechnol.* **23**, 110–119 (2012).

136. Mu, X., Zheng, W., Sun, J., Zhang, W. & Jiang, X. Microfluidics for manipulating cells. *Small* **9**, 9–21 (2013).

137. Leary, J. F. *et al.* High-Resolution Separation of Rare Cell Types. **464**, 26–40 (1991).

138. Kleinstreuer, J. K. and C. Liquid flow in microchannels: experimental observations and computational analyses of microfluidics effects. *J. Micromechanics Microengineering* **13**, 568 (2003).

139. Russom, A. *et al.* Differential inertial focusing of particles in curved low-aspect-ratio microchannels. *New J. Phys.* **11**, 75025 (2009).

140. Kuntaegowdanahalli, S. S., Bhagat, A. A. S., Kumar, G. & Papautsky, I. Inertial microfluidics for continuous particle separation in spiral microchannels. *Lab Chip* **9**, 2973–2980 (2009).

141. Thanormsridetchai, A. *et al.* Focusing and sorting of multiple-sized beads and cells using low-aspect-ratio spiral microchannels. *J. Mech. Sci. Technol.* **31**, 5397–5405 (2017).

142. Hou, H. W. *et al.* Isolation and retrieval of circulating tumor cells using centrifugal

forces. *Sci. Rep.* **3**, 1259 (2013).

143. Lin, E. *et al.* High-throughput microfluidic labyrinth for the label-free isolation of circulating tumor cells. *Cell Syst.* **5**, 295–304 (2017).

144. Shen, S. *et al.* Spiral microchannel with ordered micro-obstacles for continuous and highly-efficient particle separation. *Lab Chip* **17**, 3578–3591 (2017).

145. Di Carlo, D., Irimia, D., Tompkins, R. G. & Toner, M. Continuous inertial focusing, ordering, and separation of particles in microchannels. *Proc. Natl. Acad. Sci.* **104**, 18892–18897 (2007).

146. Wu, Z., Willing, B., Bjerketorp, J., Jansson, J. K. & Hjort, K. Soft inertial microfluidics for high throughput separation of bacteria from human blood cells. *Lab Chip* **9**, 1193–1199 (2009).

147. Squires, T. M. & Quake, S. R. Microfluidics: Fluid physics at the nanoliter scale. *Rev. Mod. Phys.* **77**, 977 (2005).

148. Di Carlo, D., Edd, J. F., Irimia, D., Tompkins, R. G. & Toner, M. Equilibrium separation and filtration of particles using differential inertial focusing. *Anal. Chem.* **80**, 2204–2211 (2008).

149. Oakey, J. *et al.* Particle focusing in staged inertial microfluidic devices for flow cytometry. *Anal. Chem.* **82**, 3862–3867 (2010).

150. McFaul, S. M., Lin, B. K. & Ma, H. Cell separation based on size and deformability using microfluidic funnel ratchets. *Lab Chip* **12**, 2369–2376 (2012).

151. Fan, X. *et al.* A microfluidic chip integrated with a high-density PDMS-based microfiltration membrane for rapid isolation and detection of circulating tumor cells. *Biosens. Bioelectron.* **71**, 380–386 (2015).

152. Preira, P. *et al.* Passive circulating cell sorting by deformability using a microfluidic gradual filter. *Lab Chip* **13**, 161–170 (2013).

153. Mohamed, H., Turner, J. N. & Caggana, M. Biochip for separating fetal cells from maternal circulation. *J. Chromatogr. A* **1162**, 187–192 (2007).

154. Shen, Y., Yalikun, Y. & Tanaka, Y. Recent advances in microfluidic cell sorting

systems. *Sensors Actuators B Chem.* (2018).

155. Jiang, Y. *et al.* A multilayer lateral-flow microfluidic device for particle separation. *Microfluid. Nanofluidics* **22**, 40 (2018).

156. Chen, X., Liu, C. C. & Li, H. fa. *Sensors Actuators B Chem.* **130**, 216–221 (2008).

157. Raub, C. B., Lee, C. & Kartalov, E. Sequestration of bacteria from whole blood by optimized microfluidic cross-flow filtration for Rapid Antimicrobial Susceptibility Testing. *Sensors Actuators B Chem.* **210**, 120–123 (2015).

158. MOLDAY, R. S., YEN, S. P. S. & REMBAUM, A. Application of magnetic microspheres in labelling and separation of cells. *Nature* **268**, 437–438 (1977).

159. Miltenyi, S., Muller, W., Weichel, W. & Radbruch, A. High Gradient Magnetic Cell Separation With MACS1. *Cytometry* **238**, 231–238 (1990).

160. Herzenberg, L. A. *et al.* The History and Future of the Fluorescence Activated Cell Sorter and Flow Cytometry: A View from Stanford. *Clin. Chem.* **48**, 1819 LP – 1827 (2002).

161. Alix-Panabieres, C. & Pantel, K. Challenges in circulating tumour cell research. *Nat Rev Cancer* **14**, 623–631 (2014).

162. Gil, M., Sar-shalom, V., Sivira, Y. M., Carreras, R. & Checa, M. A. Sperm selection using magnetic activated cell sorting (MACS) in assisted reproduction : a systematic review and meta-analysis. *J Assist Reprod Genet* 479–485 (2013). doi:10.1007/s10815-013-9962-8

163. Kumar, V. & Rezai, P. Magneto-Hydrodynamic Fractionation (MHF) for continuous and sheathless sorting of high-concentration paramagnetic microparticles. *Biomed. Microdevices* **19**, 39 (2017).

164. Pamme, N. & Manz, A. On-Chip Free-Flow Magnetophoresis : Continuous Flow Separation of Magnetic Particles and Agglomerates. *Anal, Chem.* **76**, 7250–7256 (2004).

165. Adams, J. D., Kim, U. & Soh, H. T. Multitarget magnetic activated cell sorter. *PNAS* **2008**, 1–6 (2008).

166. Carr, C. *et al.* Design , fabrication and demonstration of a magnetophoresis chamber with 25 output fractions. *J. Magn. Magn. Mater*. **m**, 1440–1445 (2009).

167. Martin, A. B., Wu, W.-T., Kameneva, M. V & Antaki, J. F. Development of a high-throughput magnetic separation device for malaria-infected erythrocytes. *Ann. Biomed. Eng.* **45**, 2888–2898 (2017).

168. Lee, J.-J. *et al.* Synthetic ligand-coated magnetic nanoparticles for microfluidic bacterial separation from blood. *Nano Lett.* **14**, 1–5 (2013).

169. Foresti, D., Nabavi, M. & Poulikakos, D. On the acoustic levitation stability behaviour of spherical and ellipsoidal particles. *J. Fluid Mech.* **709**, 581–592 (2012).

170. Bruus, H. Lab on a Chip Acoustofluidics 7 : The acoustic radiation force on small particles. *Lab Chip* 1014–1021 (2012). doi:10.1039/c2lc21068a

171. Laurell, T., Petersson, F. & Nilsson, A. Chip integrated strategies for acoustic separation and manipulation of cells and particles. *Chem. Soc. Rev.* **36**, 492–506 (2007).

172. Wu, M. *et al.* Acoustofluidic separation of cells and particles. *Microsystems Nanoeng.* **5**, 32 (2019).

173. Johansson, L., Nikolajeff, F., Johansson, S. & Thorslund, S. On-Chip Fluorescence-Activated Cell Sorting by an Integrated Miniaturized Ultrasonic Transducer. *Anal. Chem.* **81**, 5188–5196 (2009).

174. Petersson, F., Nilsson, A., Holm, C., Jonsson, H. & Laurell, T. Separation of lipids from blood utilizing ultrasonic standing waves in microfluidic channels. *Analyst* **129**, 938–943 (2004).

175. Jakobsson, O., Grenvall, C., Nordin, M., Evander, M. & Laurell, T. Acoustic actuated fluorescence activated sorting of microparticles. *Lab Chip* **14**, 1943–1950 (2014).

176. Shi, J., Mao, X., Ahmed, D., Colletti, A. & Huang, T. J. Focusing microparticles in a microfluidic channel with standing surface acoustic waves (SSAW). *Lab Chip* **8**, 221–223 (2008).

177. Gossett, D. R. *et al.* Label-free cell separation and sorting in microfluidic systems. *Anal. Bioanal. Chem.* **397**, 3249–3267 (2010).

178. Shi, J., Huang, H., Stratton, Z., Huang, Y. & Huang, T. J. Continuous particle separation in a microfluidic channel via standing surface acoustic waves (SSAW). *Lab Chip* **9**, 3354–3359 (2009).

179. Goddard, G., Martin, J. C., Graves, S. W. & Kaduchak, G. Ultrasonic Particle-Concentration for Sheathless Focusing of Particles for Analysis in a Flow Cytometer. *Cytometry* **74**, 66–74 (2006).

180. Goddard, G. R., Sanders, C. K., Martin, J. C., Kaduchak, G. & Graves, S. W. Analytical Performance of an Ultrasonic Particle Focusing Flow Cytometer. *Anal. Chem.* **79**, 8740–8746 (2007).

181. Shi, J. *et al.* Three-dimensional continuous particle focusing in a microfluidic channel via standing surface acoustic waves (SSAW). *Lab Chip* **11**, (2011).

182. Austin Suthanthiraraj, P. P. *et al.* One-dimensional acoustic standing waves in rectangular channels for flow cytometry. *Methods* **57**, 259–271 (2012).

183. Kaduchak, G. & Ward, M. D. Application of acoustic radiation pressure to align cells in a commercial flow cytometer. *Proc. Meet. Acoust.* **19**, 45014 (2013).

184. Ma, Z., Zhou, Y., Collins, D. J. & Ai, Y. Fluorescence activated cell sorting via a focused traveling surface acoustic beam. *Lab Chip* **17**, 3176–3185 (2017).

185. Nawaz, A. A. *et al.* Acoustofluidic fluorescence activated cell sorter. *Anal. Chem.* **87**, 12051–12058 (2015).

186. Ren, L. *et al.* Standing Surface Acoustic Wave (SSAW)-Based Fluorescence-Activated Cell Sorter. *Small* **14**, 1801996 (2018).

187. Ung, W. L. *et al.* Enhanced surface acoustic wave cell sorting by 3D microfluidic-chip design. *Lab Chip* **17**, 4059–4069 (2017).

188. Cheng, I.-F., Chang, H.-C., Hou, D. & Chang, H.-C. An integrated dielectrophoretic chip for continuous bioparticle filtering, focusing, sorting, trapping, and detecting. *Biomicrofluidics* **1**, 21503 (2007).

189. Voldman, J. Electrical forces for microscale cell manipulation. *Annu. Rev. Biomed. Eng.* **8**, 425–454 (2006).

190. Wang, L., Flanagan, L. A., Monuki, E., Jeon, N. L. & Lee, A. P. Dielectrophoresis switching with vertical sidewall electrodes for microfluidic flow cytometry. *Lab Chip* **7**, 1114–1120 (2007).

191. Cole, R. H. *et al.* Printed droplet microfluidics for on demand dispensing of picoliter droplets and cells. *Proc. Natl. Acad. Sci.* **114**, 8728–8733 (2017).

192. Baret, J.-C. *et al.* Fluorescence-activated droplet sorting (FADS): efficient microfluidic cell sorting based on enzymatic activity. *Lab Chip* **9**, 1850–1858 (2009).

193. Sciambi, A. & Abate, A. R. Accurate microfluidic sorting of droplets at 30 kHz. *Lab Chip* **15**, 47–51 (2015).

194. Ashkin, A. Acceleration and trapping of particles by radiation pressure. *Phys. Rev. Lett.* **24**, 156 (1970).

195. Ashkin, A., Dziedzic, J. M. & Yamane, T. Optical trapping and manipulation of single cells using infrared laser beams. *Nature* **330**, 769 (1987).

196. Curtis, J. E., Koss, B. A. & Grier, D. G. Dynamic holographic optical tweezers. *Opt. Commun.* **207**, 169–175 (2002).

197. Schneckenburger, H. *et al.* Laser-assisted optoporation of single cells. *J. Biomed. Opt.* **7**, 410–417 (2002).

198. Deisseroth, K. Optogenetics. *Nat. Methods* **8**, 26 (2011).

199. Ekpenyong, A. E. *et al.* Viscoelastic properties of differentiating blood cells are fate-and function-dependent. *PLoS One* **7**, e45237 (2012).

200. Ashkin, A. *Optical trapping and manipulation of neutral particles using lasers: a reprint volume with commentaries*. (World Scientific, 2006).

201. Rodrigo, P. J., Daria, V. R. & Glückstad, J. Real-time three-dimensional optical micromanipulation of multiple particles and living cells. *Opt. Lett.* **29**, 2270–2272 (2004).

202. Zhang, H. & Liu, K.-K. Optical tweezers for single cells. *J. R. Soc. interface* **5**, 671–690 (2008).

203. Wang, X. *et al.* Enhanced cell sorting and manipulation with combined optical tweezer and microfluidic chip technologies. *Lab Chip* **11**, 3656–3662 (2011).

204. Grier, D. G. A revolution in optical manipulation. *Nature* **424**, 810–816 (2003).

205. Applegate, R. W., Squier, J., Vestad, T., Oakey, J. & Marr, D. W. M. Optical trapping, manipulation, and sorting of cells and colloids in microfluidic systems with diode laser bars. *Opt. Express* **12**, 4390–4398 (2004).

206. Wu, T.-H. *et al.* Pulsed laser triggered high speed microfluidic fluorescence activated cell sorter. *Lab Chip* **12**, 1378–1383 (2012).

207. Wang, M. M. *et al.* Microfluidic sorting of mammalian cells by optical force switching. *Nat. Biotechnol.* **23**, 83 (2005).

208. Zwaan, E., Le Gac, S., Tsuji, K. & Ohl, C.-D. Controlled Cavitation in Microfluidic Systems. *Phys. Rev. Lett.* **98**, 254501 (2007).

209. Chen, Y. *et al.* Pulsed laser activated cell sorting with three dimensional sheathless inertial focusing. *Small* **10**, 1746–1751 (2014).

210. Chen, Y., Wu, T.-H., Kung, Y.-C., Teitell, M. A. & Chiou, P.-Y. 3D pulsed laser-triggered high-speed microfluidic fluorescence-activated cell sorter. *Analyst* **138**, 7308–7315 (2013).

211. Fu, A. Y., Chou, H.-P., Spence, C., Arnold, F. H. & Quake, S. R. An integrated microfabricated cell sorter. *Anal. Chem.* **74**, 2451–2457 (2002).

212. Chen, P. *et al.* Hydrodynamic gating valve for microfluidic fluorescence-activated cell sorting. *Anal. Chim. Acta* **663**, 1–6 (2010).

213. Hulspas, R. *et al.* Purification of regulatory T cells with the use of a fully enclosed high-speed microfluidic system. *Cytotherapy* **16**, 1384–1389 (2014).

214. Abdelfattah, A. S. *et al.* Microfluidic cell sorter-aided directed evolution of a protein-based calcium ion indicator with an inverted fluorescent response. *Integr. Biol.* **6**, 714–725 (2014).

215. Cheng, Z., Wu, X., Cheng, J. & Liu, P. Microfluidic fluorescence-activated cell sorting (μFACS) chip with integrated piezoelectric actuators for low-cost mammalian cell enrichment. *Microfluid. Nanofluidics* **21**, 9 (2017).

216. Sakuma, S., Kasai, Y., Hayakawa, T. & Arai, F. On-chip cell sorting by high-speed local-flow control using dual membrane pumps. *Lab Chip* **17**, 2760–2767 (2017).

217. Herschel, J. F. W. On a case of superficial colour presented by a homogeneous liquid internally colourless. *Philos. Trans. R. Soc. London* 143–145 (1845).

218. Chalfie, M. & Kain, S. R. *Green fluorescent protein: properties, applications and protocols*. **47**, (John Wiley & Sons, 2005).

219. Prasher, D. C., Eckenrode, V. K., Ward, W. W., Prendergast, F. G. & Cormier, M. J. Primary structure of the Aequorea victoria green-fluorescent protein. *Gene* **111**, 229–233 (1992).

220. Yuste, R. Fluorescence microscopy today. *Nat. Methods* **2**, 902–904 (2005).

221. Day, R. N. & Schaufele, F. Fluorescent protein tools for studying protein dynamics in living cells: a review. *J. Biomed. Opt.* **13**, 31202 (2008).

222. Miller, L. W. & Cornish, V. W. Selective chemical labeling of proteins in living cells. *Curr. Opin. Chem. Biol.* **9**, 56–61 (2005).

223. Smiley, S. T. *et al.* Intracellular heterogeneity in mitochondrial membrane potentials revealed by a J-aggregate-forming lipophilic cation JC-1. *Proc. Natl. Acad. Sci.* **88**, 3671–3675 (1991).

224. Reano, A. *et al.* Lectins as markers of human epidermal cell differentiation. *Differentiation* **22**, 205–210 (1982).

225. Maecker, H. T., McCoy, J. P. & Nussenblatt, R. Standardizing immunophenotyping for the Human Immunology Project. *Nat. Rev. Immunol.* **12**, 191–200 (2012).

226. Lebaron, P., Parthuisot, N. & Catala, P. Comparison of blue nucleic acid dyes for flow cytometric enumeration of bacteria in aquatic systems. *Appl. Environ. Microbiol.* **64**, 1725–1730 (1998).

227. Pjura, P. E., Grzeskowiak, K. & Dickerson, R. E. Binding of Hoechst 33258 to the minor groove of B-DNA. *J. Mol. Biol.* **197**, 257–271 (1987).

228. Parks, D. R. & Herzenberg, L. A. [19] Fluorescence-activated cell sorting: Theory, experimental optimization, and applications in lymphoid cell biology. in *Immunochemical Techniques, Part G* (eds. Di Sabato, G., Langone, J. J. & Van Vunakis, H. B. T.-M. in E.) **108**, 197–241 (Academic Press, 1984).

229. Galbraith, D. W., Anderson, M. T. & Herzenberg, L. A. Flow cytometric analysis and FACS sorting of cells based on GFP accumulation. in *Methods in cell biology* **58**, 315–341 (Elsevier, 1998).

230. Geerts, A. *et al.* Purification of rat hepatic stellate cells by side scatter–activated cell sorting. *Hepatology* **27**, 590–598 (1998).

231. Gopinath, R. & Nutman, T. B. Identification of eosinophils in lysed whole blood using side scatter and CD16 negativity. *Cytometry* **30**, 313–316 (1997).

232. Thompson, J. M., Gralow, J. R., Levy, R. & Miller, R. A. The optimal application of forward and ninety-degree light scatter in flow cytometry for the gating of mononuclear cells. *Cytometry* **6**, 401–406 (1985).

233. Picot, J., Guerin, C. L., Le Van Kim, C. & Boulanger, C. M. Flow cytometry: retrospective, fundamentals and recent instrumentation. *Cytotechnology* **64**, 109–130 (2012).

234. Ashcroft, R. G. & Lopez, P. A. Commercial high speed machines open new opportunities in high throughput flow cytometry (HTFC). *J. Immunol. Methods* **243**, 13–24 (2000).

235. Ibrahim, S. F. & van den Engh, G. Flow Cytometry and Cell Sorting BT - Cell Separation: Fundamentals, Analytical and Preparative Methods. in (eds. Kumar, A., Galaev, I. Y. & Mattiasson, B.) 19–39 (Springer Berlin Heidelberg, 2007). doi:10.1007/10_2007_073

236. Williams, G. C. Pleiotropy, Natural Selection and the Evolution of Senescence. *Evolution (N. Y).* **11**, 398–411 (1957).

237. Campisi, J. Aging, Cellular Senescence, and Cancer. *Annu. Rev. Physiol.* **75**, 685–

705 (2013).

238. Hayflick, L. & Moorhead, P. S. The serial cultivation of human diploid cell strains. *Exp. Cell Res.* **25**, 585–621 (1961).

239. Aird, K. M. & Zhang, R. Detection of senescence-associated heterochromatin foci (SAHF). *Methods Mol. Biol.* **965**, 185–196 (2013).

240. Chandra, T. Senescence Associated Heterochromatic Foci: SAHF BT - The Functional Nucleus. in *The Functional Nucleus* (eds. Bazett-Jones, D. P. & Dellaire, G.) 205–218 (Springer International Publishing, 2016). doi:10.1007/978-3-319-38882-3_9

241. Hengartner, M. O. The biochemistry of apoptosis. *Nature* **407**, 770–776 (2000).

242. Buendia, B., Santa-Maria, A. & Courvalin, J. C. Caspase-dependent proteolysis of integral and peripheral proteins of nuclear membranes and nuclear pore complex proteins during apoptosis. *J. Cell Sci.* **112**, 1743–1753 (1999).

243. Elmore, S. Apoptosis: a review of programmed cell death. *Toxicol. Pathol.* **35**, 495–516 (2007).

244. Gentric, G., Celton-Morizur, S. & Desdouets, C. Polyploidy and liver proliferation. *Clin. Res. Hepatol. Gastroenterol.* **36**, 29–34 (2012).

245. Gentric, G., Desdouets, C. & Celton-Morizur, S. Hepatocytes Polyploidization and Cell Cycle Control in. *Int. J. Hepatol.* **2012**, (2012).

246. Duncan, A. W. *et al.* The ploidy conveyor of mature hepatocytes as a source of genetic variation. *Nature* **467**, 707–710 (2010).

247. Lewsey, J. *et al.* PTH-104 Hospital Admissions and Associated Costs of Alcoholic Liver Disease in Scotland Between 1991 and 2011. *Gut* **65**, A270 LP-A270 (2016).

248. Stubbington, M. J. T., Rozenblatt-Rosen, O., Regev, A. & Teichmann, S. A. Single-cell transcriptomics to explore the immune system in health and disease. *Science (80-.).* **358**, 58–63 (2017).

249. Lei, C. *et al.* High-throughput imaging flow cytometry by optofluidic time-stretch microscopy. *Nat. Protoc.* **13**, 1603–1631 (2018).

250. Yang, R.-J., Fu, L.-M. & Hou, H.-H. Review and perspectives on microfluidic flow cytometers. *Sensors Actuators B Chem.* **266**, 26–45 (2018).

251. Hosic, S., Murthy, S. K. & Koppes, A. N. Microfluidic Sample Preparation for Single Cell Analysis. *Anal. Chem.* **88**, 354–380 (2016).

252. Girault, M. *et al.* An on-chip imaging droplet-sorting system: a real-time shape recognition method to screen target cells in droplets with single cell resolution. *Sci. Rep.* **7**, 40072 (2017).

253. Ota, S. *et al.* Ghost cytometry. *Science (80-.).* **360**, 1246–1251 (2018).

254. Eulenberg, P. *et al.* Reconstructing cell cycle and disease progression using deep learning. *Nat. Commun.* **8**, 463 (2017).

255. Lee, K. C. M. *et al.* Quantitative Phase Imaging Flow Cytometry for Ultra-Large-Scale Single-Cell Biophysical Phenotyping. *Cytom. Part A* (2019).

256. Gu, Y. *et al.* Machine Learning Based Real-Time Image-Guided Cell Sorting and Classification. *Cytom. Part A* (2019).

257. Aström, K. J. & Murray, R. M. *Feedback systems: an introduction for scientists and engineers*. (Princeton university press, 2010).

258. Arulmozhiyal, R. & Kandiban, R. Design of fuzzy PID controller for brushless DC motor. in *Computer Communication and Informatics (ICCCI), 2012 International Conference on* 1–7 (IEEE, 2012).

259. de Abreu Costa, L. *et al.* Dimethyl sulfoxide (DMSO) decreases cell proliferation and TNF-α, IFN-γ, and IL-2 cytokines production in cultures of peripheral blood lymphocytes. *Molecules* **22**, 1789 (2017).

260. Li, Z., Mak, S. Y., Sauret, A. & Shum, H. C. Syringe-pump-induced fluctuation in all-aqueous microfluidic system implications for flow rate accuracy. *Lab Chip* **14**, 744–9 (2014).

261. Ford, T., Graham, J. & Rickwood, D. Iodixanol: A Nonionic Iso-osmotic Centrifugation Medium for the Formation of Self-Generated Gradients. *Anal. Biochem.* **220**, 360–366 (1994).

262. Isozaki, A. *et al.* A practical guide to intelligent image-activated cell sorting. *Nat. Protoc.* **14**, 2370–2415 (2019).

263. Jiang, X. *et al.* Quantification of cell size using temporal diffusion spectroscopy. *Magn. Reson. Med.* **75**, 1076–1085 (2016).

264. Boothe, T. *et al.* A tunable refractive index matching medium for live imaging cells, tissues and model organisms. *Elife* **6**, e27240 (2017).

265. Akimoto, T., Sasaki, S., Ikebukuro, K. & Karube, I. Refractive-index and thickness sensitivity in surface plasmon resonance spectroscopy. *Appl. Opt.* **38**, 4058–4064 (1999).

266. Nagrath, S. *et al.* Isolation of rare circulating tumour cells in cancer patients by microchip technology. *Nature* **450**, 1235–1239 (2007).

267. Chang, Q. *et al.* Imaging mass cytometry. *Cytom. part A* **91**, 160–169 (2017).

268. Bernuau, D., Rogier, E. & Feldmann, G. Decreased albumin and increased fibrinogen secretion by single hepatocytes from rats with acute inflammatory reaction. *Hepatology* **3**, 29–33 (1983).

269. Oka, J. A. & Weigel, P. H. Recycling of the asialoglycoprotein receptor in isolated rat hepatocytes. Dissociation of internalized ligand from receptor occurs in two kinetically and thermally distinguishable compartments. *J. Biol. Chem.* **258**, 10253–10262 (1983).

270. Sreejith, K. R., Ooi, C. H., Jin, J., Dao, D. V. & Nguyen, N.-T. Digital polymerase chain reaction technology–recent advances and future perspectives. *Lab Chip* **18**, 3717–3732 (2018).